PDRs4All II. JWST's NIR and MIR imaging view of the Orion Nebula

Citation for the original published paper (version of record):

N.B. When citing this work, cite the original published paper.

(article starts on next page)

**Astronomy
&
Astrophysics**

PDRs4All

II. JWST's NIR and MIR imaging view of the Orion Nebula[*]

Emilie Habart[1], Els Peeters[2,3,4], Olivier Berné[5], Boris Trahin[1], Amélie Canin[5], Ryan Chown[2,3], Ameek Sidhu[2,3],
Dries Van De Putte[6], Felipe Alarcón[7], Ilane Schroetter[5], Emmanuel Dartois[8], Sílvia Vicente[9], Alain Abergel[1],
Edwin A. Bergin[7], Jeronimo Bernard-Salas[10,11], Christiaan Boersma[12], Emeric Bron[13], Jan Cami[2,3,4],
Sara Cuadrado[14], Daniel Dicken[15], Meriem Elyajouri[1], Asunción Fuente[16], Javier R. Goicoechea[14],
Karl D. Gordon[6,17], Lina Issa[5], Christine Joblin[5], Olga Kannavou[1], Baria Khan[2,3,4], Ozan Lacinbala[18],
David Languignon[13], Romane Le Gal[19,20], Alexandros Maragkoudakis[12], Raphael Meshaka[1,13], Yoko Okada[21],
Takashi Onaka[22,23], Sofia Pasquini[2], Marc W. Pound[7], Massimo Robberto[6,24], Markus Röllig[25,26],
Bethany Schefter[2,3], Thiébaut Schirmer[1,27], Benoit Tabone[1], Alexander G. G. M. Tielens[28,29], Mark G. Wolfire[29],
Marion Zannese[1], Nathalie Ysard[1], Marc-Antoine Miville-Deschenes[30], Isabel Aleman[31], Louis Allamandola[12,32],
Rebecca Auchettl[33], Giuseppe Antonio Baratta[34], Salma Bejaoui[12], Partha P. Bera[12,35], John H. Black[27],
Francois Boulanger[36], Jordy Bouwman[37,38,39], Bernhard Brandl[28,40], Philippe Brechignac[8],
Sandra Brünken[41], Mridusmita Buragohain[42], Andrew Burkhardt[43], Alessandra Candian[44], Stéphanie Cazaux[45],
Jose Cernicharo[14], Marin Chabot[46], Shubhadip Chakraborty[47,48], Jason Champion[5], Sean W. J. Colgan[12],
Ilsa R. Cooke[49], Audrey Coutens[5], Nick L.J. Cox[10,11], Karine Demyk[5], Jennifer Donovan Meyer[50],
Sacha Foschino[5], Pedro García-Lario[51], Lisseth Gavilan[12], Maryvonne Gerin[52], Carl A. Gottlieb[53],
Pierre Guillard[54,55], Antoine Gusdorf[36,52], Patrick Hartigan[56], Jinhua He[57,58,59], Eric Herbst[60],
Liv Hornekaer[61], Cornelia Jäger[62], Eduardo Janot-Pacheco[63], Michael Kaufman[64], Francisca Kemper[65,66,67],
Sarah Kendrew[68], Maria S. Kirsanova[69], Pamela Klaassen[15], Sun Kwok[70], Álvaro Labiano[71],
Thomas S.-Y. Lai[72], Timothy J. Lee[12,†], Bertrand Lefloch[73], Franck Le Petit[13], Aigen Li[74], Hendrik Linz[75],
Cameron J. Mackie[76,77], Suzanne C. Madden[28], Joëlle Mascetti[78], Brett A. McGuire[50,79], Pablo Merino[80],
Elisabetta R. Micelotta[81], Karl Misselt[82], Jon A. Morse[83], Giacomo Mulas[34,5], Naslim Neelamkodan[84],
Ryou Ohsawa[85], Alain Omont[52], Roberta Paladini[86], Maria Elisabetta Palumbo[34], Amit Pathak[87],
Yvonne J. Pendleton[88], Annemieke Petrignani[89], Thomas Pino[8], Elena Puga[68], Naseem Rangwala[12],
Mathias Rapacioli[90], Alessandra Ricca[12,4], Julia Roman-Duval[6], Joseph Roser[4,12], Evelyne Roueff[13],
Gaël Rouillé[62], Farid Salama[12], Dinalva A. Sales[91], Karin Sandstrom[92], Peter Sarre[93], Ella Sciamma-O'Brien[12],
Kris Sellgren[94], Sachindev S. Shenoy[95], David Teyssier[51], Richard D. Thomas[96], Aditya Togi[97],
Laurent Verstraete[1], Adolf N. Witt[98], Alwyn Wootten[50], Henning Zettergren[99], Yong Zhang[100],
Ziwei E. Zhang[101], and Junfeng Zhen[102]

(Affiliations can be found after the references)

ABSTRACT

Context. The *James Webb* Space Telescope (JWST) has captured the most detailed and sharpest infrared (IR) images ever taken of the inner region of the Orion Nebula, the nearest massive star formation region, and a prototypical highly irradiated dense photo-dissociation region (PDR).

Aims. We investigate the fundamental interaction of far-ultraviolet (FUV) photons with molecular clouds. The transitions across the ionization front (IF), dissociation front (DF), and the molecular cloud are studied at high-angular resolution. These transitions are relevant to understanding the effects of radiative feedback from massive stars and the dominant physical and chemical processes that lead to the IR emission that JWST will detect in many Galactic and extragalactic environments.

Methods. We utilized NIRCam and MIRI to obtain sub-arcsecond images over $\sim$150″ and 42″ in key gas phase lines (e.g., Pa α, Br α, [FeII] 1.64 μm, H_2 1–0 S(1) 2.12 μm, 0–0 S(9) 4.69 μm), aromatic and aliphatic infrared bands (aromatic infrared bands at 3.3–3.4 μm, 7.7, and 11.3 μm), dust emission, and scattered light. Their emission are powerful tracers of the IF and DF, FUV radiation field and density distribution. Using NIRSpec observations the fractional contributions of lines, AIBs, and continuum emission to our NIRCam images were estimated. A very good agreement is found for the distribution and intensity of lines and AIBs between the NIRCam and NIRSpec observations.

Results. Due to the proximity of the Orion Nebula and the unprecedented angular resolution of JWST, these data reveal that the molecular cloud borders are hyper structured at small angular scales of ~0.1–1″ (~0.0002–0.002 pc or ~40–400 au at 414 pc). A diverse set of features are observed such as ridges, waves, globules and photoevaporated protoplanetary disks. At the PDR atomic to molecular transition, several bright features are detected that are associated with the highly irradiated surroundings of the dense molecular condensations and embedded young star. Toward the Orion Bar PDR, a highly sculpted interface is detected with sharp edges and density increases near the IF and DF. This was predicted by previous modeling studies, but the fronts were unresolved in most tracers. The spatial distribution of the AIBs reveals that the PDR edge is steep and is followed by an extensive warm atomic layer up to the DF with multiple ridges. A complex, structured, and folded H^0/H_2 DF surface was traced by the H_2 lines. This dataset was used to revisit the commonly adopted 2D PDR structure of the Orion Bar as our observations show that a 3D "terraced" geometry is required to explain the JWST observations. JWST provides us with a complete view of the PDR, all the way from the PDR edge to the substructured dense region, and this allowed us to determine, in detail, where the emission of the atomic and molecular lines, aromatic bands, and dust originate.

Conclusions. This study offers an unprecedented dataset to benchmark and transform PDR physico-chemical and dynamical models for the JWST era. A fundamental step forward in our understanding of the interaction of FUV photons with molecular clouds and the role of FUV irradiation along the star formation sequence is provided.

Keywords: infrared: ISM – photon-dominated region (PDR) – ISM: clouds

1. Introduction

Massive stars dominate the evolution of the galaxy through the injection of radiative and mechanical energy into their natal molecular cloud and surrounding interstellar medium (ISM). This feedback stirs up and heats the gas and limits molecular cloud lifetimes through photo-ionization and photo-evaporation, inhibiting future star formation. Feedback can also trigger star formation as gas is swept up in dense and massive shells. Hence, feedback is closely tied to the star formation efficiency of molecular gas (e.g., Elmegreen 2011; Hopkins et al. 2014).

Our understanding of stellar feedback is directly linked to studies of photo-dissociation regions (PDRs). PDRs are the regions where far-ultraviolet (FUV; $6\,eV < h\nu < 13.6\,eV$) radiation from massive stars dominates the thermal processes and chemistry (see reviews by Hollenbach & Tielens 1997; Wolfire et al. 2022). PDRs separate the gas ionized by a star from the molecular cloud in which the star was born. Hence, stellar radiative energy is mainly deposited in a PDR, while the mechanical energy is transmitted through the PDR layer to the interiors of molecular clouds in the form of shock waves and/or turbulence. The "classic" PDRs are at the interface between the HII region and the molecular cloud, extending into the deeper molecular layers (e.g., Tielens & Hollenbach 1985b,a). PDRs however, appear in many other environments including reflection nebulae (Sheffer et al. 2011; Peeters et al. 2017), planetary nebulae (Bernard-Salas & Tielens 2005), surfaces of pillars and globules (Goicoechea et al. 2020; Schneider et al. 2021), the diffuse ISM (Wolfire et al. 1995, 2003), and in protostellar and protoplanetary disks (Gorti & Hollenbach 2002; Vicente et al. 2013; Champion et al. 2017; see reviews by Öberg & Bergin 2021; Winter & Haworth 2022). In fact, most of the nonstellar baryons in galaxies are in PDRs (Hollenbach & Tielens 1999). Thus, understanding the physics and chemistry of PDRs is critical for understanding the star formation history of the Universe.

With their wavelength coverage extending well into the mid-infrared, the instruments on JWST are well suited to study the physical and chemical characteristics of PDRs. The warm ($T \simeq 100$–1000 K) and dense ($n \gtrsim 10^3\,cm^{-3}$) PDR gas – in part heated through photoelectric emission of electrons from small grains and molecules (Bakes & Tielens 1994; Weingartner & Draine 2001; Berné et al. 2022a) – is bright in the pure rotational transitions of H_2, the mid- and far-infrared fine-structure transitions of atomic ions and neutrals (e.g., Si^+, Fe^+, C^+, O), rotational transitions of CO and its isotopes, and rotational transitions of small

radicals. Carbon is singly ionized in the PDR surface layers and the cascade generated by electron recombinations will produce a rich spectrum of C^0 lines (Cesarsky 1982; Walmsley et al. 2000). In addition, the strong FUV field produces bright fluorescence in the near-infrared ro-vibrational transitions of H_2, atomic transitions of O and N, and the Aromatic Infrared Bands (AIBs), generally attributed to the emission of vibrationally excited polycyclic aromatic hydrocarbon molecules (PAHs; e.g. Black & van Dishoeck 1987; Tielens et al. 1993; Marconi et al. 1998; Martini et al. 1999; Peeters et al. 2004; Tielens 2008; Habart et al. 2011). The adjoining ionized gas will show bright IR line emission produced by collisional excitation of fine-structure levels (e.g., Fe^+, Ar^+, Ar^{2+}, Ne^+, Ne^{2+}, S^{2+}, S^{3+}) and by recombination lines from HI and HeI (Martín-Hernández et al. 2002; Rubin et al. 2007). The spatial resolution of JWST (~0.1–1″) exceeds that of all other space telescopes over the same wavelength range[1] and is similar in spatial resolution to that of the Atacama Large Millimeter Array (ALMA) at submillimeter wavelengths. JWST has many IR filters centered on gas lines, molecular spectroscopic patterns as well as the continuum due to interstellar dust (emission and scattering). JWST emission line and continuum images of a PDR thus carry key information relevant to our understanding of the morphological impacts of stellar feedback, and JWST observations enable us to probe at unprecedented resolution how a molecular cloud is being disrupted by strong stellar UV radiation, winds, outflows and jets.

The focus of this article is on JWST NIRCam and MIRI images of the Orion Nebula complex carried out as part of the PDRs4All Early Release Science (ERS) program (Berné et al. 2022b). The Orion Nebula complex is a nearby site of active star formation exhibiting many feedback processes and PDR interfaces (e.g., Pabst et al. 2019). The prototypical highly irradiated dense PDR in this nebula is usually referred to as the "Bright Bar" or "Orion Bar" (e.g., Elliott & Meaburn 1974; Tielens et al. 1993; O'Dell & Yusef-Zadeh 2000). In the following, we refer to it as the "Bar." The ionizing and FUV radiation from the Orion Trapezium Cluster shines directly on the face of the Bar. At the outer layers, the ionized gas recombines at the ionization front (IF) and the gas becomes neutral hydrogen. This corresponds to the edge of the neutral PDR. The gas remains atomic (e.g., van der Werf et al. 2013; Henney 2021) until the H_2 dissociation

---

[1] The ground based Keck telescope using adaptive optics can achieve a similar spatial resolution but with a restricted IR filter set and wavelength range (e.g., Habart et al. 2023).
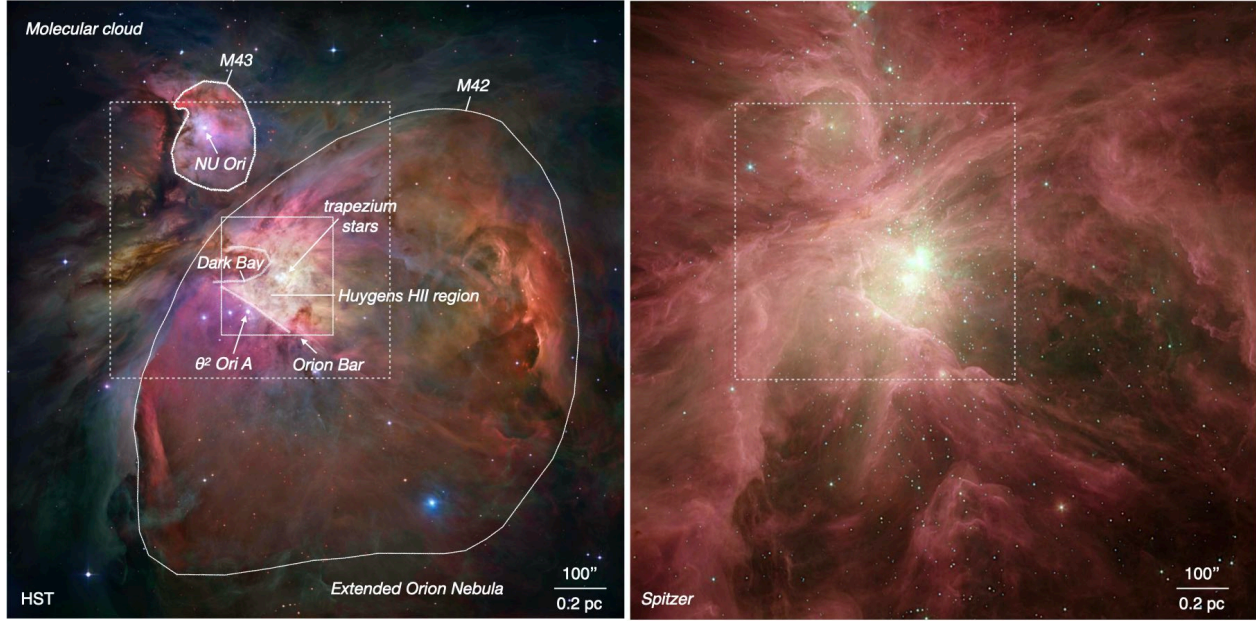
Fig. 1. Composite color *Hubble* (left) and *Spitzer* (right) views of M42 and M43 in the Orion Nebula complex. The solid white lines delineate the shells of M42 and M43, the Bar, the Huygens HII region, and the Dark Bay. The Huygens Region corresponds to the brightest parts of the Orion Nebula. The Dark Bay shows that there are regions of high optical depth between the observer and the ionized gas. Foreground depressions of visible light such as the Dark Bay are globally known as the Veil (Abel et al. 2019; Pabst et al. 2019). Arrows indicate the positions of the most massive stars within each region: Trapezium stars in M42 and NU Ori in M43. The position of the θ^2 Ori A star near the center of the Bar is also indicated. The areas where the JWST observations were obtained are the Bar, north of the Dark Bay, and north of M42 and M43 as presented in Fig. 2. The large dashed rectangle shows the limits of the upper panel of Fig. 2. The image credits for *Hubble* are as follows: NASA, ESA, M. Robberto (Space Telescope Science Institute/ESA) and the *Hubble* Space Telescope Orion Treasury Project Team. The image credits for *Spitzer* are as follows: NASA/JPL-Caltech/Univ. of Toledo. The wavelengths of the composite color images correspond to 435, 555, 658, 775 and 850 nm for *Hubble* and 3.6, 4.5, 5.8 and 8 μm for *Spitzer*.

front (DF), where the molecular hydrogen abundance increases rapidly. Over nearly 40 years, the Bar has been the target of many studies to elucidate the physical and chemical characteristics of PDRs (Parmar et al. 1991; Tielens et al. 1993; Tauber et al. 1994; Young Owl et al. 2000; Bernard-Salas et al. 2012; Goicoechea et al. 2016; Parikka et al. 2018; Kaplan et al. 2021) and provides therefore a widely-used template for the observational signature of the interaction of stars with their environment, both in the Milky Way and galaxies out to high redshifts (Stacey et al. 2010; Vallini et al. 2018; Wolfire et al. 2022). With its wide wavelength coverage, high sensitivity, multiple filters and high spectral resolution resulting in large line-to-continuum ratios, JWST has the potential to provide a coherent vision of the structure of the Bar. Its structure includes the extended atomic layers (often called the "inter-clump" medium) and the thin emission layers of dense warm gas associated with the DF as well as the illuminated surfaces of large dense clumps.

The article is organized as follows. In Sect. 2, we describe the main physical characteristics of our target inferred from previous studies. The observations, data reduction and the fractional contributions of line, AIB, and continuum emission to our NIRCam images are described in Sect. 3. In Sect. 4, we describe the structures observed by NIRCam and MIRI within the inner region of the OrionNebula. In Sect. 5, we focus on the Bar as a template region to understand the structure and morphology of a strongly irradiated PDR. The complex transition from the IF, the PDR DF to the molecular cloud is studied, and we determine in detail the origin of the atomic and molecular lines, aromatic bands, and dust emission. In Sect. 6, we describe the photoevaporating proto-planetary disks observed in the whole NIRCam fields. A summary and conclusions are given in Sect. 7. In Appendix A,

we show the template NIRSpec spectra presented in Peeters et al. (2023) in the wavelength domain of NIRCam filters, illustrating the variation of the contribution of different lines into each imaging band. Appendix B provides NIRCam and ground based images of the Bar. In Appendix C, we describe the structures observed within the NIRCam fields north of the Dark Bay, north of M42 and in M43 (Fig. 1).

2. M42 and the Bar

The Orion HII region, M42, – the nearest site of massive star formation – is illuminated by the Trapezium stars for which the O7-type star, θ^1 Ori C dominates (Sota et al. 2011), being the most massive and luminous member of the Trapezium cluster at the heart of the Orion Nebula (e.g., O'Dell 2001b). θ^1 Ori C has created a concave blister of ionized gas on the surface of the underlying Orion Molecular Core 1 (OMC-1) (see Wen & O'Dell 1995; O'Dell 2001b, and references therein), with the brightest portion called the Huygens Region (Fig. 1). The electron density varies across this region from a central high of almost 10^4 cm^{-3} to 3×10^3 cm^{-3} in the outer regions, while the electron temperature is usually about 9000 K (Weilbacher et al. 2015). Between the ionized gas and OMC-1 lies a PDR that is face-on to our line of sight. In the region of the Bar, the ionized atomic layer and its PDR are tilted almost along the line of sight (~4 (1–8) degrees, Walmsley et al. 2000; Pellegrini et al. 2009; Salgado et al. 2016; Peeters et al. 2023), forming an escarpment in the Main Ionization Front (MIF) and due to projection effects, producing one of the optically brightest features of the Huygens Region. This also provides the ability to probe without

overlapping the multiple layers of the PDR (Tielens et al. 1993; Hogerheijde et al. 1995, cf. Fig. 5). The Bar is a strongly UV irradiated PDR viewed nearly edge-on.

The gas density (n_H) in the ambient molecular cloud is estimated to be $n_H = 0.5$–1.0×10^5 cm^{-3} from a variety of IR and submillimeter gaseous emission lines (Tielens & Hollenbach 1985a; Hogerheijde et al. 1995; Bernard-Salas et al. 2012; Goicoechea et al. 2017). In addition, much denser small structures and molecular condensations ("clumps") are embedded in the Bar ($n_H \gtrsim 10^6$ cm^{-3}; Lis & Schilke 2003; Goicoechea et al. 2016; Joblin et al. 2018; Cuadrado et al. 2019). The Far-UV (FUV) radiation field incident on the PDR of the Bar is $G_0 = 2.2$–7.1×10^4 in Habing units (1.6×10^{-3} erg cm^{-2} s^{-1}; Habing 1968) as derived from UV-pumped IR-fluorescent lines of OI by Marconi et al. (1998) and Peeters et al. (2023). Given the stellar characteristics of θ^1 Ori C and the far-IR surface brightness of the Bar, this places θ^1 Ori C at a physical distance of 0.33 pc from the far-IR dust emission (Salgado et al. 2016). The projected distance between the star and the ionization front (IF) is about 0.2 pc (cf., Fig. 5). Beyond the IF, where the hydrogen gas converts from ionized to neutral, only FUV photons with energies below 13.6 eV penetrate the cloud. This corresponds to the edge of the neutral PDR but note that species with low ionization potentials (e.g., C, S, Fe) are still ionized in the surface layers of PDRs. Deeper in ($\Delta A_V \simeq 1$–2 mag), the radiation field has been sufficiently attenuated by dust extinction that hydrogen goes from atomic to molecular. At a depth of $\Delta A_V \simeq 2$–4 mag, the carbon balance shifts from C$^+$ to C^0 to CO (Tielens & Hollenbach 1985b). This chemical stratification has been verified by an important series of infrared to radio observations (e.g., Jansen et al. 1995; Tielens et al. 1993; Goicoechea et al. 2016). Relative to the molecular gas in OMC-1, the PDR gas flows through the ionization front at ~ 1 km s^{-1} (Pabst et al. 2019) and once ionized accelerates away at about 7 ± 4 km s^{-1} for the [N II] emitting layer close to the ionization front and 12 ± 4 km s^{-1} for the [O III] emitting layer further out (O'Dell et al. 2020) as it joins the general expansion of the nebula. Close to θ^1 Ori C there is a low density bubble of gas of diameter of 0.2 pc shaped by its stellar wind (O'Dell et al. 2009, 2020). This wind-blown cavity is open to the southwest and feeds the region of the Extended Orion Nebula (EON, Fig. 1) where hot shocked gas has been detected (Güdel et al. 2008). A layer of ionized gas covers much of the Huygens Regions (García-Díaz & Henney 2007; O'Dell et al. 2020) and outside of this is the atomic layer of gas known as the Veil, one portion of which is a hemispherical bubble best described as the Outer Shell, which was discovered by Pabst et al. (2019) and expands at about 13 km s^{-1} away from the OMC. The Veil has a column density of $N_H = (2$–$6) \times 10^{21}$ cm^{-2}, depending on the direction, and obscures the Huygens Region by 1–3 magnitudes of visual extinction (O'Dell et al. 1992; O'Dell & Yusef-Zadeh 2000; Weilbacher et al. 2015). The physical characteristics of the Bar are summarized in Table 2.

Assuming that the background PDR directly behind the Trapezium stars is a face-on PDR, the incident FUV field is estimated to be 10^5 Habings from the observed far-IR surface brightness (Tielens & Hollenbach 1985a); a factor of $\simeq 2$–5 higher than the FUV field incident on the Bar. The gas density in this PDR is estimated to be slightly higher (10^5 cm^{-3}) than in the Bar (Tielens & Hollenbach 1985a), concomitant with the higher density of the ionized gas (Weilbacher et al. 2015).

The wide field of view of the JWST images include the nearby low-ionization HII region M43 (NGC 1982) powered by HD 37061 (also known as NU Ori), a B0.5V star (Fig. 1). M43 lies to the northeast of M42 and this object has not been well studied but we include analysis of this JWST data in this article as well. M43 is seen to be shielded from illumination by θ^1 Ori C by the northeast portion of the wall bounding M42.

M42 exhibits several high-velocity features, including microjets, large scale Herbig-Haro flows, and wind driven shocks (e.g., Bally et al. 2000; O'Dell 2001b). Protostellar jets and outflows emanate from dust-enshrouded, nascent stars. Shocks are formed where the collimated flows interact with the nebula's ambient ionized gas and the neutral foreground veil. Additionally, uncollimated flows from the low-mass accreting stars and the stellar wind from θ^1 Ori C produce shocks. M42 further shows structures resulting from embedded sources of outflow in the BN-KL and Orion-S regions.

As this summary demonstrates, many questions remain on: (i) the detailed geometry of this highly irradiated and very structured PDR; (ii) the best tracers of the different physical zones (H$^+$, H^0, H$_2$, C$^+$, C, CO); (iii) the physical and chemical conditions in these different zones, particularly at the ionization and dissociation fronts; (iv) the relationship of the various components (interclump, clumps, proplyds, winds and jets) populating this region. JWST, with its high spatial resolution, can uniquely address these issues and thereby provide valuable insight in the physical and chemical processes taking place in FUV irradiated, interstellar material.

3. Observations and data reduction

3.1. Observations

We provide in this section a summary of the main parameters of imaging observations obtained within the ERS project #1288 "Radiative Feedback from Massive Stars as Traced by Multi-band Imaging and Spectroscopic Mosaics", based on NIRCam and MIRI observations (Berné et al. 2022b). The details of the observations can be retrieved from STScI using the Astronomer Proposal Toolkit (APT) under program ID 1288.

The telescope orientation (V3 Position Angle) was left unconstrained between 260 and 270 degrees. At the time of observation, 10–11th of September 2022, the telescope was oriented at about 265 degrees, resulting in the pointing illustrated in Fig. 2.

For NIRCam observations, we refer in particular to the data obtained under Observation 1 "NIRCam Orion Bar Imaging", whereas for MIRI we refer to Observations 15 and 16 "MIRI Orion Bar Imaging". These two MIRI observations were executed with NIRCam in parallel on September 11th for the $F1500W$ and $F2550W$ filters and September 18th for the $F770W$ and $F1130W$ filters, with a difference between these two dates for the telescope orientation on the ecliptic plane of about 3 degrees. Due to the V3 orientation, the parallel NIRCam field observed covers the northern part of the Orion Nebula, near the M43 (NGC 1982) region. A second set of background images, Observations 14 and 17, were taken at an offset field about 2 degrees west of the Bar using again MIRI and NIRCam in parallel with the same parameters adopted for Observation 15 and 16, respectively. However, Observations 14 could not be achieved due to Fine Guidance Sensor (FGS) loss of fine guidance control, the background observations in the corresponding MIRI and NIRCAM filters are therefore not available. An overview of the imaging filter selection is given in Table 1.
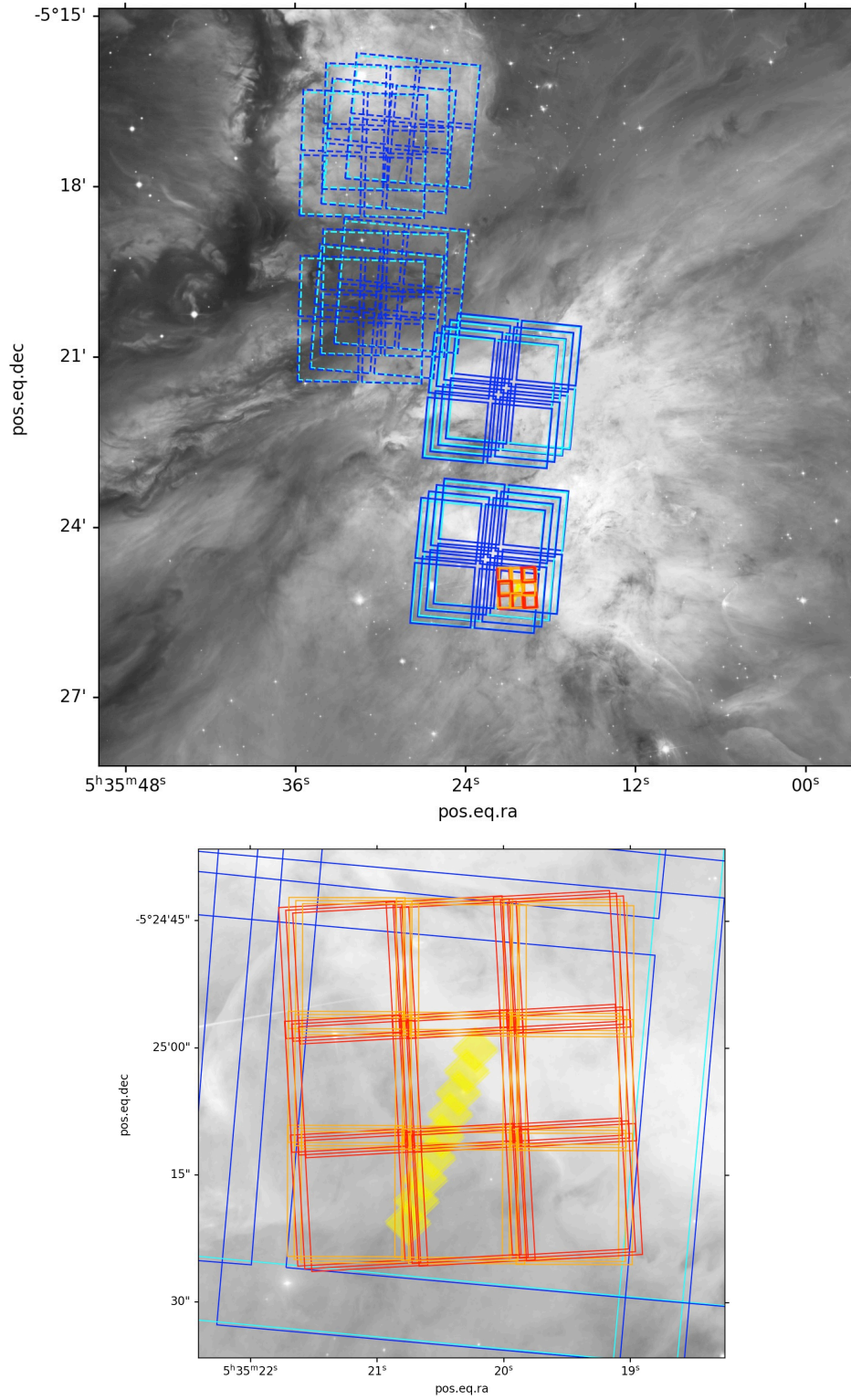
Fig. 2. Overlay of the JWST NIRCam (blue) and MIRI (red) imaging and NIRSpec (yellow) footprints on the *Hubble* Space Telescope image of the Bar at 1.3 μm (Robberto et al. 2020). Upper: all of the NIRCam and MIRI observations. For NIRCam, module B covering the Bar and module A in the North of the Dark Bay are shown in this overlay. The pointing position is situated in between these two modules at RA = $05^h35^m20.1963$, Dec = $-05°23'10.45''$. Dotted FOVs correspond to the NIRCam parallel observations. Lower: MIRI observations are centered on position RA = $05^h35^m20.3448$, Dec = $-05°25'4.01''$. The NIRSpec footprint (yellow) is a strip oriented perpendicularly to the ionization front.

Table 1. Summary of imaging observations obtained with NIRCam and MIRI and filters selection.

Species	$\lambda^{(1)}$ (μm)	Filter	Cont. filter[2]	B[3]	S/R[4]	M43[5]	Obs. ID (OB,M43/BKG)	Background[7]	Pixel scale (arcsec)	PSF FWHM (arcsec)
						NIRCam				
[FeII]	1.644	F164N		√	>4		1		0.031	0.056
			F162M	√	>30		1		0.031	0.055
Pa α	1.876	F187N		√	> 54	√	1,15/14	×	0.031	0.064
			F182M	√	> 75	√	1,16/17	√	0.031	0.062
Br α	4.052	F405N		√	>326	√	1,16/17	√	0.063	0.136
			F480M	√	>198		1		0.063	0.164
			F410M			√	1,15/14	×	0.063	0.137
H$_2$	2.120	F212N		√	>6	√	1,15/14	×	0.031	0.072
			F210M	√	>38	√	1,16/17	√	0.031	0.071
AIB	3.235	F323N[6]		√	>60		1		0.063	0.108
			F300M	√	>131		1,15/14	×	0.063	0.100
H$_2$	4.694	F470N		√	>54		1		0.063	0.160
			F480M	√	>198		1		0.063	0.164
AIBs	3.3–3.4	F335M		√	>382	√	1,16/17	√	0.063	0.111
			F300M	√	>131	√	1,15/14		0.063	0.100
	1.405	F140M		√	>19		1		0.031	0.048
	2.672	*F277W*		√	>182		1		0.063	0.092
						MIRI				
AIBs	7.7	*F770W*		√			15/14	×	0.11	0.269
AIBs	11.3	*F1130W*		√			15/14	×	0.11	0.375
	15.0	*F1500W*		√			16/17	√	0.11	0.488
	25.5	*F2550W*		√			16/17	√	0.11	0.803

Notes. The main targeted species and features with the chosen filters are given in the first and third column. [1]The wavelength of the transition or pivot wavelength of the filter for NIRCam broad band filters. [2]Continuum filter. [3]B: Bar (on-target observations) and north of the Bar. [4]S/R: minimum signal-to-noise ratio measured at the template positions (HII, atomic and molecular regions) in the Bar and covered by the NIRSpec field. [5]M43 (NGC 1982): NIRCam parallel observations. [6]This filter contains an H$_2$ line at 3.23 μm but is largely dominated by the 3.3 μm AIB. [7]A "×" indicates that the observation has failed because of FGS loss.

3.1.1. NIRCam imaging

The selected NIRCam filters cover i) the 3.3–3.4 μm Aromatic Infrared Bands (AIBs), ii) the ro-vibrationally and rotationally excited lines of H$_2$ 1–0 S(1) at 2.12 and H$_2$ 0–0 S(9) at 4.69 μm, tracing the dissociation front, iii) the [FeII] line at 1.64 μm, tracing the ionization front, and iv) the Paschen Pa α and Brackett Br α atomic hydrogen lines, tracing the H II region. Each filter was paired with a reference filter centered on an adjacent wavelength for subtraction of the underlying continuum emission. We mapped the PDR region with a single pointing using a 4 point primary dither (Fig. 2). To avoid saturation, we used the RAPID readout mode with two groups per integration and two integrations per exposure. With 4 dithered pointings, this corresponds to 8 total integrations. The integration time per pixel from the reset to the second sample was about 21.47 s, corresponding to a total exposure time of 171.788 s. The minimum resulting signal-to-noise ratio on the extended emission toward the Bar template regions covered by NIRSpec is given for all filters in Table 1.

3.1.2. MIRI imaging

Data were obtained in i) the 7.7 and 11.3 μm filters including AIBs which, when combined, could provide a proxy for PAH ionization (e.g., Joblin et al. 1996; Galliano et al. 2008) and ii) the 15 and 25 μm filters dominated by continuum emission tracing warm dust in the H II and neutral region, similarly to

the corresponding WISE, *Spitzer*, and IRAS filters. We obtain a 3×3 mosaic using a three point dither pattern (3-POINT-MIRI-*F770W*-WITH-NIRCam) (Fig. 2). To prevent saturation given the brightness of the Bar, we use the FASTR1 readout pattern and the SUB128 imaging subarray.

3.1.3. NIRCam parallel observations

We obtained parallel NIRCam observations with the on-source MIRI imaging. The adopted filters cover i) the 3.3 and 3.4 μm AIB, ii) the vibrationally excited line of H$_2$ 1–0 S(1) at 2.12 μm, and iii) the Pa α and Br α lines. Also in this case, each filter was paired with a reference filter to estimate and be able to subtract the underlying continuum emission. The pointings, number of dithers, and dither pattern were set by those of the primary observations (on-source MIRI imaging). To accommodate the brightness of the Bar, we used the BRIGHT2 readout mode with two groups per integration, one integration per exposure, and the three dithered positions. The effective exposure time in this case results is 1159.569 s, corresponding to 580 s with correlated double sampling.

3.2. Data reduction

3.2.1. NIRCam

Given the evolving nature of the automatic pipeline producing the data available on MAST, we have chosen to reduce

our observations starting from the original _uncal files, that is those produced by the preliminary Stage 0, adopting the latest available development version of the pipeline at that time 1.7.3. Stage 1 corrects instrument signatures that need to be treated at the level of individual groups before ramp fitting, such as for dark current, nonlinearity detector response, and cosmic ray (CR) events. Given the intensity of the signal, we turned off the suppress_one_group option of the ramp fitting step to recover signal saturated after the very first sample. Stage 2 operates on the count rate images produced by Stage 1 removing the background -if dedicated files are provided-, calibrating each exposure individually to produce images in physical units of MJy sr^{-1} and rectifying the images for final combination with other images. The last stage combines the rectified exposures from multiple exposures, performing outlier pixel removal and astrometric alignment to produce the final products, i.e. drizzled and mosaicked images with their associated data catalogs and segmentation maps. We have chosen to independently combine the different dithers for each module and each filter. We have also tested the impact of different parameters. First, we have tried bypassing the outlier detection step. This step allows finding some bad pixels and cosmic-rays not corrected in the previous stage. Without this step, the final images show a strong "salt and pepper" pixeling effect.

On the short wavelength filters (F162M, F164N, and F212N), we detected some artefacts identified as wisps. They are due to straylight and are located at the same positions in each detector. The wisps are mainly on the B4 and A3 detectors and their positions depend on the filter, the detector, and the observation. To correct them, we selected polygons encompassing the wisps by hand. Then, we flagged these polygons as DO_NOT_USE in the DQ array. The wisps were removed because they were not considered further but as a consequence the noise was higher in these areas in the mosaic, because there is less information. We corrected for the $1/f$ noise by subtracting the median value of each row and then each column before the JWST pipeline stage 3 process. We first took care to apply a mask on all the bright sources when computing the median values for row and column subtractions and carefully inspected the results for any unintended consequences.

Finally, we improved the world coordinate system (WCS) alignment between the different mosaics by detecting unsaturated point sources in all detector images and comparing their positions with the astrometry from the *Gaia* DR3 catalog. The astrometry correction was at most of 0.3″. To get the flux-calibrated line maps continuum subtracted in erg cm^{-2} s^{-1} sr^{-1}, the maps (in MJy sr^{-1}) are multiplied by $10^6 \times 10^{-23} \times \Delta\lambda \times c/(\lambda_c)^2$ with $\Delta\lambda$ and λ_c the bandwidth and pivot wavelength of the filters from the NIRCam manual.

3.2.2. MIRI

As for the NIRCam observations, we reduced our observations starting from the raw data using the latest version of the pipeline and reference files available at that time (February 2023). The inter-pixel capacitance (IPC) step, correcting for the interpixel capacitance, was skipped in stage 1 as recommended by the instrument team because of poorly defined deconvolution kernels. Similarly, the Reset Switch Charge Decay (RSCD) step correcting for some ideal detector and readout effects was skipped because of the low number of groups per integration in our observations. Dedicated backgrounds were observed for the *F1500W* and *F2550W* filters and were subtracted from the data in stage 2 of the pipeline. As mentioned in Sect. 3.1,

background observations in the *F770W* and *F1130W* filters were not successful due to FGS loss of fine guidance control. The tweakreg step in stage 3 used to improve the alignment of the different input images was skipped because of the lack of point-like sources in the different filters, as well as the outlier detection step as we observed a deterioration of the final mosaics when applying this correction. For the *F2550W* filter, as most of the groups reached the saturation level for the pixels along the Bar, we skipped the jump step because of poor performance.

Moreover, we observed strong edge-brightening effects in the final mosaics attributed to straylight features in the SUB128 array flat fields (the SUB128 array is located at the top left of the detector), stronger at longer wavelengths (*F1500W* and *F2550W* filters). A first solution was to flag the affected left columns and top rows as DO_NOT_USE (about 15 rows and columns) so that they are not used in the final mosaic. For the *F2550W* a region around the Lyot mask has also been flagged. The number of rows/columns to flag has been selected for each filter as a trade off between having sufficient pixels for the overlap and removing pixels with poor quality. A better solution, used in this article, is to use the mosaics for flat field estimations with backprojection (projection of the computed mosaic back to the detector at the central position). Then the mosaics are recomputed using the estimated flat fields. Repeating this process with an additional deflagging of the affected columns/rows in each iteration, significantly improved signal recovery.

3.3. Line, AIBs, and continuum emission contributions to imaging bands in the NIRCam filters

Here we summarize our results regarding the fractional contributions of line, AIBs, and continuum emission to our NIRCam images (for a complete description see the Science Enabling Product 4 article, Chown et al. 2023). We computed synthetic NIRCam images from the stitched and co-added NIRSpec mosaic from Peeters et al. (2023). We did this by applying Eq. (5) of Gordon et al. (2022) to each spaxel. This approach is similar to what has been done with *Spitzer*/IRS data[2]. We call these images "synthetic images" in order to distinguish them from images observed by NIRCam.

We then decomposed each spaxel into line and continuum components (based on local baseline fit around prominent lines), and then calculated synthetic images from each of the line and continuum components. The fractional contribution of emission component i to imaging band j, is given by the ratio of the synthetic image of component i in band j to the synthetic image in band j of the total spectrum. Note that this measurement relies solely on NIRSpec data, and so it is not affected by any differences from NIRSpec and NIRCam data (such as flux calibration, resolution, etc.) – we investigate such differences in Chown et al. (2023).

Figures A.1–A.7 show the three template spectra (HII region, Atomic PDR, Dissociation Front DF3) presented in Peeters et al. (2023), illustrating the variation of the contribution of different lines into each imaging band. Figures in Chown et al. (2023) show the fractional contribution of continuum and the line of interest into corresponding imaging bands. We thus derive the following for the different lines, bands and the continuum:

– Fe II 1.64 µm: The F162M filter is dominated by continuum emission (> 80%), while F164N captures continuum, Fe II 1.64 µm line, and the H I (12–4) line (Fig. A.1). As a result,

---

[2] See, e.g., https://irsa.ipac.caltech.edu/data/SPITZER/docs/dataanalysistools/cookbook/14/

F164N–F162M primarily traces Fe II 1.64 μm, except where the H I (12–4) line contributes significantly.

– Pa α: The Pa α line contributes to 80–90% of the emission in F187N (Fig. A.2), without subtracting continuum using the F182M band. In F182M, continuum emission contributes 30–50%, while Pa α contributes 40–60%. Both F187N and F187N–F182M are well-correlated with the true Pa α line intensity, although some Pa α emission is self-subtracted in F187N–F182M.

– Br α: This line contributes 40–50% of the F405N flux, which is well-correlated with the true Br α line intensity. In the Bar (on-target) observations, the F480M filter can be used to trace the continuum underlying F405N. F480M traces the continuum well with a small contribution from an H I line or an H_2 line (Fig. A.3). F405N–F480M flux is overall a good measure of Br α intensity, but suffers from more scatter than the F405N vs. Br α correlation.

– H_2 1–0 S(1) 2.12 μm: The fractional contribution of continuum emission in F212N is higher than that in F210M over a large area. This is due to bright H I and He I emission lines that fall in the F210M filter but fall outside of the F212N filter (Fig. A.4). This results in a negative flux in the F212N–F210M image in a significant fraction of area closer to the exciting sources. Note also that the He lines that are close to H_2 2.12 μm contribute to F212N at a comparable degree to the H_2 line except in regions that are sufficiently far away from the exciting sources.

– H_2 1–0 O(5) 3.24 μm: This line is located on a shoulder of the 3.3 μm AIB (Fig. A.5). The contribution of this line to F323N is 5–15% across the observed area. The correlation of the F323N synthetic image with the actual line intensity is poor, and subtracting continuum as traced by F300M does not improve this correlation.

– H_2 0–0 S(9) 4.69 μm: In the northern half of the observed area with NIRSpec, H I lines contribute to the observed F480M flux but not to F470N (Fig. A.6). Similar to the situation with H_2 1–0 S(1) 2.12 μm in the F212N filter, this results in a negative flux in the F470N–F480M image. However, in the southern half (far from the exciting sources), F480M works reasonably well at subtracting continuum in F470N to estimate the intensity of the H_2 4.69 μm line, although rising continuum towards longer wavelengths underestimates the line flux probed by F470N–F480M.

– The 3.3 μm AIB: This AIB is the dominant component of the emission in the F335M filter. This AIB contributes 50–60% of the F335M flux near the exciting sources, and 70–80% at remaining positions. F300M traces the continuum on the shorter wavelength side of F335M reasonably well (Fig. A.7). F335M–F300M is thus a good tracer of the integrated strength of the 3.3 μm AIB.

A detailed analysis of a full set of lines will be presented in the science enabling product and the associated article (Chown et al. 2023).

4. Morphology of the Orion Nebula inner region

With their high angular resolution and unparalleled sensitivity, NIRCam and MIRI unveil the structures at very small scales of the Orion Nebula (0.1 to 1″ from 2 to 25 μm, equivalent to 2×10^{-4} to 2×10^{-3} pc at the Orion distance of 414 pc). It displays an incredible richness of substructures, as well as previously hidden stars and even background galaxies. In this section, we present several prominent features arising in the images within the inner region of the Orion Nebula (M42), i.e. the fields centered on the Bar.

Figure 3 shows composite NIRCam images in three selected filters (F187N, F335M, and F470N). The F187N filter captures the distribution of ionized gas via the bright Pa α, F335M traces mostly emission from the AIB 3.3–3.4 μm aromatic and aliphatic CH stretching mode bands and F470N traces the dust continuum and the high excited H_2 0–0 S(9) pure rotational line. Figure B.1 shows composite MIRI images in the three selected filters $F770W$, $F1130W$, $F1500W$. These filters image the 7.7 and 11.3 μm aromatic bands and the continuum emission from hot/warm dust at thermal equilibrium. The emission at 15 μm is mainly produced by very small carbonaceous grains whereas at 25 μm slightly larger grains can contribute (e.g., Compiègne et al. 2011). In Appendix B, all the images obtained in the filters listed in Table 1, and for some gas lines continuum subtracted, are presented.

A schematic view of the Bar inferred from both these JWST observations and the literature on previous observations from visible to millimeter is presented in Fig. 5. We are viewing the main ionization front almost edge-on along the Bar.

4.1. Ionized gas, crenellations, bow-shocks and YSOs

In Fig. 3, the ionized gas (in blue) comes from the MIF extending from the Trapezium grouping of stars to the Bar. Beyond the Bar, the MIF is primarily photoionized by Θ^2 Ori A (O'Dell et al. 2017a). Due to intense ultraviolet and ionizing radiation, hot and ionized gas is photoevaporating away from the MIF. H I and He I lines observed toward the Huygens Region at visible-wavelengths are blue-shifted, by $\simeq 10$ km s^{-1}, with respect to the molecular gas emission (O'Dell et al. 2023). This velocity difference approximately agrees with that inferred from observations of H and He radio recombination lines (e.g., Goicoechea et al. 2015; Cuadrado et al. 2019).

In the NIRCam images, ionized gas flows from the IF of the Bar (see panel G in Figs. 3 and 4) are not easy to discern because they are seen in the foreground of the MIF emission. The NIRCam and MIRI images do not show any AIBs and H_2 emission that would be associated with the photoevaporating flows from the IF of the Bar. The AIBs and H_2 emission in front of the Bar most likely originate from the surface of the OMC-1. This surface is perpendicular to the line of sight and is illuminated by the Trapezium cluster, making it a face-on PDR [3].

On the background OMC-1 surface, several structures as shown in panels A and B in Fig. 4 are spatially resolved. These types of features are not the only ones and several of them were observed at visual wavelengths with the HST. They were called "Crenellations" by O'Dell et al. (2015). The interaction of collimated jets and outflows from protostars inside the molecular cloud likely drives the shocks that create these structures at the surface of the cloud (see also Kavak et al. 2022b,a). In order to study whether some of these structures are "apparent" structures produced by extinction variations or the edges of dense molecular gas structures, high angular resolution molecular line tracers are needed.

One of the largest outflows with highly blue-shifted features (e.g., O'Dell et al. 1997; O'Dell & Henney 2008) is HH 203 and 204, localized southwest of θ^2 Ori A, are well seen in the Pa α, Br α and [FeII] line NIRCam images and in the continuum filters

---

[3] The emission from this background face-on PDR was previously observed with *Herschel* in other PDR tracers, especially in high-J CO, CH$^+$ lines (Parikka et al. 2018) and [OI] 63 and 145 μm and [CII] 158 μm (Bernard-Salas et al. 2012), as well as, with *Spitzer* in AIBs (Knight et al. 2022).
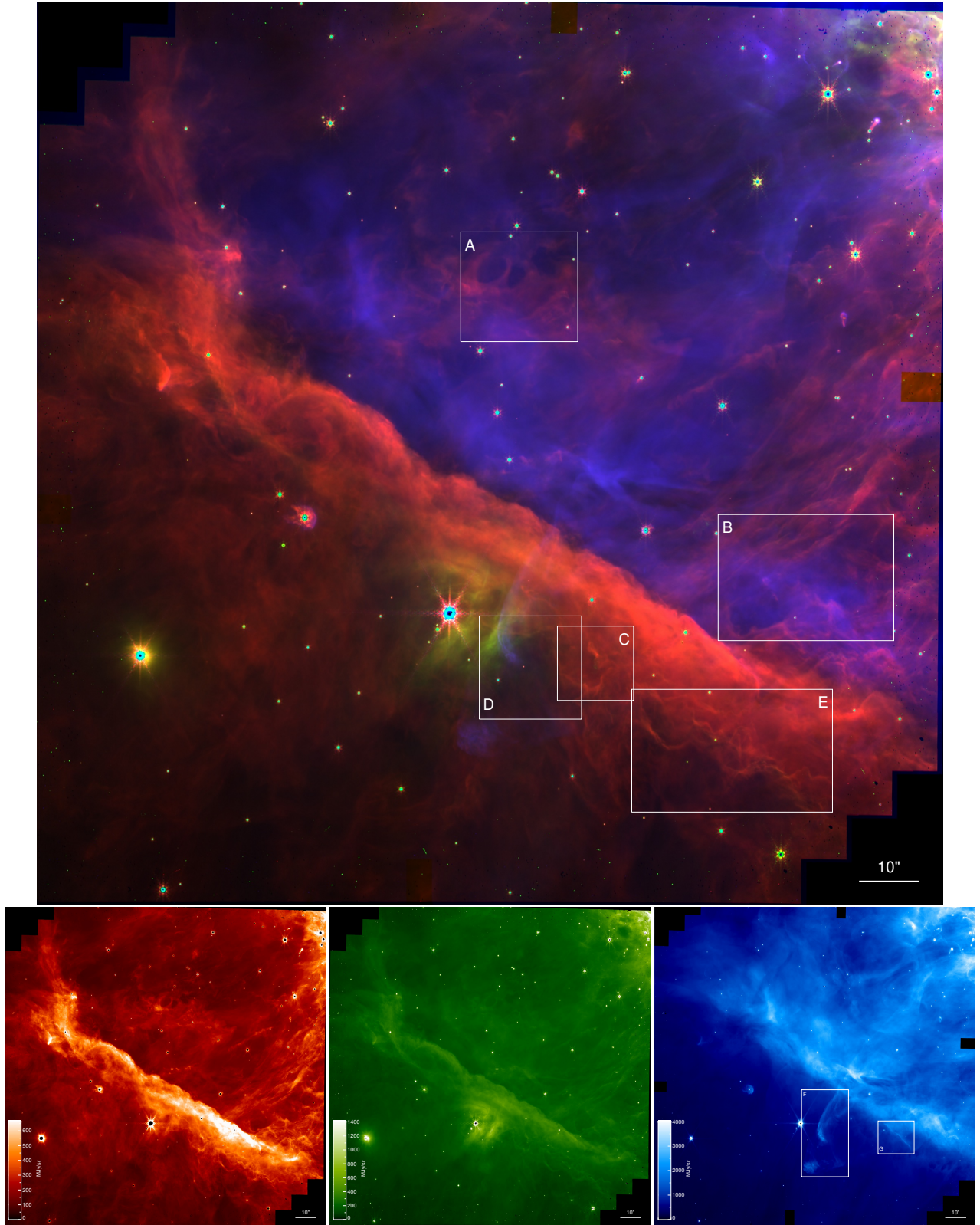
Fig. 3. Inner region of the Orion Nebula as seen by the JWST's NIRCam instrument with north up and east left. In the upper panel, three images in different filters were combined to produce an RGB composite image: F335M (red), F470N (green) and F187N (blue) that trace emission from hydrocarbons (AIBs), dust and molecular gas (H_2 0–0 S(9) line), and ionized gas (Pa α line), respectively. The individual images used to make the RGB composite are shown in the lower panels. No continuum was subtracted. The size of the images is ~$150'' \times 150''$. Most prominent is the Bar, a wall of dense gas and dust that runs from the top left to the bottom right in these images, and that contains the bright star θ^2 Ori A O9.5 Vp which shines in the center of the Bar. The Bar and the surface of the Orion Molecular Cloud 1 (seen in the background in the front of the Bar) are illuminated by a group of hot, young massive stars forming the Trapezium Cluster, located just off the top right of the image. White boxes (labeled A, B, C, D, E, F and G) delineate regions of particular interest zoomed in and shown in Fig. 4.
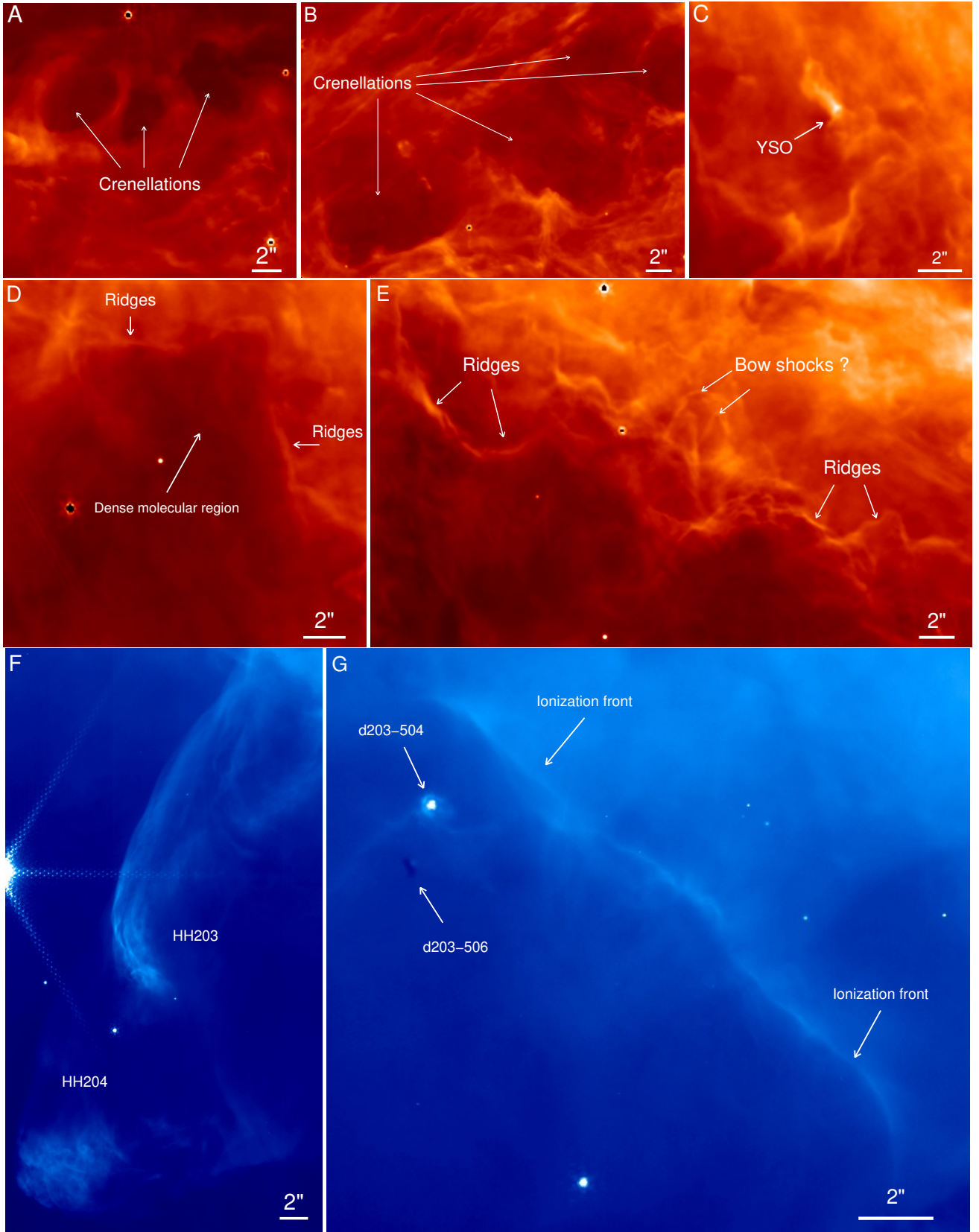
Fig. 4. Zoom into the F335M (red) and F187N (blue) areas shown in Fig. 3. A, B: several crenellations that may result from the interaction of collimated jets and outflows from protostars inside the molecular cloud. C: bright substructure, likely a YSO candidate, detected with ALMA (Fig. B.5). D, E: irradiated molecular edges showing many patterns such as ridges. F: features known as HH 203 and 204 driven by large outflows. G: Ionisation front of the Bar with the two irradiated proto-planetary disks 203–504 and 203–506.

at shorter wavelengths (panel F in Figs. 3 and 4 and figures in Appendix B). HH 203 is a well defined bow-shock with low ionization characteristics at its end. It is driven by a high-velocity jet that emerges into the area ionized by θ^1 Ori C or the nearest (in the plane of the sky) star θ^2 Ori A. HH 204 is almost at the same position angle as HH 203 but shows a different structure. Its top is a flocculant structure (that includes low ionization characteristics) and no jet is visible. These structures are not detected in H_2 line emission (Sect. 5.2 shows the H_2 emission in the map and the spatial profile towards the cut 5 which indicate that the H_2 emission is associated with the Bar and not with the bow shock of HH 203). This supports the suggestion that these flows interact with the ambient ionized gas of the nebula and not the molecular gas (e.g., O'Dell & Henney 2008).

NIRCam images in the F470N and F480M filters reveal for the first time strong emission in the surroundings of the bright star θ^2 Ori A (at about ~8″ or 0.015 pc from the star for a distance of 414 pc). These previously unknown features are also visible in F277W, F300M, F323N and F335M filters. A stellar wind from the θ^2 Ori A star most likely forms these features. A bow wave around the θ^2 Ori A star is probably moving into the MIF. The dynamical and radiative impact of θ^2 Ori A is influencing and complicating its nearby environment. O'Dell et al. (2017a) showed that foreground objects near this location are illuminated by θ^2 Ori A.

A very bright substructure located in the southern part of the Bar shows a very particular structure ~1000 au in size for a distance of 414 pc (see panel C in Figs. 3 and 4). This structure is also visible with ALMA (see Fig. B.5 where it appears as a globule) and might correspond to the surroundings of a protostellar source embedded in the highly irradiated environment of the Bar (Goicoechea et al., in prep.). No MIRI point source is detected at this position, probably because the extended emission from the Bar is very bright and dominates the continuum emission. This indicates that this YSO is most likely too cold to emit strongly at mid-infrared wavelengths. The structures around this YSO are very bright in the H_2 0–0 S(9) and 1–0 S(1) lines in the NIRCam and Keck (Habart et al. 2023) maps (see Fig. B.5) but also in the AIB emission (see panel C in Fig. 4). This emission likely arises from a combination of irradiated shocks from the outflow and PDR emission. Finally, several bright emission features associated with embedded proplyds are detected in the Bar and in front of it (e.g., panel G in Figs. 3 and 4). The proplyds detected within the inner region of the Orion Nebula are discussed in Sect. 6.

4.2. Crenellations on the Bar

One of the most striking features from the NIRCam and MIRI images, and in particular in filters probing AIBs and H_2 emission, is that the molecular cloud border in the background and the Bar appears hyper structured, most likely turbulent (e.g., Goicoechea et al. 2016). In the Bar, lots of patterns are apparent such as crenellated structures or ridges (e.g., panels D, E in Figs. 3 and 4). The upper west corner of panel E in Fig. 4 coincides with a region where the Bar has no sharp boundary, a region labeled "SW-Gap" in Fig. 24 of O'Dell et al. (2015). In this zone, a number of crenellated structures were seen with HST. These features are both detected in the NIRCam filters dominated by the ionized gas and continuum below 3μm. As suggested by O'Dell et al. (2015), these structures are very likely bow shocks forming in the tilted portion of the Bar or the foreground Veil. On the other hand, in the regions further inside the Bar (e.g., panel D or panel E from upper east corner to west corner), the structures seen in the NIRCam and MIRI filters probing

AIBs and H_2 lines emission likely correspond to the edges of dense molecular gas inside the Bar. Most of these structures are in fact well seen in the submm HCO^+ ($J = 4$–3) emission (with ALMA, see Sect. 5) which is sensitive to molecular gas density variations.

This highlights a very intricate irradiated cloud surface and sub-dense structures at such small scales that they were inaccessible to previous observations. The surge of stellar energy sculpts this region exhibiting an incredible richness of substructures. The F335M filter is essential for bringing out the high-textured structure of the UV irradiated molecular cloud surfaces. The aromatic emission traces a combination of cloud density and strength of the local FUV field (see Sect. 5.1). The F335M filter provides one of the highest resolution views of the outer molecular layer of the PDRs available with JWST. Intricate fine details of how interstellar matter is structured at small scale is thus revealed. At the cloud edge, AIB emission is more restricted to the atomic H layers of the PDR than the H_2 line emission (see Sect. 5). With the high incident FUV radiation field on the Bar, molecules in general are expected to survive longer in the shielded environment offered by the dense Bar or OMC-1. However, emission in highly rotationally and ro-vibrationally excited H_2 lines require FUV photons to be pumped. These lines are therefore observed at the photodissociation front more specifically at the H^0/H_2 transition where atomic hydrogen becomes molecular. Consequently, the subtracted continuum H_2 line images (e.g., the H_2 0–0 S(9) and 1–0 S(1) lines at 4.69 and 2.12 μm) highlight the irradiated edges of dense molecular structures. A detailed comparison between the atomic and molecular phase tracers across the Bar PDR is given below in Sect. 5.

5. Transition from ionization front to H^0/H_2 dissociation front

In this section, we focus on the Bar, a prototypical highly irradiated dense PDR. Figures 6–11 and B.5 show close-up maps and surface brightness profiles of the Bar viewed edge-on. A gradual structure is evident when moving away from the excitation source as the ionization front, the AIB and H_2 emission layers appear successively, in agreement with previous studies (e.g., Tielens et al. 1993). However, instead of a smooth PDR transition, multiple ridges in AIB and H_2 emission are spatially resolved for the first time. In addition JWST unambiguously reveals very sharp edges (on scales of ~1″ or 0.002 pc) and rich small-scale structures (with typical widths of ~0.5−1″ or ~0.001–0.002 pc). This is in agreement with previous high spatial resolution ALMA HCO^+ emission maps (Goicoechea et al. 2016) which showed a highly sculpted interface. Along with analysis of high-J CO and CH^+ *Herschel* observations and H_2 pure rotational lines from ISO, Joblin et al. (2018) concluded that the emission of these tracers arises from a thin (a few 10^{-3} pc), high thermal pressure ($P \sim 10^8$ K cm^{-3}) layer at the surface of the molecular region. However, the corresponding structures were unresolved in most tracers until now.

In the following, we use the notations of the scheme in Fig. 5 and Table 2 for the physical quantities related to the Bar PDR. In particular, the assumed distance to the Bar is 414 pc (Menten et al. 2007). This value is slightly higher or similar to more recent estimates using *Gaia* observations (see annotations in Table 2). We use the notation l_{PDR}^{los} the length of the PDR along the line of sight toward us and d_{PDR} for the depth in the PDR from the IF. N_H^{los} and A_V^{los} are the column density and visual extinction along
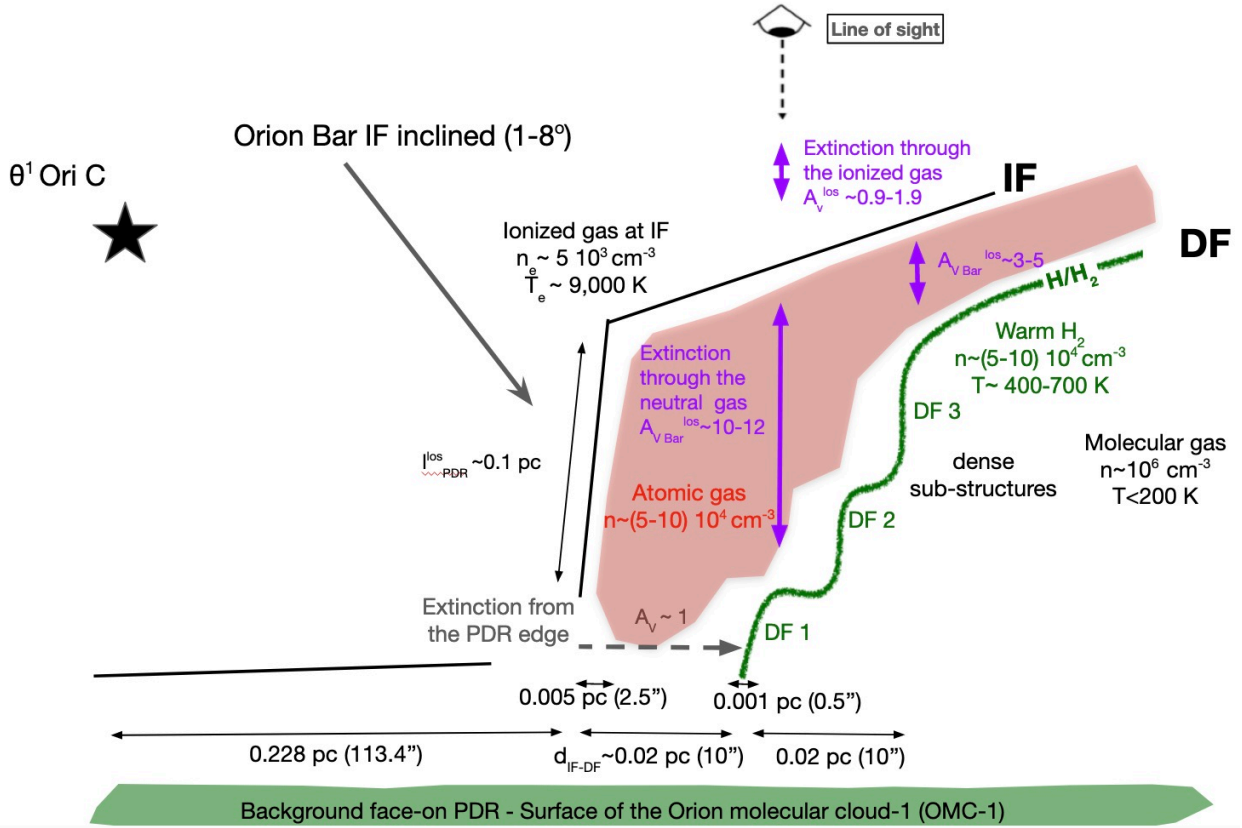
Fig. 5. Schematic view of the Bar inferred from JWST and previous observations from visible to mm (e.g., Jansen et al. 1995; Wen & O'Dell 1995; O'Dell 2001b; Pellegrini et al. 2009). It displays the main features discussed in detail in the core of this article, and inferred from both the imaging observations (this work) and NIRSpec spectroscopic observations (Peeters et al. 2023). We note that for clarity the dimensions perpendicular to the Bar are not to scale, the true spatial scales being explicitly given in the annotations. The adopted distance to the Bar is 414 pc. In addition, the sketch does not include foreground material, which includes a layer of ionized gas (O'Dell et al. 2020) and, closer to the observer, layers that are grouped together under the designation as the Veil (e.g., van der Werf et al. 2013; Pabst et al. 2019, 2020).

the line of sight toward us. $N_{\rm H}$ and $A_{\rm V}$ are the column density and visual extinction in the UV illuminating direction (perpendicular to the Bar).

5.1. Spatial distribution of the AIB emission

We first analyze the surface brightness profiles of the filters probing the AIBs and continuum emission along the direction going away from the sources of UV illumination. In order to probe variations across the PDR, several cuts perpendicular to the Bar from southwest to northeast are shown in Figs. 6 and 8. This allows us to probe the flux variations along the entire illuminated interface. An approximate position of the IF has been marked in maps and profiles as a vertical line, which corresponds to the emission peak of the [FeII] 1.64 μm line and the rise of the AIBs and gas lines in the atomic zone (e.g., [OI] 63 and 145 μm). The different components observed in the AIB emission profiles in the different PDR zones are annotated (Fig. 7) and discussed next. Our high spatial resolution JWST study permits filling in the near IF portion of the Bar's PDR that the study of Henney (2021) based on Herschel data did not allow (cf. his Fig. 5).

5.1.1. Steep density rise at the IF

At first glance, the spatial distribution of the AIB filter emission profiles follows the same trend as we move across the Bar, a steep increase at the IF position, followed by a slower decrease

(with a typical scale of 10″ or ∼ 0.02 pc, see Figs. 7, 6 and 8). At first order, the AIBs surface brightness is proportional to the column density of the band carriers and to the local FUV flux strength, $I \propto N_{\rm H}^{\rm los} \times [{\rm C/H}] \times G_0 \times e^{-\tau_{FUV}}$ with $N_{\rm H}^{\rm los} = n_{\rm H} \times l_{\rm PDR}^{\rm los}$ and [C/H] their carbon abundance. The column density is along the line of sight to us while the opacity τ_{FUV} is in the FUV illuminating direction, perpendicular to the Bar. The initial brightness increase is expected due to a large increase in dust column density at the IF, while the slower decrease is expected due to the extinction of the incident UV irradiation field. What is noteworthy is that the emission spatial profiles show an extreme climb over few sub-arcsecs just after the IF. The emission peak arises 1″ to 2.5″ (0.002–0.005 pc) from the IF depending on the position in the Bar (see Fig. 6). Such a sharp density rise is expected due to the sharp decrease in gas temperature at the IF if the thermal pressures in the ionized and neutral regions are of similar magnitude, as discussed below. In addition, the extreme rise of the emission profile could put strong constraints on the tilt angle θ of the PDR between the plane of the irradiated surface and the line of sight. This is discussed in Peeters et al. (2023) and will be investigated in more detail in a future work.

5.1.2. FUV dust extinction and density in the atomic PDR

Just after the rise, one can clearly observe in the AIB profiles a rapid decrease which must result from the FUV radiation field decreasing with depth inside the PDR as a consequence of the dust extinction. Fluxes in filters centered on

Table 2. Parameters employed or derived for the Bar.

Parameter	Value	Reference
Distance	414±7 pc [a]	Menten et al. (2007)
	1″ = 0.002 pc	
Projected distance, d_{proj}, between θ^1 Ori C and the IF	0.228 pc	
Transverse size l_{PDR}^{los}	∼0.1 pc	Peeters et al. (2023)
G_0 at IF	∼(2.2–7.1) × 10^4	Peeters et al. (2023)
FUV dust cross-section σ_H	6.5×10^{-22} cm^2/H	Cardelli et al. (1989); Blagrave et al. (2007)
		Schirmer et al. (2022)
$R_V = A_V/E(B-V)$	5.5	Cardelli et al. (1989); Blagrave et al. (2007)
A_V/N_H	3.5×10^{-22} mag/cm^{-2}	Cardelli et al. (1989); Blagrave et al. (2007)
Density in atomic PDR n_H	(5–10) × 10^4 cm^{-3}	This article (Sect. 5.1)
Density at the IF n_e	5×10^3 cm^{-3}	Weilbacher et al. (2015)
Temperature at the IF T_e	∼9×10^3 K	Weilbacher et al. (2015)
Distance between IF and DF d_{IF-DF}	0.02–0.04 pc	This article (Sect. 5.2.1)
Average atomic density between IF and DF	4.6×10^4 cm^{-3}	This article (Sect. 5.2.1)
Density from NIR H$_2$ n_H	($3.5) \times 10^4$ to ×10^5 cm^{-3}	Peeters et al. (2023)
Temperature at the DF T	∼400–700 K	Allers et al. (2005), van de Putte et al. (2024)

Notes. [a]The adopted distance is based on the Menten et al. (2007) study using radio very long baseline interferometry. We underline that more recent observations, including *Gaia*, point to slightly lower or similar values. Kounkel et al. (2017) used the Very Large Baseline Array and measured a distance of 388±5 pc toward the Orion Nebula Cluster (ONC). This distance corresponds to the weighted average distance of all the stars located toward the ONC, including the Trapezium. Kounkel et al. (2018) used *Gaia* DR2 and measured an average distance of 386±3 pc for the ONC. However, other studies based on *Gaia* DR2 parallaxes such as Binder & Povich (2018); Großschedl et al. (2018); Kuhn et al. (2019) quote distances for the ONC of 410 pc, 400–410 pc and 403^{+7}_{-6} pc, respectively which are near the estimate from Menten et al. (2007). Großschedl et al. (2018) suggested that the about 10 pc difference compared to the literature value can be seen as an estimate of remaining systematic uncertainties. In Appendix A of Kuhn et al. (2019), they compare their distance estimate to one from Kounkel et al. (2018) and discuss effects of the three-dimensional structure of Orion A. Moreover, one should note that these distances correspond to the distances of the stars and not the one of the molecular cloud and the Bar. New *Gaia* releases (in combination with new trigonometric parallax) will provide even more accurate distance determinations. For simplicity, we choose to assume the distance of 414±7 pc from Menten et al. (2007) in order to remain consistent with Berné et al. (2022b). The difference in distance values has anyway no important implications for the results presented in this article.

AIBs are most likely dominated by the emission produced by (sub)nanometric particles including large molecules (PAHs) stochastically heated, which is proportional to the FUV radiation field strength. To visualize the decay of the FUV flux, the curve $\exp(-\tau_{FUV})=\exp(-\sigma_H N_H)$ with σ_H the dust FUV extinction cross-section per proton, and N_H the column density from AIB emission peak (along the UV illuminating direction, perpendicular to the Bar), is plotted on Fig. 6 (dotted line). The parameters employed to reproduce the initial part of the observed decay are given in Table 2. We assume σ_H, R_V and A_V/N_H in agreement with the extinction curve measured in the Orion Nebula by Cardelli et al. (1989) and as refined by Blagrave et al. (2007). These values differ from that of the average measured in the ISM ($R_V = 3.1$ and $A_V/N_H = 5.3 \times 10^{-22}$ mag cm^{-2}) and lead to an increased penetration of FUV photons compared to the dust found in the diffuse ISM[4]. Then, in order to compute the column density N_H, we assumed after the initial rise in density (i.e., after the emission peak) a constant density n_H in the atomic PDR as in Arab et al. (2012) and Schirmer et al. (2022). N_H is then given by $n_H \times d_{PDR}$ with d_{PDR} the distance from the emission peak. The

density n_H is adjusted to reproduce the initial part of the observed decay (d_{PDR} ∼0.002–0.01 pc). We derive n_H=(5–10)×10^4 cm^{-3} (see Fig. 6). The density value range we derived in the atomic PDR is in agreement with the location of the H^0/H$_2$ transition obtained with NIRCam (see Table 2) as discussed in Sect. 5.2.3 as well as estimates from atomic gas FIR lines (e.g., [CII] and [OI] fine-structure lines, Bernard-Salas et al. 2012). It also agrees with estimates from the Raman-scattered wings of hydrogen Hα lines in the Bar (Henney 2021).

The density we derived in the atomic PDR is significantly higher (factor 10–20) than the electron density n_e derived at the IF which is about ∼5×10^3 cm^{-3} (see Figs. 26 and 27 in Weilbacher et al. 2015). In a D-critical IF[5] (that can be expected in a blister HII region), the pressure in the neutral gas at the close-back of the IF is expected to be a factor of 2 higher than in the ionized gas in the close-front of the IF. A strong rise in density is then expected to compensate for the much stronger temperature decrease between the ionized and neutral region. In that case, a pressure of about ∼2×10^8 K cm^{-3} is expected in the neutral atomic region[6], and given our density estimate, this would mean a temperature of a few 10^3 K.

[4] This lower FUV extinction is in agreement with the findings of Schirmer et al. (2022) who fit *Spitzer* and *Herschel* observations with the THEMIS dust evolution model (Jones et al. 2017). Despite the poor resolution, a radiative transfer model of the Bar including the evolution of dust grains (size, abundance, properties) allowed them to highlight a strong depletion of the subnanometric grain population and a size distribution shifted towards larger particles compared to the diffuse ISM. A more recent study with JWST data confirms this result (Elyajouri et al. 2024).

[5] In the usual classification of IF types (first established by Kahn 1954; Axford 1961, and summarized in usual textbooks, e.g., Spitzer 2004; Draine 2011), a D-critical front travels at subsonic speed with respect to the neutral gas, while the ionized gas is expelled at the speed of sound with respect to the front.

[6] The electron temperature T_e derived at the IF is of the order of ∼9×10^3 K (see Figs. 24 and 25 in Weilbacher et al. 2015) which gives a thermal pressure of $P_{th/k} = 2 \times n_e \times T_e \sim 10^8$ K cm^{-3}.
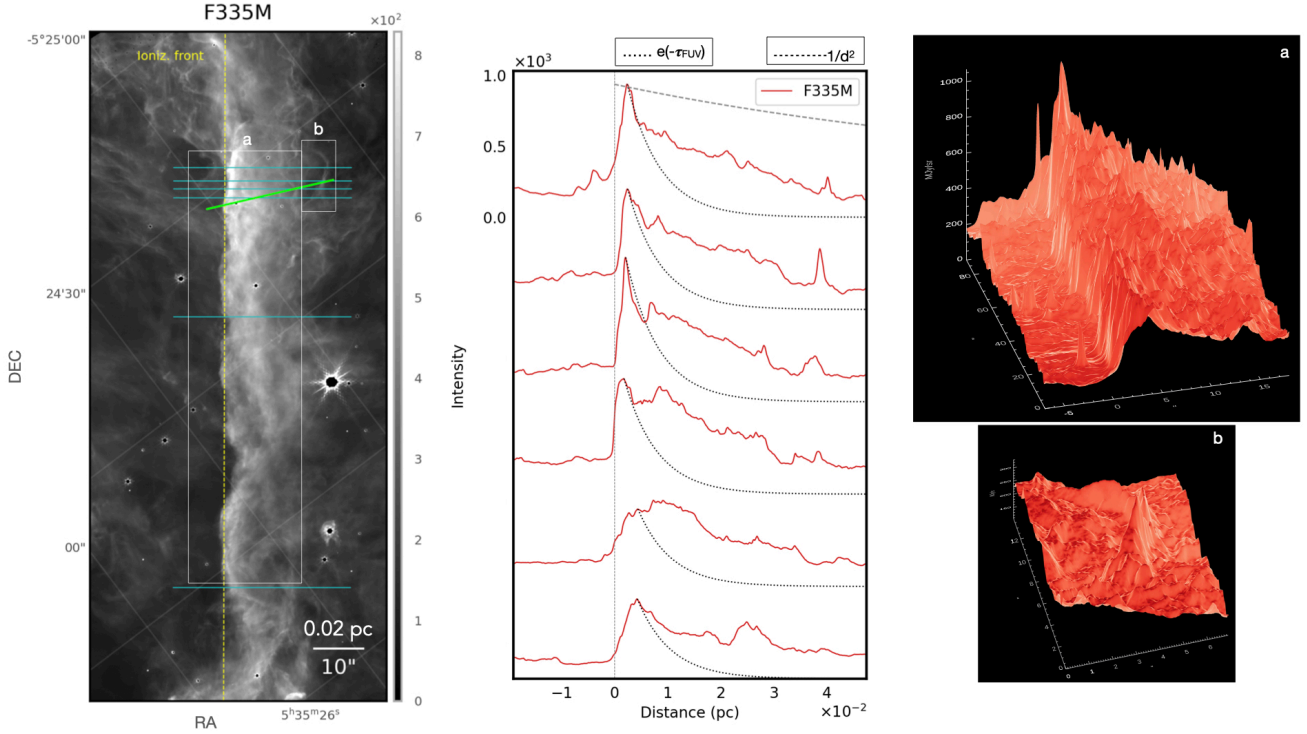
Fig. 6. Spatial distribution of the F335M filter tracing mostly the AIBs CH stretch emission in the 3.17–3.54 µm range. *Left*: map in the F335M filter centered on the Bar and rotated so that the ionizing radiation strikes the Bar from the left. Units are in MJy sr^{-1}. The vertical dashed line (in yellow) delimits the average position of the IF. The horizontal lines (in cyan) give the position of 6 cuts, perpendicular to the Bar (the top cut toward the south), displayed in the middle panel. the inclined line (in green) gives the position of the cut obtained from the NIRSpec field, shown in Fig. 11. The boxes (in white) delineate the regions of the 3D surface brightness maps shown on the right panels. *Middle*: surface brightness profiles in the F335M filter shown as a function of the distance from the IF. The FUV extinction decrease in the Bar (dotted lines) and the expected geometric dilution factor of the incident FUV field intensity from the O7-type star θ^1 Ori C (dashed lines in the upper cut) are both normalized to the peak of the emission in the F335M filter for comparison. The vertical dotted-dashed lines indicate the average position of the IF, also indicated in yellow in the left panel. *Right*: 3D maps of the surface brightness profile in two regions defined in the left panel. For a, the grid is $24'' \times 85.2''$. It shows the sharp rise in brightness along the Bar. For b, the grid is $6.6'' \times 13.3''$. It shows bright fronts superimposed on the Bar emission. The orientations of the plots are optimized for the best viewing angle.
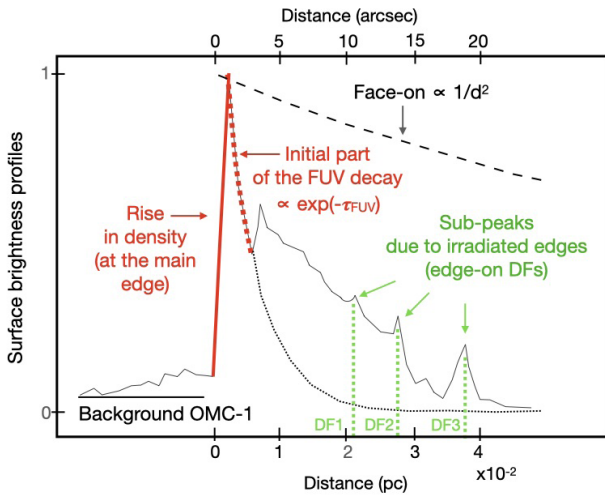
Fig. 7. Annotation of the different components seen in the AIB surface brightness profile perpendicular to the Bar. These are shown for cut 2 in filter F333M from Fig. 6, where several other cuts through the Bar are shown.

5.1.3. Extended emission and secondary peaks towards the molecular region

Another important characteristic of the observed emission profiles is that when entering the PDR, the emission decays to a

nonzero plateau that extends into the molecular region (Figs. 7 and 6). This extended emission is most likely due to irradiated atomic material along the line of sight located in front of the molecular region, in the foreground face-on PDR surface layer (as seen in geometry on Fig. 5). This emission may originate in the flattened region that is still illuminated directly by the ionizing stars. The MIF turns up at the Bar and then continues a flatter rise further away (as illustrated in the lower part of Fig. 13 in O'Dell & Harris 2010). A detailed *Spitzer* study revealing what is behind the Bar and supporting this geometry is published by Rubin et al. (2011). For AIBs and dust continuum emission, the further inside the Bar, the greater the face-on PDR contribution with the FUV radiation in the Bar being rapidly attenuated.

Furthermore, in the decaying part of the profile, several secondary peaks are visible (Figs. 7 and 6). This might be associated with multiple irradiated ridges with varying densities. These ridges are located after the main edge in the FUV illuminating direction. The sub-peaks in the region where the hydrogen is mostly molecular ($d_{PDR} > 0.02$ pc) spatially and individually coincide with strong H_2 line emission peaks (Fig. 9), hinting that these AIB emission peaks arise from the material at or close to the DF. Some AIBs sub-peaks are very pronounced (such as the one at $d_{PDR} = 0.04$ pc, Fig. 6, panel b). For those, the AIB emission sub-peak is observed slighlty shifted (by ~0.2'') from the H_2 emission peak (i.e. H_2 is observed closer to the Trapezium). In order to investigate this shift in detail, radiative transfer calculations are required.
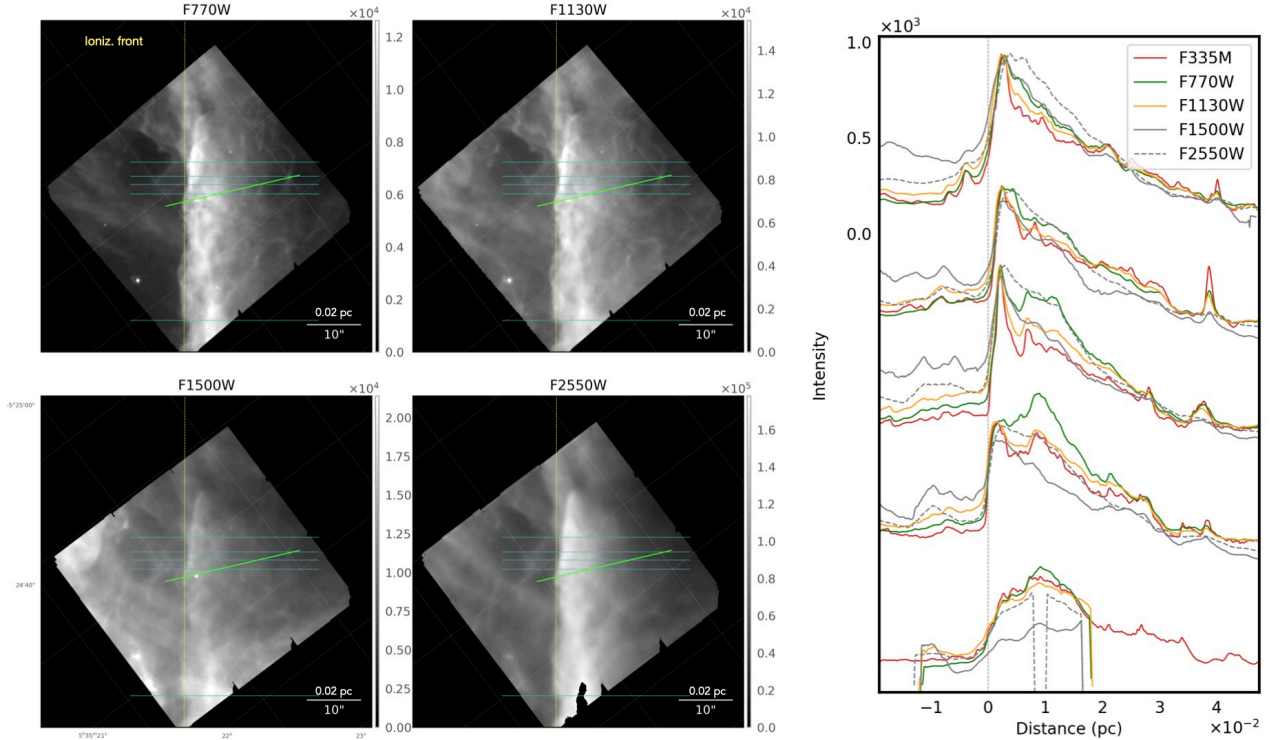
Fig. 8. Spatial distribution of the MIRI filters tracing the AIBs at 7.7 and 11.3 μm and continuum dust emission. *Left*: Maps in the MIRI filters. Same as Fig. 6 for the vertical and horizontal lines. *Right*: Surface brightness profiles of the F335M NIRCam filter (in red), and *F770W* (in green), *F1130W* (in yellow), *F1500W* (solid grey) and *F2550W* (dashed grey) MIRI filters as a function of the distance from the IF. In order to compare the brightness profiles along each cut in the Bar, the mean emission background in front of the Bar (face-on background PDR contribution) has been subtracted to each filter's cut and then scaled to the NIRCam F335M filter maximum amplitude. The background emission level subtracted to the profiles is about 160, 1700, 3200, 4900, 34 000 MJy sr^{-1} for the F335M, *F770W*, *F1130W*, *F1500W* and *F2500W* filters, respectively. The vertical dotted-dashed line indicates the average position of the IF, also indicated by yellow line in the left panel.

5.2. Excited dense molecular gas

In this section, we analyze the distribution of the excited dense molecular gas traced by H$_2$ emission in order to probe the gas physical structure and the location of the key chemical transitions occurring in the molecular PDR. With JWST, we are for the first time able to spatially resolve the emission profiles of both the high rotationally and vibrationally excited H$_2$ lines (see Figs. 9, B.5 and 11). Our NIRCam observations show a very good agreement with Keck/NIRC2 observations (Habart et al. 2023) in terms of vibrationally excited line distribution and intensity. In the following, we examine the highly structured H^0/H$_2$ dissociation fronts towards the Bar as well as the remarkably similar spatial distribution between the highly rotationally (0–0 S(9)) and vibrationally (1–0 S(1)) excited H$_2$ lines and the HCO$^+$ line J = 4–3 emission observed with ALMA. The spatial distribution of the emission lines as a function of the geometry of the DF surface layer, density variation with depth into the PDR and extinction along the line of sight is now discussed in detail.

5.2.1. Highly structured H^0/H$_2$ dissociation fronts

In Figs. 9, 10 and 11, the NIR H$_2$ line emission (delineating the H^0/H$_2$ transition) show several bright ridges which are spatially resolved and small scale structures. The H^0/H$_2$ fronts appear highly structured with several ridges and the emission rise is extremely sharp with a width of 0.5 to 1″ (0.001–0.002 pc or

200–400 AU). The ridges run parallel to the Bar but a succession of bright substructures is also observed from the edge towards the molecular region. This is particularly clear in the southwest part of the Bar which corresponds to the upper part of the map displayed in Fig. 9. In this area, the structure of the Bar is very complex and irregular. The H$_2$ emission ridges appear in an area that starts at about 10″ from the IF (d_{PDR}=0.02 pc) and up to 20″ (d_{PDR}=0.04 pc) as shown in Fig. 9. We interpret the three main ridges that appear as three edge-on portions of the DF surface which are successively more and more distant from the IF. These edge-on portions of the DF, denoted DF1, 2, 3 thereafter, are located at a projected distance from the IF of d_{PDR} ∼0.02 pc, 0.027 pc, and 0.038 pc respectively, as indicated by vertical dashed lines in Figs. 9 and 10. The DF2 is the one which coincides best with the average position of H$_2$ emission ridges all along the Bar.

A terraced-field-like structure. A terraced-field-like structure with several steps seen from above as shown in Fig. 5 can explain the succession of H$_2$ ridges across the Bar. In that geometry, each H$_2$ emission ridge corresponds to a portion of the DF seen edge-on, i.e., a step. Since highly rotationally and rovibrationally excited H$_2$ emission profiles are sensitive to the gas density, the very narrow and bright ridges must be due to irradiated dense material. For low density interface, the H$_2$ emission is spatially more extended and weaker. In the isobaric hypothesis, as discussed previously, the gas density rises as the gas cools at the DF (e.g., Allers et al. 2005; Joblin et al. 2018).
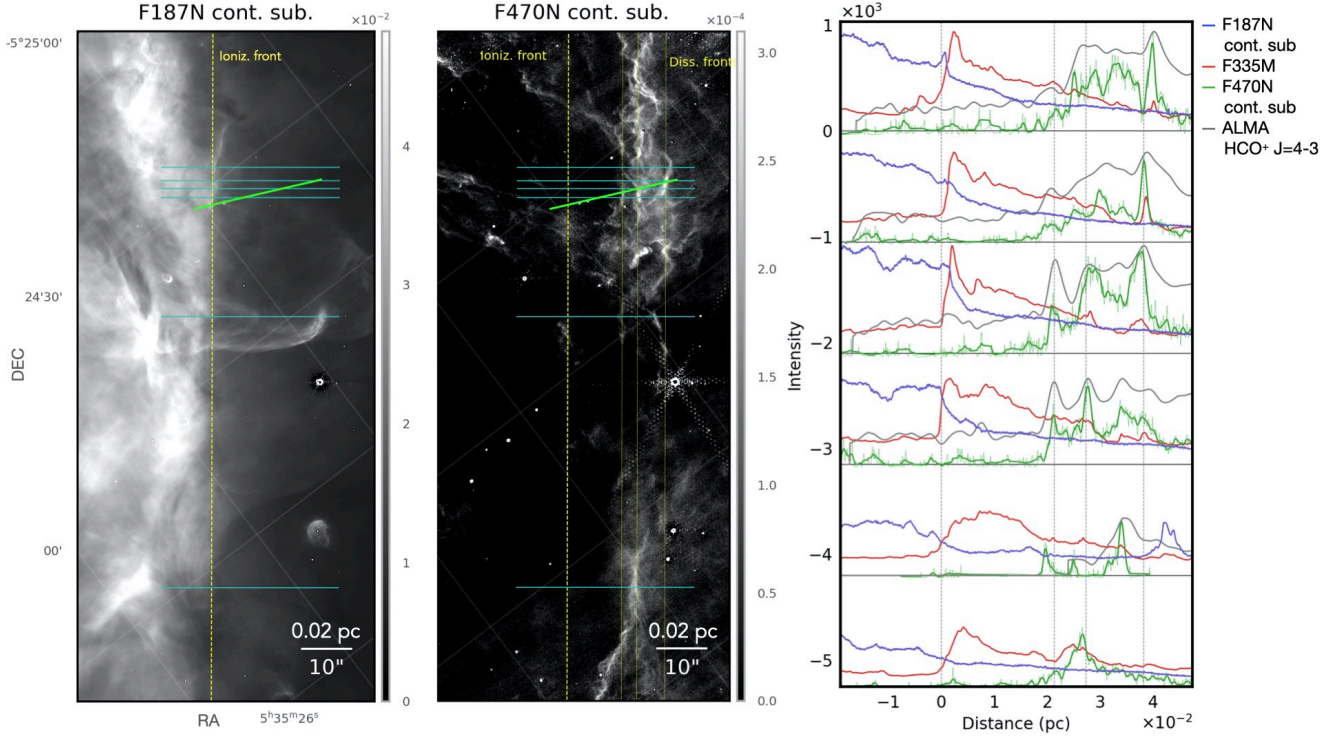
Fig. 9. Spatial distribution of the ionized and excited dense molecular gas. *Left*: maps in the F187N filter (Pa α line) and in the F470N filter continuum subtracted (H$_2$ 0–0 S(9) line). Same as Fig. 6 for the vertical and horizontal lines. Vertical dotted lines in the F470N filter continuum subtracted show the DFs position as determined in Sect. 5.2.1. Units are in erg cm^{-2} s^{-1} sr^{-1}. *Right*: Surface brightness profiles of the Pa α (in blue) and H$_2$ 0–0 S(9) line (in green) as a function of the distance from the IF. The profiles of the lines are normalized to the surface brightness profiles of the F335M filter (in red). The intensities have not been corrected for dust extinction. The ALMA HCO$^+$ $J = 4$–3 line integrated intensity profile is shown in grey. The vertical dotted-dashed lines indicate the average position of the IF and the DFs, also indicated by yellow lines in the left panels.

Additional evidence for the terraced-field-like structure comes from the difference in visual extinction $A_{V\mathrm{Bar}}^{\mathrm{los}}$ along the line of sight (see Fig. 5 and Sect. 5.2.2; Peeters et al. 2023), as well as the comparison between NIR and millimeter data (Sect. 5.2.4), showing that $A_{V\mathrm{Bar}}^{\mathrm{los}}$ is higher for the DF1 than for the DF2 and the DF3 dissociation fronts. Furthermore, DF1 remains visible in the NIRCam filter F335M but is no longer discernible in the F210M filter (see Fig. 10). This last filter is most likely due to the dust scattered light. The fact of not seeing DF1 in F210M confirms that there is more material along the line of sight at the DF1 position.

An additional morphological point to highlight is the contrast between a relatively smooth and unstructured IF (see the Pa α line map in Fig. 9) and a complex, structured, folded DF surface as traced by the H$_2$ 0–0 S(9) line in Fig. 9). Moreover, the southwest part of the Bar which corresponds to the upper part of the map displayed in Fig. 9 is much more structured than the other regions of the Bar. In the northeast, a single main DF is observed. This could be related to previous ground-based observations of the molecular condensations deeper inside the PDR which showed that the northeast part of the Bar has a main condensation while the southwest part is fragmented into several components (e.g., Lis & Schilke 2003; Lee et al. 2013).

Physical origin of the terraced-field-like structure. These structures may result from pre-existing high density structures shaped by the high FUV field inducing a compression. The density contrasts increase due to compression. Another potential

explanation is that the region exposed to stellar winds and protostellar outflows make it especially turbulent. On larger spatial scales, SOFIA observations of C$^+$ reveal that stellar winds and protostellar outflows shape the molecular cloud and also inject mechanical energy (Pabst et al. 2020). Regularly spaced ridges that run parallel to the photo-dissociation front could also suggest that large-scale magnetic fields are dynamically-important (Mackey & Lim 2011) and raise the question if they could be associated with magnetic-driven density peaks. If the gas thermal pressure is very large then one needs strong magnetic fields for such an hypothesis to be dynamically relevant (e.g., for $P_{\mathrm{th}} \sim 2 \times 10^8$ K cm^{-3}, one needs 800 µG; Pellegrini et al. 2009; Goicoechea et al. 2016). SOFIA HAWC+ observations of the dust polarization toward the Bar reveal a magnetic field strength of $\sim$300 µG (Chuss et al. 2019; Guerra et al. 2021). However, high angular observations of the dust polarization are needed to confirm its relevance. Berné et al. (2010) observed similar ridge-like structures, coined the "Ripples", in the western part of the Orion Nebula, also at the interface between the molecular cloud and the HII region. They interpreted the formation of these structures as the result of the Kelvin-Helmholtz (KH) instability occurring due to gas shearing at the interface. Interestingly, the spatial extension of these structures is about 10 times larger ($\sim$0.1 pc) than that of the ridges observed in the Bar ($\sim$0.01 pc, Fig. 7). This can be explained by the larger density of the molecular gas in the Bar (close to 10^5 cm^{-3} at the DFs, Table 2) as compared to the density in the Ripples (closer to 10^4 cm^{-3}). The fact that the ridges in the Bar appear less well-aligned than in the
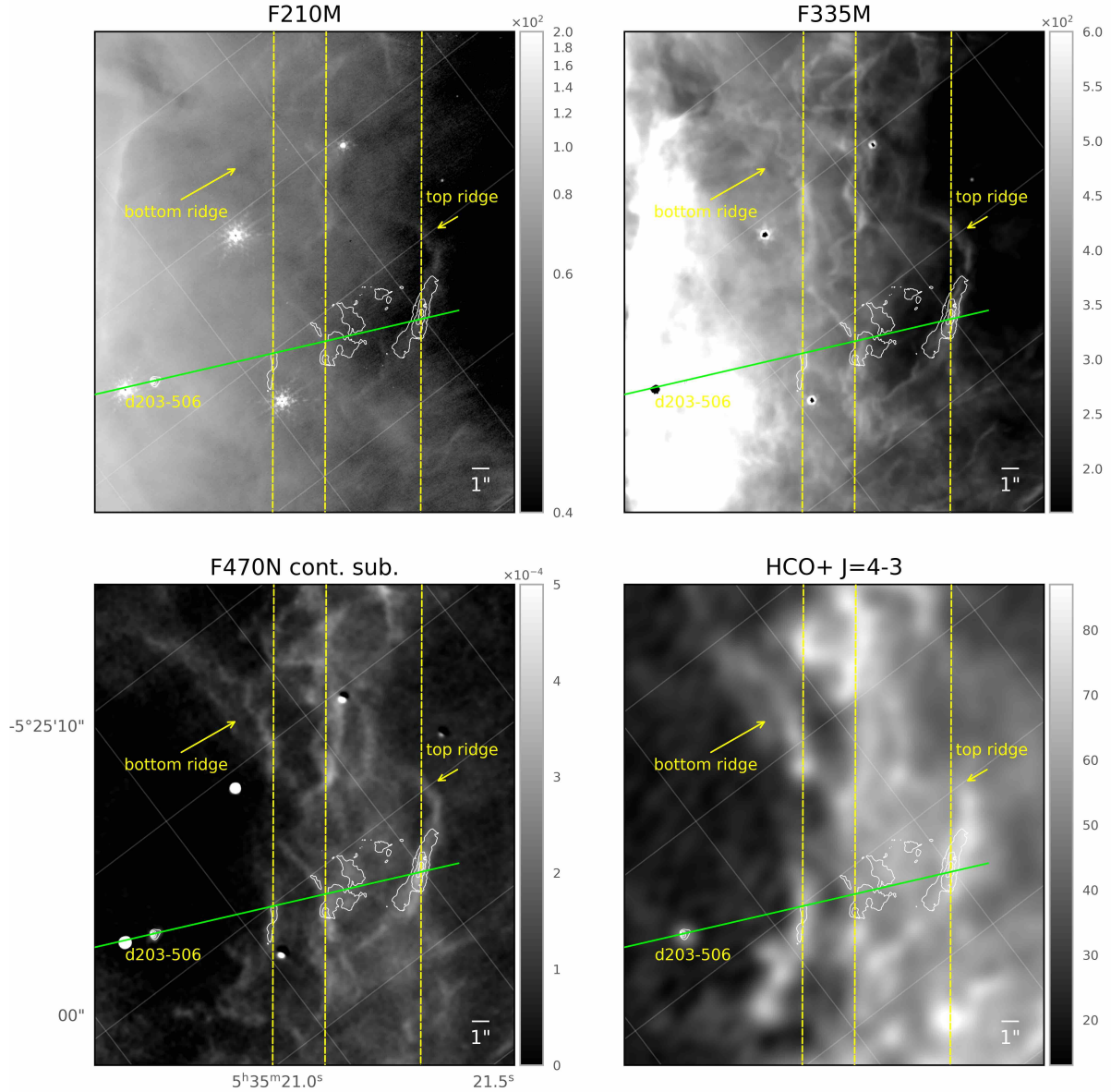
Fig. 10. Zoom into the Bar covered in part by the NIRSpec observations. From upper left to bottom right: NIRCam maps in the F210M filter (tracing dust scattered light), F335M (emission from the 3.3–3.4μm aromatic and aliphatic CH stretching modes), continuum subtracted F470N (tracing H$_2$ 0–0 S(9)) and the ALMA HCO$^+$ $J = 4$–3 map. Contours of the NIRSpec map in the 0–0 S(9) line with levels equal to 1.5, 2.3, 3.1, 3.9, 4.6 10^{-4} erg s^{-1} cm^{-2} sr^{-1} are shown in white. The vertical dotted yellow lines indicate the average position of the main DFs. The inclined line in green gives the position of the cut in the NIRSpec field shown in Fig. 11.

Ripples also suggests that the gas is in a more turbulent phase, which could correspond to the decay of the KH instability (Berne & Matsumoto 2012).

5.2.2. Extinction attenuation of the H$_2$ NIR lines along the line of sight

The intensity variations in the different H$_2$ 1–0 S(1) at 2.12 μm emission peaks ranging from ~2 to ~10 × 10^{-4} erg s^{-1} cm^{-2} sr^{-1} (Fig. 11) may result from a combination of effects due to the local gas densities, geometry (length of the edge-on portion along the line of sight) and dust extinction along the line of sight. For the H$_2$ emission in the PDR, extinction along the line of sight due to the dust in the Bar itself between the ionized gas and the region of excited H$_2$ may significantly attenuate the NIR emission. The extinction might be variable depending on the sightline

and the density of the region crossed. From the radio and NIR H$_2$ line maps, Walmsley et al. (2000) suggests, in fact, that extinction can vary rapidly as a function of position in the Bar. Precise spatial estimates of the internal PDR extinction are thus required. This is possible with the high angular resolution near-IR line maps we obtained with JWST that constraint in detail how dust extinction affect the apparent morphology of the NIR H$_2$ line emission and how the matter is distributed along the line of sight.

Extinctions towards the edge-on DFs. An effective way to measure extinction is comparing the observed-to-theoretical H$_2$ ro-vibrational line flux ratios from pairs of lines arising from the same upper level that are separated in wavelength. The dust absorption cross-section rapidly drops with increasing wavelength. Although NIRCam maps can give an overall view of
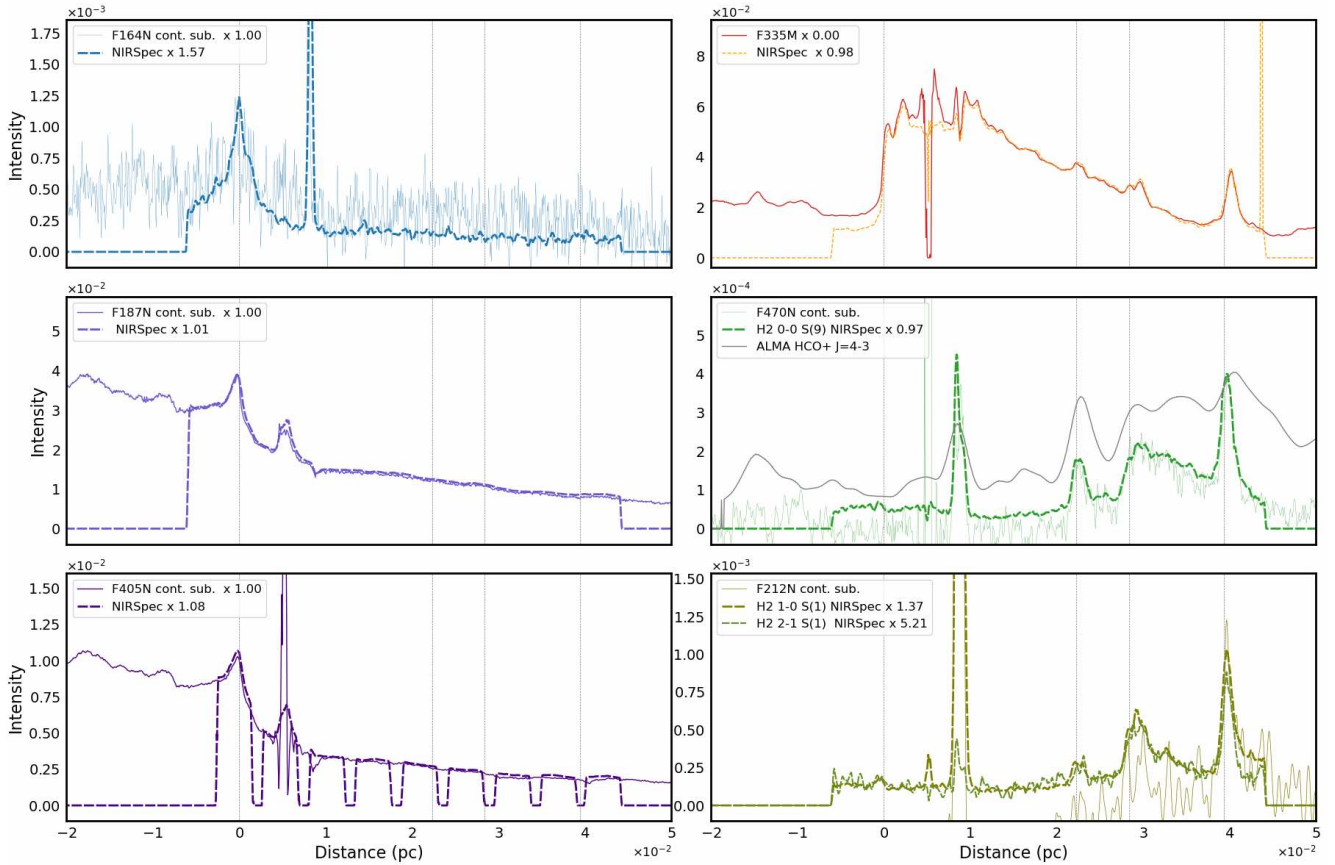
Fig. 11. Intensity profiles shown as a function of the distance from IF along the NIRSpec cut (Fig. 10.) comparing NIRCam imaging data in selected filters (continuum substracted) and NIRSpec line intensities. Units are in erg cm^{-2} s^{-1} sr^{-1}. The emission line intensities are continuum subtracted. The vertical dotted lines indicate the average position of the IF and the main DFs. In comparison to the cuts perpendicular to the Bar, it can be noted that the positions of the DFs are slightly shifted by approximately 0.0016 pc due to the inclination of the NIRSpec cut. The intensity profiles of the lines observed with NIRSpec have been scaled by the factors indicated in the legends. The intensities have not been corrected for dust extinction.

the extinction across the entire front, we cannot use the maps in the F212N filter (centered on H$_2$ 1–0 S(1) line at 2.12 μm) and the F323N filter (centered on 1–0 O(5) line at 3.23 μm with same upper level) since this last filter is dominated by aromatic band emission (see Sect. 3.3). NIRSpec observations from Peeters et al. (2023) where line intensity can be measured without being contaminated by bands were used. The extinction map and profile derived along the line of sight, $A_{V\mathrm{Bar}}^{\mathrm{los}}$, in the NIRSpec field is shown in Peeters et al. (2023). $A_{V\mathrm{Bar}}^{\mathrm{los}}$ is found equal to 10–12 on DF1 and decreases to 5–3 on DF2 and DF3. This shows that DF1 is farther along the line of sight and is in agreement with the stepwise structure (see Fig. 5) with the column density along the line of sight increasing for the first DFs which are more distant from the observer (but closer in projected distance from the IF).

NIR H$_2$ line intensity variations due to extinction. Due to extinction effects along the line of sight, the H$_2$ 1–0 S(1) line at 2.12 μm is significantly attenuated compared to the 0–0 S(9) line at 4.69 μm at the DF1 (by about 50%, see the line profiles shown in Fig. 11 towards the NIRSpec cut). Comparing the NIRCam H$_2$ 0–0 S(9) 4.69 μm and Keck 1–0 S(1) 2.12 μm line maps, one can see that the latter is systematically weaker all along the DF1 on the entire southern part of the Bar (Fig. B.5). However, the extinction alone cannot account for the intensity variations observed between the DFs. The H$_2$ at 4.69 μm, which is little

attenuated by the dust extinction effects (decrease less than 10–20% for $A_V = 10$), is in fact twice as high at DF3 than at DF1. This intensity variation must result from geometrical or density effects.

5.2.3. Highly rotationally and ro-vibrationally excited H$_2$ lines profiles

Here, we compare the surface brightness profiles of several rotationally and ro-vibrationally excited H$_2$ lines, [FeII] 1.664 μm, Pa and Br α lines and AIBs measured with NIRCam and NIRSpec (see Fig. 11). A very good agreement between NIRCam and NIRSpec is found in terms of line distribution and intensity.

The spatial emission profiles of H$_2$ lines agree in remarkable detail. The H$_2$ 1–0 S(1) ($v = 1$, $J = 3$, E_u=6951 K), 0–0 S(9) ($v = 0$, $J = 11$, E_u=10 261 K), 2–1 S(1) ($v = 2$, $J = 3$, E_u=12 550 K) line emission show the same spatial behavior with a strong increase at the edge-on DF1, DF2 and DF3. The emission peaks of the different H$_2$ lines at the edge-on DFs spatially coincide at the spatial resolution of our observations (Fig. 11). The H$_2$ line profiles follow each other very well for $d_{\mathrm{PDR}} > 0.01$ pc, with small line ratio variations. Along the NIRSpec cut, the most significant line ratio variation with a strong excess of the 1–0 S(1) line is observed on the irradiated disk d203–506. This

is due to a density increase (Berné et al. 2023). For dense highly irradiated conditions, collisional population of the $v = 1$, $J = 3$ level becomes competitive, and the 1–0 S(1)/2–1 S(1) lines ratio is thus expected to increase from a pure radiative cascade value (~2) to a collisional excitation value (of the order of 10). In the Bar, the 1–0 S(1)/2–1 S(1) line ratio is on the order of ~5. This ratio varies little between the different edge-on DFs. Gas density of the H_2 emission zone must remain comparable along the folded DFs surface.

Background H_2 emission toward the ionized and atomic region. Along the profiles, the H_2 emission seen in projection in front of the Bar and in the atomic region mostly comes from the surface of the OMC-1 in the background, not from the Bar itself. This is demonstrated by several points as explained below. First, NIRCam and NIRSpec emission line profiles are flat and at the same level of intensity in the ionized and atomic regions. Second, the NIRSpec H_2 excitation diagrams are very similar in the ionized and atomic region (Peeters et al. 2023). The emission in the atomic region itself is predicted by PDR models to be very weak. For example, for an isobaric model (with the Meudon PDR code, Le Petit et al. 2006) with $P = 5 \times 10^7$–10^8 K cm^{-3} (corresponding to $n \sim 5 \times 10^4$ cm^{-3} in the atomic region and $n \sim 10^5$ cm^{-3} in the zone where the H_2 abundance increases sharply and high-J and v H_2 lines emit), the predicted H_2 0–0 S(9) line emissivity is on average 100–50 times lower in the atomic region than at the H_2 peak.

Density in the H_2 emission zone compared with that estimated in the atomic region. By fitting the intensities of a hundred H_2 lines measured with NIRSpec to the grid of Meudon PDR models Peeters et al. (2023) found that densities are about $n_H = (3.5$–$10) \times 10^4$ cm^{-3} in the H_2 emission zone in the Bar, and similar towards the face-on background OMC-1 PDR. This density is of similar magnitude with density estimates from AIB emission profiles in Sect. 5.1.2. Density must be roughly constant from the PDR edge (where AIB emission peak) to the beginning of the ro-vibrationally excited H_2 emission layer where the density and H_2 abundance starts to increase sharply. This is consistent with the average atomic PDR density derived from the observed location of the H^0/H_2 transition. The H^0/H_2 is predicted by PDR models to be displaced inward from the IF by $A_V \sim 1$ for the Bar physical conditions (i.e., high G_0/n_H regime). Using $A_V/N_H = 3.5 \times 10^{-22}$ mag cm^{-2}, this translates into an average atomic PDR density of 1 mag $/(3.5 \times 10^{-22}$ mag cm$^{-2})/(d_{\text{IF–DF}}) = 4.6 \times 10^4 \times (0.02$ pc$/d_{\text{IF–DF}})$ cm^{-3} with $d_{\text{IF–DF}}$ the distance between IF and DF. By taking the values of $d_{\text{IF–DF}}$ given in Sect. 5.2.1, we obtain densities comparable to those derived at the PDR edge from AIB emission.

5.2.4. Spatial distribution between the H_2 and HCO$^+$ $J = 4$–3 emission

Common substructures in the H_2 and HCO$^+$ $J = 4$–3 lines. Figs. 10 and B.5 compare the H_2 maps to HCO$^+$ $J = 4$–3 line map across the same field of view. Most of the substructures are common to both maps and show a very similar distribution. The overall spatial coincidence between the H_2 and HCO$^+$ line emission shows that they both come from the edge of dense structures and that they are chemically linked. Because of its high dipole moment, and thus critical density for collisional excitation (a few 10^6 cm^{-3} for optically thin emission), the HCO$^+$

$J = 4$–3 rotational line is a good indicator of dense molecular gas. Thus, some of the densest portions of the Bar lie very near the DFs. Detection of both bright HCO$^+$ and CO emission by ALMA towards the H_2 vibrational emission layers suggests that the C$^+$/CO transition nearly coincides with the H^0/H_2 transition (in agreement with Goicoechea et al. 2016). In dense PDRs, the reaction between vibrationally excited H_2 molecules and C$^+$ ions becomes exothermic and leads to the formation of CH$^+$. Fast exothermic reactions with H_2 subsequently lead to the formation of CH$_3^+$. This key hydrocarbon ion reacts with abundant oxygen atoms and enhances the HCO$^+$ abundance in the H_2 emitting PDR layers (Goicoechea et al. 2016). We estimated that the average offset between H_2 and HCO$^+$ is less than 1″, about ~0.6″ (or 0.0012 pc). This is close to the distance between the H^0/H_2 and C$^+$/C/CO transition as predicted by high-pressure isobaric stationary PDR models (Joblin et al. 2018).

Bright emission from the surface of the molecular condensations. The small H_2 and HCO$^+$ $J = 4$–3 structures localized at the DF are in general shifted by a about ~10−20″ relative to the center of the bigger (5″−10″) molecular condensations seen more inside the molecular cloud (Young Owl et al. 2000; Lis & Schilke 2003). However, some bright H_2 fronts detected in the northwest end of the Bar (sixth cut in Fig. 9) and between the center and the southwest end of the Bar (zone C in Figs. 3 and 4) correspond to the irradiated superficial layers of the bright cold cores detected in CS $J = 2$–1 (cores denoted 3 in the north and 1 in the center-south respectively in Lee et al. 2013). These starless cores are fragmented into 3–5 components, and their fragments are embedded in larger filamentary structures. Some of the clumps are likely collapsing to form a low-mass star (Lis & Schilke 2003). JWST observations could therefore provide very strong constraints on the external boundary conditions (n_H, T_g) of these molecular condensations.

Substructures located further along the line of sight. The HCO$^+$ $J = 4$–3 substructures found at DF1 have emission velocity ($v_{\text{LSR}} = 8$–9 km s^{-1}) more consistent with emission from the background OMC-1 than from the Bar ($v_{\text{LSR}} = 10.5$ km s^{-1}). These structures may thus be located further along the line of sight. This is consistent with the stepwise structure (Fig. 5) and estimates of extinction from H_2 lines (see Sect. 5.2.2). Towards the HCO$^+$ $J = 4$–3 and H_2 common substructures, those found at DF1 are accordingly faintly visible in the H_2 ro-vibrational emission at 2.12 μm (Figs. 11 and B.5), since they are affected by extinction along the line of sight.

6. Photoevaporating protoplanetary disks

In this section, we describe the photoevaporating proto-planetary disks observed in the whole NIRCam fields. The NIRCam images of the Orion Nebula show, in several passbands, numerous spatially resolved externally illuminated protoplanetary disks surrounding young stars, also known as proplyds (O'Dell et al. 1993). They are mostly found in the M42 region, clustering around the Trapezium stars and θ^2 Ori A, south of the Bar. A couple of proplyds were also identified in M43, located nearby NU Ori (HD 37061), the B0.5V star creating the almost spherical HII region of M43 (see Appendix C). Proplyds inside the HII region typically show bright heads of ionized gas (ionization front) and tails pointing directly away from the brightest OB stars. The proplyd family (as defined in O'Dell et al. 1993)

also include YSO's seen in silhouette against the background HII region. The disks appear as dark ellipses on top of a bright nebula background and are called pure silhouettes.

The *Hubble* Space Telescope was the first observatory to spatially resolve proplyd anatomy and show detailed structure of each one of its components: ionized cocoon, embedded photo-evaporating disk and jets/outflows. Nearly 200 proplyds in the Orion Nebula were discovered in HST images, mostly using narrow-band filters centered on the Hα λ6563 and forbidden lines of [NII] λ6583, [O I] λ6300, [O III] λ5007, and [S II] λ6717 + 6731 lines (Prosser et al. 1994; O'Dell & Wen 1994; O'Dell & Wong 1996; McCaughrean & O'Dell 1996; Bally et al. 1998, 2000; O'Dell 2001a; Smith et al. 2005). The most complete catalog of proplyds found in M42 and M43 is presented in Ricci et al. (2008). The atlas is based on HST/ACS/WFC observations obtained under the Treasury Program on the Orion Nebula (PI: M. Robberto, GO 10249) using B, V, I, z passbands and the Hα narrow-band filter. They compile proplyds from previous studies and find new ones, including disks identified by their bipolar nebulae and jets, if closer than 1″ to the stellar source. They exclude HH objects, bow-shocks and elongated jets, but include candidate background galaxies or filaments. The catalog lists 178 bright proplyds with tails, 28 silhouettes, 8 bipolar nebulae and 5 jets, on a total of 219 sources.

In order to identify known proplyds, and possibly find new ones, we cross-matched the sources in the NIRCam images with the Ricci et al. (2008) catalog. We used the F187N narrow-band filter, centered on the Paα emission line, because proplyd ionization fronts and tails are better traced in hydrogen recombination lines. In addition, the JWST diffraction limit at this wavelength (1.87 μm) is nearly the same as HST at 0.656 μm or Hα, that is ~0.07″, allowing for a direct comparison of proplyd morphology in the optical and in the near-IR. Narrow-band filters centered on emission lines are always preferred to observe proplyd structure because they cancel most of the continuum from the central star. Nevertheless, and due to the extreme sensitivity of JWST/NIRCam instrument, most proplyds remain unseen, obscured by the bright "snow-flake" shape PSF of the JWST, even in the narrow-band filters. The best targets are proplyds with nearly edge-on disks that still remain optically thick at near-IR wavelengths and hence are able to cover the young star. A few proplyds show wind-wind arcs and a couple show collimated jets. A detailed analysis of a few of these objects will be the subject of another article.

6.1. M42 region

The NIRCam images were divided into module A, covering the North of the Dark Bay and corresponding to the northeast region of the Trapezium stars, and module B, covering the southeast region of the Trapezium stars, the Bar and θ^2 Ori A. The M42 south field of view includes 62 known proplyds but only 34 of these were identified as having extended proplyd structure in the F187N image: 29 bright proplyds and 5 pure silhouettes. They are shown in Fig. 12. The giant proplyd 244–440 is shown in Fig. 13 due to its much larger size. No new proplyds were found.

The field of view north of the Dark Bay includes 16 sources from the Ricci et al. (2008) catalog, of which 12 are bright proplyds, 3 are pure silhouettes, and one is a bipolar reflection nebula. Only 7 of the 12 proplyds show extended structure, and only one silhouette of the 3 is visible in the F187N image because it is an edge-on disk. The other proplyds are simply point-like sources. The proplyd 215–106 shows a bright spot in the PSF

that can be associated to a jet or a fainter smaller companion, requiring further analysis. The reflection bipolar nebula 208–122 does not appear in the F187N image but it reveals instead a close binary. The reflection polar nebulae and a dark disk are clearly seen in the F164N image centered at the [FeII] line at 1.64 μm. These objects are shown in Fig. C.12. We also find 3 new proplyd candidates (shown in Fig. C.13), very faint and small, and named them 171–212, 180–218 and 234–104, following O'Dell & Wen (1994) coordinate-based naming convention. 171–212 is a small proplyd in the north with a faint tail. 234–104 shows a faint ionized cusp in Paα but not a tail. It lies in the northeast, at a distance greater than 140″ from the Trapezium. Both objects face the Trapezium stars. 180–218 lies along what seems to be a faint ionized filament or shock front. A round cusp surrounding a star is seen in Paα and Brα hydrogen recombination lines, but not in other line tracers. It also shows no tail. The cusp can be the ionization front or a bow-shock caused by wind-wind interaction, requiring further analysis. The 3 objects are proplyds in nature because they fill in the proplyd criteria which are a disk and/or envelope that is being photoevaporated by external UV radiation. They show an ionization front and sometimes a tail and a bow-shock and have already a YSO forming inside. They differ from Evaporating Gaseous Globules (EGGs) which do not have yet a star forming and are just condensations of dense gas experiencing external photoevaporation. The 3 objects are not part of the 2MASS catalog of point sources and hence they must be very-low mass YSOs.

6.2. M43 region

The NIRCam images obtained in the parallel mode were divided into module A, covering M43, and module B, covering a region in the north of M42. The NIRCam images of M43 include 4 proplyds from Ricci et al. (2008) catalog but only one of them shows extended structure. That is proplyd 332–1605 pointing directly to the ionizing star NU Ori, at 27″ to the west, and showing a long tail, with a head-to-tail extension of 11.6″ or 4600 au at 414 pc, measured in the F187N NIRCam image. That is nearly 10 times larger than the proplyd HST10 which makes it a giant proplyd candidate. This proplyd was first discovered in HST/WFPC2 parallel images (PI: Rubin, GO 6065) analyzed by O'Dell (2001a) as having a faint ionization front visible in Hα and [SII] images but not in [OIII], and no tail. This object was also imaged with HST/ACS in Hα by Ricci et al. (2008) who confirmed its tailless structure. The fact that we see a long tail in Paα and not in Hα is consistent with the low ionizing power of the star NU Ori (B0.5V) when compared to the Trapezium stars (O7V for θ^1 Ori C) or θ^2 Ori A (O9.5V). A new proplyd candidate is found in the F187N image with a prominent jet rendered visible by a chain of knots or HH objects. The ionization front and the knots are also visible in the HST/ACS image in Hα, but not the central star. The powerful jet and the fact that it is not visible in the optical means this object must be very young, still embedded in its circumstellar envelope of gas and dust and experiencing high accretion, that is, it is still a protostar. This object is part of the 2MASS catalog of point sources. We named it 269–1713 following O'Dell & Wen (1994) coordinate-based naming convention. The new proplyd is located at 97″ to the southwest of the ionizing star, NU Ori. Figures C.14 and C.15 show respectively the giant proplyd 332–1605 and the new proplyd candidate 269–1713 in NIRCam Paα vs. HST/ACS Hα (PI: J.Bally, GO 9825) images. In the NIRCam images of M43 and M42 north we find numerous
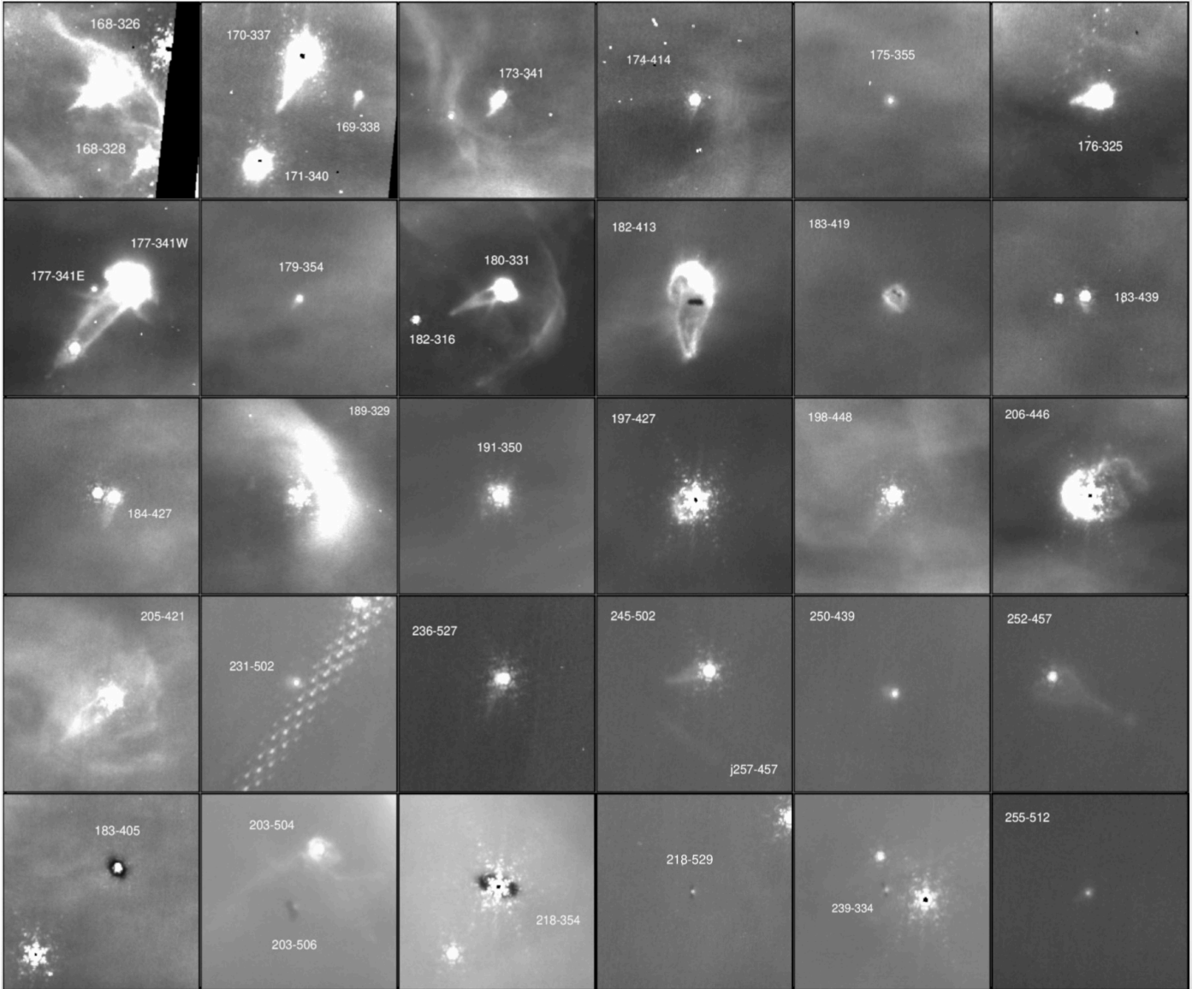
Fig. 12. Zoom on the 29 bright proplyds and 5 silhouettes showing extended structure in the F187N image of M42 covering the southeast region of the Trapezium and the Bar (detector B). The tiles are 5″ × 5″ with north up and east to the left. Some images suffer from instrumental effects such as the diffraction pattern of bright stars and uncorrected cosmic ray events, affecting particularly the edge of the images because of lack of redundancy.

extended, elliptical and diffuse objects, sometimes with spiral arms. These are background galaxies.

7. Conclusions

The JWST/NIRCam and MIRI imaging observations of the Orion Nebula allow us to probe the global fundamental structure and small-scale structures of an interstellar cloud strongly illuminated by UV radiation. We have access to the multiple scales of the nebula with resolution of 0.1 to 1″ from 2 to 25 μm, equivalent to $\sim 2 \times 10^{-4}$ to 2×10^{-3} pc or 40 to 400 au at 414 pc, over a field of view of 150″ and 42″, equivalent to ~0.3 and 0.08 pc (at the Orion distance of 414 pc) for NIRCAM and MIRI images centered on the Bar. Our main results can be summarized as follows.

- One of the most striking features observed in all our NIR-CAM and MIRI images is that the molecular cloud borders appear structured at small scales. Numerous patterns are observed, such as ridges, waves and globules. This highlights a very intricate irradiated cloud surface (most likely turbulent) and sub-dense structures at such small scales that they were inaccessible to previous IR observations. Several bright emission features associated with the highly irradiated surroundings of dense molecular condensations, embedded young star and photoevaporated protoplanetary disks are detected in the extended PDR layers;

- The observations spatially resolve the transition from the ionization front, the dissociation front to the molecular cloud of the prototypical highly irradiated extended dense Orion Bar PDR. This allows us to study the PDR along all its fronts and to spatially resolve the FUV radiation penetration scales inside the molecular cloud. A progressive structure is evident in agreement with previous studies. However, instead of a smooth PDR transition, JWST unambiguously reveals a
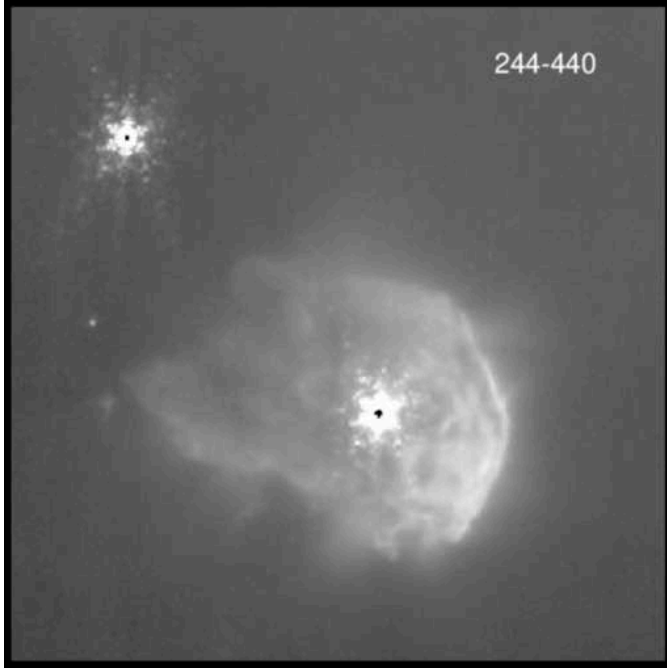
Fig. 13. Giant proplyd 244–440 located southeast of the Bar and illuminated by both stars, θ^1 Ori C and θ^2 Ori A. The image is $10'' \times 10''$ in the F187N NIRCam filter, with north up and east to the left.

highly sculpted interface with very sharp edges and multiple ridges;

– The spatial distribution of the AIB emission reveal a very sharp illuminated edge at the IF (on scales of $1''$ or 0.002 pc) with a strong density rise in the neutral zone. This is expected due to the sharp decrease in gas temperature at the ionization front if the thermal pressures in the ionized and neutral region are of similar magnitude. The density we derived in the atomic region ($n_{\rm H} \sim (5$–$10) \times 10^4$ cm^{-3}) is much higher (factor 10–20) than the electron density previously derived at the IF. Behind the sharp PDR edge, an extensive warm layer of neutral material, essentially atomic with strong emission from the AIBs, is observed up to the H^0/H_2 dissociation front at 10–$20''$ or 0.02–0.04 pc from the IF;

– In contrast to the IF, a very complex, structured and folded H^0/H_2 dissociation front surface is traced by the H_2 lines. This is particularly apparent in the southwestern part of the Bar. A terraced-field-like structure with several steps seen from above can explain the succession of H_2 ridges across the Bar. In that geometry, each observed H_2 emission ridge corresponds to a portion of the DF seen edge-on;

– The line spatial profiles of the highly rotationally and rovibrationally excited H_2 agree in remarkable detail. Physical conditions must be comparable along the folded DFs surface. Very thin and bright H_2 emission layers ($\sim10^{-3}$ pc) are spatially resolved at the irradiated surface of the dense molecular regions. The highly excited H_2 emission arises from the very thin zone where the gas density and H_2 abundance starts to increase sharply;

– A remarkable agreement in the spatial distribution between the rotationaly and rovibrationaly excited H_2 and ALMA HCO^+ $J = 4$–3 emission maps is observed. This indicates that they both come from the edge of dense structures and

that they are chemically linked. Some of the densest portions of the Bar lie very near the DFs. This is in agreement with previous analysis of ALMA and *Herschel* observations. However, the small structures were unresolved in most tracers until now. JWST observations provide very strong constraints on the external boundary conditions of the dense molecular condensations;

– In M42, several outflows interacting with the ambient ionized gas of the nebula or the molecular gas are detected. Crenellated structures and various arches which are most likely bow-shocks are observed. Regions exposed to stellar winds and protostellar outflows might be especially turbulent;

– Numerous proplyds are identified in the NIRCam images of M42 and M43. Nevertheless, many remain unseen, obscured by the bright snow-flake PSF of the very sensitive JWST. The best observed targets are proplyds with nearly edge-on disks that remain optically thick at near-IR wavelengths and thus are able to cover the young star. For these proplyds, the NIRCam instrument offers a unique opportunity to study proplyd morphology in the near-IR with a spatial resolution comparable to the HST in the optical. We find 4 new proplyds identified in the F187N images, 3 located at the northeast from the Trapezium stars and one in the M43 region. They were named 171–212, 180–218, 234–104 and 269–1713, following O'Dell & Wen (1994) coordinate-based naming convention.

The JWST ERS program on the Orion Bar PDR (Berné et al. 2022b) gives access to IFU spectroscopy with NIRSpec and MIRI which will be published in other articles. IFU spectroscopy provides insight into the local gas physical conditions (temperature, density, and pressure), the dust properties and the chemical composition of the warm, very structured irradiated medium. It will be possible to probe the dust properties and physical conditions in the dense substructures detected with NIRCam and MIRI images described in this article. To determine the pressure and density variations at the PDR edge, future detailed spatial studies of both the H_2 pure rotational and rovibrational lines will be carried out (Peeters et al. 2023), van de Putte et al. (2024). These constraints on the physical conditions may allow us to better understand the dynamical effects in PDRs, such as compression waves and photo-evaporative flows.

References

Abel, N. P., Ferland, G. J., & O'Dell, C. R. 2019, ApJ, 881, 130

Allers, K. N., Jaffe, D. T., Lacy, J. H., Draine, B. T., & Richter, M. J. 2005, ApJ, 630, 368

Arab, H., Abergel, A., Habart, E., et al. 2012, A&A, 541, A19

Axford, W. I. 1961, Philos. Trans. Roy. Soc. Lond. Ser. A, 253, 301

Bakes, E. L. O., & Tielens, A. G. G. M. 1994, ApJ, 427, 822

Bally, J., Sutherland, R. S., Devine, D., & Johnstone, D. 1998, AJ, 116, 293

Bally, J., O'Dell, C. R., & McCaughrean, M. J. 2000, AJ, 119, 2919

Bernard-Salas, J., & Tielens, A. G. G. M. 2005, A&A, 431, 523

Bernard-Salas, J., Habart, E., Arab, H., et al. 2012, A&A, 538, A37

Berne, O., & Matsumoto, Y. 2012, ApJ, 761, L4

Berné, O., Marcelino, N., & Cernicharo, J. 2010, Nature, 466, 947

Berné, O., Foschino, S., Jalabert, F., & Joblin, C. 2022a, A&A, 667, A159

Berné, O., Habart, É., Peeters, E., et al. 2022b, PASP, 134, 054301

Berné, O., Habart, É., & Peeters, E. 2023, Science, 383, 988

Binder, B. A., & Povich, M. S. 2018, ApJ, 864, 136

Black, J. H., & van Dishoeck, E. F. 1987, ApJ, 322, 412

Blagrave, K. P. M., Martin, P. G., Rubin, R. H., et al. 2007, ApJ, 655, 299

Cardelli, J. A., Clayton, G. C., & Mathis, J. S. 1989, ApJ, 345, 245

Cesarsky, D. A. 1982, A&A, 113, L7

Champion, J., Berné, O., Vicente, S., et al. 2017, A&A, 604, A69

Chown, R., Okada, Y., & Peeters, E. 2023, A&A, 685, A75 (Paper IV)

Chuss, D. T., Andersson, B. G., Bally, J., et al. 2019, ApJ, 872, 187

Compiègne, M., Verstraete, L., Jones, A., et al. 2011, A&A, 525, A103

Cuadrado, S., Salas, P., Goicoechea, J. R., et al. 2019, A&A, 625, A3

Draine, B. T. 2011, Physics of the Interstellar and Intergalactic Medium, (Princeton, NJ, USA: Princeton Univ. Press)

Elliott, K. H., & Meaburn, J. 1974, Ap&SS, 28, 351

Elmegreen, B. G. 2011, in EAS Publications Series, 51, 45

Elyajouri, M., Ysard, N., Abergel, A., et al. 2024, A&A, 685, A76 (Paper V)

Galliano, F., Madden, S. C., Tielens, A. G. G. M., Peeters, E., & Jones, A. P. 2008, ApJ, 679, 310

García-Díaz, M. T. & Henney, W. J. 2007, AJ, 133, 952

Goicoechea, J. R., Teyssier, D., Etxaluze, M., et al. 2015, ApJ, 812, 75

Goicoechea, J. R., Pety, J., Cuadrado, S., et al. 2016, Nature, 537, 207

Goicoechea, J. R., Cuadrado, S., Pety, J., et al. 2017, A&A, 601, A9

Goicoechea, J. R., Pabst, C. H. M., Kabanovic, S., et al. 2020, A&A, 639, A1

Gordon, K. D., Bohlin, R., Sloan, G. C., et al. 2022, AJ, 163, 267

Gorti, U., & Hollenbach, D. 2002, ApJ, 573, 215

Großschedl, J. E., Alves, J., Meingast, S., et al. 2018, A&A, 619, A106

Güdel, M., Briggs, K. R., Montmerle, T., et al. 2008, Science, 319, 309

Guerra, J. A., Chuss, D. T., Dowell, C. D., et al. 2021, ApJ, 908, 98

Habart, E., Boulanger, F., Verstraete, L., et al. 2003, A&A, 397, 623

Habart, E., Walmsley, M., Verstraete, L., et al. 2005, Space Sci. Rev., 119, 71

Habart, E., Abergel, A., Boulanger, F., et al. 2011, A&A, 527, A122

Habart, E., Le Gal, R., Alvarez, C., et al. 2023, A&A, 673, A149

Habing, H. J. 1968, Bull. Astron. Inst. Netherlands, 19, 421

Henney, W. J. 2021, MNRAS, 502, 4597

Hogerheijde, M. R., Jansen, D. J., & van Dishoeck, E. F. 1995, A&A, 294, 792

Hollenbach, D. J., & Tielens, A. G. G. M. 1997, ARA&A, 35, 179

Hollenbach, D. J., & Tielens, A. G. G. M. 1999, Rev. Mod. Phys., 71, 173

Hopkins, P. F., Kereš, D., Oñorbe, J., et al. 2014, MNRAS, 445, 581

Jansen, D. J., Spaans, M., Hogerheijde, M. R., & van Dishoeck, E. F. 1995, A&A, 303, 541

Joblin, C., Tielens, A. G. G. M., Geballe, T. R., & Wooden, D. H. 1996, ApJ, 460, L119

Joblin, C., Bron, E., Pinto, C., et al. 2018, A&A, 615, A129

Jones, A. P., Köhler, M., Ysard, N., Bocchio, M., & Verstraete, L. 2017, A&A, 602, A46

Kahn, F. D. 1954, Bull. Astron. Inst. Netherlands, 12, 187

Kaplan, K. F., Dinerstein, H. L., Kim, H., & Jaffe, D. T. 2021, ApJ, 919, 27

Kavak, Ü., Bally, J., Goicoechea, J. R., et al. 2022a, A&A, 663, A117

Kavak, Ü., Goicoechea, J. R., Pabst, C. H. M., et al. 2022b, A&A, 660, A109

Knight, C., Peeters, E., Tielens, A. G. G. M., & Vacca, W. D. 2022, MNRAS, 509, 3523

Kounkel, M., Hartmann, L., Loinard, L., et al. 2017, ApJ, 834, 142

Kounkel, M., Covey, K., Suárez, G., et al. 2018, AJ, 156, 84

Kuhn, M. A., Hillenbrand, L. A., Sills, A., Feigelson, E. D., & Getman, K. V. 2019, ApJ, 870, 32

Lee, K., Looney, L. W., Schnee, S., & Li, Z.-Y. 2013, ApJ, 772, 100

Le Petit, F., Nehme, C., Le Bourlot, J., & Roueff, E. 2006, ApJS, 164, 506

Lis, D. C., & Schilke, P. 2003, ApJ, 597, L145

Mackey, J., & Lim, A. J. 2011, MNRAS, 412, 2079

Marconi, A., Testi, L., Natta, A., & Walmsley, C. M. 1998, A&A, 330, 696

Martín-Hernández, N. L., Peeters, E., Morisset, C., et al. 2002, A&A, 381, 606

Martini, P., Sellgren, K., & DePoy, D. L. 1999, ApJ, 526, 772

McCaughrean, M. J., & O'Dell, C. R. 1996, AJ, 111, 1977

Menten, K. M., Reid, M. J., Forbrich, J., & Brunthaler, A. 2007, A&A, 474, 515

Nony, T., Motte, F., Louvet, F., et al. 2020, A&A, 636, A38

Öberg, K. I., & Bergin, E. A. 2021, Phys. Rep., 893, 1

O'Dell, C. R. 2001a, AJ, 122, 2662

O'Dell, C. R. 2001b, ARA&A, 39, 99

O'Dell, C. R., & Wen, Z. 1994, ApJ, 436, 194

O'Dell, C. R., & Wong, K. 1996, AJ, 111, 846

O'Dell, C. R., & Yusef-Zadeh, F. 2000, AJ, 120, 382

O'Dell, C. R., Walter, D. K., & Dufour, R. J. 1992, ApJ, 399, L67

O'Dell, C. R., & Harris, J. A. 2010, AJ, 140, 985

O'Dell, C. R., & Henney, W. J. 2008, AJ, 136, 1566

O'Dell, C. R., Wen, Z., & Hu, X. 1993, ApJ, 410, 696

O'Dell, C. R., Hartigan, P., Bally, J., & Morse, J. A. 1997, AJ, 114, 2016

O'Dell, C. R., Henney, W. J., Abel, N. P., Ferland, G. J., & Arthur, S. J. 2009, AJ, 137, 367

O'Dell, C. R., Ferland, G. J., Henney, W. J., et al. 2015, AJ, 150, 108

O'Dell, C. R., Ferland, G. J., & Peimbert, M. 2017a, MNRAS, 464, 4835

O'Dell, C. R., Kollatschny, W., & Ferland, G. J. 2017b, ApJ, 837, 151

O'Dell, C. R., Abel, N. P., & Ferland, G. J. 2020, ApJ, 891, 46

O'Dell, C. R., Ferland, G. J., & Méndez-Delgado, J. E. 2023, AJ, 165, 21

Pabst, C. H. M. 2021, PhD thesis, University of Leiden, The Netherlands

Pabst, C., Higgins, R., Goicoechea, J. R., et al. 2019, Nature, 565, 618

Pabst, C. H. M., Goicoechea, J. R., Teyssier, D., et al. 2020, A&A, 639, A2

Pabst, C. H. M., Goicoechea, J. R., Hacar, A., et al. 2022, A&A, 658, A98

Parikka, A., Habart, E., Bernard-Salas, J., Köhler, M., & Abergel, A. 2018, A&A, 617, A77

Parmar, P. S., Lacy, J. H., & Achtermann, J. M. 1991, ApJ, 372, L25

Peeters, E., Allamandola, L. J., Bauschlicher, C. W., J., et al. 2004, ApJ, 604, 252

Peeters, E., Bauschlicher, Charles W., J., Allamandola, L. J., et al. 2017, ApJ, 836, 198

Peeters, E., Berné, O., & Habart, É. 2023, A&A, 685, A74 (Paper III)

Pellegrini, E. W., Baldwin, J. A., Ferland, G. J., Shaw, G., & Heathcote, S. 2009, ApJ, 693, 285

Plunkett, A. L., Arce, H. G., Corder, S. A., et al. 2013, ApJ, 774, 22

Prosser, C. F., Stauffer, J. R., Hartmann, L., et al. 1994, ApJ, 421, 517

Ricci, L., Robberto, M., & Soderblom, D. R. 2008, AJ, 136, 2136

Robberto, M., Gennaro, M., Ubeira Gabellini, M. G., et al. 2020, ApJ, 896, 79

Rubin, R. H., Simpson, J. P., Colgan, S. W. J., et al. 2007, MNRAS, 377, 1407

Rubin, R. H., Simpson, J. P., O'Dell, C. R., et al. 2011, MNRAS, 410, 1320

Salgado, F., Berné, O., Adams, J. D., et al. 2016, ApJ, 830, 118

Schirmer, T., Ysard, N., Habart, E., et al. 2022, A&A, 666, A49

Schneider, N., Röllig, M., Polehampton, E. T., et al. 2021, A&A, 653, A108

Sheffer, Y., Wolfire, M. G., Hollenbach, D. J., Kaufman, M. J., & Cordier, M. 2011, ApJ, 741, 45

Smith, N., Bally, J., Licht, D., & Walawender, J. 2005, AJ, 129, 382

Sota, A., Maíz Apellániz, J., Walborn, N. R., et al. 2011, ApJS, 193, 24

Spitzer, L. 2004, Physical Processes in the Interstellar Medium, Physics Textbook (Weinheim: Wiley), oCLC: 255567470

Stacey, G. J., Hailey-Dunsheath, S., Ferkinhoff, C., et al. 2010, ApJ, 724, 957

Tauber, J. A., Tielens, A. G. G. M., Meixner, M., & Goldsmith, P. F. 1994, ApJ, 422, 136

Tielens, A. G. G. M. 2008, ARA&A, 46, 289

Tielens, A. G. G. M., & Hollenbach, D. 1985a, ApJ, 291, 747

Tielens, A. G. G. M., & Hollenbach, D. 1985b, ApJ, 291, 722

Tielens, A. G. G. M., Meixner, M. M., van der Werf, P. P., et al. 1993, Science, 262, 86

Tielens, A., Meixner, M., Van der Werf, P., et al. 1993, Science, 262, 86

Vallini, L., Pallottini, A., Ferrara, A., et al. 2018, MNRAS, 473, 271

Van De Putte, D., Meshaka, R., Trahin, B., et al. 2024, A&A, accepted [arXiv:2404.03111] (Paper VIII)

van der Werf, P. P., Goss, W. M., & O'Dell, C. R. 2013, ApJ, 762, 101

Vicente, S., Berné, O., Tielens, A., et al. 2013, ApJ, 765, L38

Walmsley, C., Natta, A., Oliva, E., & Testi, L. 2000, A&A, 364, 301

Weilbacher, P. M., Monreal-Ibero, A., Kollatschny, W., et al. 2015, A&A, 582, A114

Weingartner, J. C., & Draine, B. T. 2001, ApJS, 134, 263

Wen, Z., & O'Dell, C. 1995, ApJ, 438, 784

Winter, A. J., & Haworth, T. J. 2022, Eur. Phys. J. Plus, 137, 1132

Wolfire, M. G., Hollenbach, D., McKee, C. F., Tielens, A., & Bakes, E. 1995, ApJ, 443, 152

Wolfire, M. G., McKee, C. F., Hollenbach, D., & Tielens, A. G. G. M. 2003, ApJ, 587, 278

Wolfire, M. G., Vallini, L., & Chevance, M. 2022, ARA&A, 60, 247

Young Owl, R. C., Meixner, M. M., Wolfire, M., Tielens, A. G. G. M., & Tauber, J. 2000, ApJ, 540, 886

[1] Institut d'Astrophysique Spatiale, Université Paris-Saclay, CNRS, Bâtiment121, 91405 Orsay Cedex, France
e-mail: pis@pdrs4all.org

[2] Department of Physics & Astronomy, The University of Western Ontario, London ON N6A 3K7, Canada

[3] Institute for Earth and Space Exploration, The University of Western Ontario, London ON N6A 3K7, Canada

[4] Carl Sagan Center, SETI Institute, 339 Bernardo Avenue, Suite 200, Mountain View, CA 94043, USA

[5] Institut de Recherche en Astrophysique et Planétologie, Université Toulouse III – Paul Sabatier, CNRS, CNES, 9 Av. du colonel Roche, 31028 Toulouse Cedex 04, France

[6] Space Telescope Science Institute, 3700 San Martin Drive, Baltimore, MD 21218, USA

[7] Department of Astronomy, University of Michigan, 1085 South University Avenue, Ann Arbor, MI 48109, USA

[8] Institut des Sciences Moléculaires d'Orsay, CNRS, Université Paris-Saclay, Bâtiment 520, 91405 Orsay Cedex, France

[9] Instituto de Astrofísica e Ciências do Espaço, Tapada da Ajuda, Edifício Leste, 2° Piso, 1349-018 Lisboa, Portugal

[10] ACRI-ST, Centre d'Études et de Recherche de Grasse (CERGA), 10 Av. Nicolas Copernic, 06130 Grasse, France

[11] INCLASS Common Laboratory, 10 Av. Nicolas Copernic, 06130 Grasse, France

[12] NASA Ames Research Center, MS 245-6, Moffett Field, CA 94035-1000, USA

[13] LERMA, Observatoire de Paris, PSL Research University, CNRS, Sorbonne Universités, 92190 Meudon, France

[14] Instituto de Física Fundamental (CSIC), Calle Serrano 121-123, 28006, Madrid, Spain

[15] UK Astronomy Technology Centre, Royal Observatory Edinburgh, Blackford Hill, Edinburgh EH9 3HJ, UK

[16] Observatorio Astronómico Nacional (OAN,IGN), Alfonso XII, 3, 28014 Madrid, Spain

[17] Sterrenkundig Observatorium, Universiteit Gent, Gent, Belgium

[18] Quantum Solid State Physics (QSP), Celestijnenlaan 200d – box 2414, 3001 Leuven, Belgium

[19] Institut de Planétologie et d'Astrophysique de Grenoble (IPAG), Université Grenoble Alpes, CNRS, 38000 Grenoble, France

[20] Institut de Radioastronomie Millimétrique (IRAM), 300 Rue de la Piscine, 38406 Saint-Martin d'Hères, France

[21] I. Physikalisches Institut der Universität zu Köln, Zülpicher Straße 77, 50937 Köln, Germany

[22] Department of Astronomy, Graduate School of Science, The University of Tokyo, 7-3-1 Bunkyo-ku, Tokyo 113-0033, Japan

[23] Department of Physics, Faculty of Science and Engineering, Meisei University, 2-1-1 Hodokubo, Hino, Tokyo 191-8506, Japan

[24] Johns Hopkins University, 3400 N. Charles Street, Baltimore, MD 21218, USA

[25] Physikalischer Verein – Gesellschaft für Bildung und Wissenschaft, Robert-Mayer-Straße 2, 60325 Frankfurt am Main, Germany

[26] Institut für Angewandte Physik. Goethe-Universität Frankfurt, Max-von-Laue-Str. 1, 60438 Frankfurt am Main, Germany

[27] Department of Space, Earth and Environment, Chalmers University of Technology, Onsala Space Observatory, S439 92 Onsala, Sweden

[28] Leiden Observatory, Leiden University, PO Box 9513, 2300 RA Leiden, The Netherlands

[29] Astronomy Department, University of Maryland, College Park, MD 20742, USA

[30] AIM, CEA, CNRS, Université Paris-Saclay, Université Paris Diderot, Sorbonne Paris Cité, 91191 Gif-sur-Yvette, France

[31] Instituto de Física e Química, Universidade Federal de Itajubá, Av. BPS 1303, Pinheirinho, 37500-903, Itajubá, MG, Brazil

[32] Bay Area Environmental Research Institute, Moffett Field, CA 94035, USA

[33] Australian Synchrotron, Australian Nuclear Science and Technology Organisation (ANSTO), Victoria, Australia

[34] INAF – Osservatorio Astrofisico di Catania, Via Santa Sofia 78, 95123 Catania, Italy

[35] Bay Area Environmental Research Institute, Moffett Field, CA 94035, USA

[36] Laboratoire de Physique de l'École Normale Supérieure, ENS, Université PSL, CNRS, Sorbonne Université, Université Paris Cité, 75005 Paris, France

[37] Laboratory for Atmospheric and Space Physics, University of Colorado, Boulder, CO 80303, USA

[38] Department of Chemistry, University of Colorado, Boulder, CO 80309, USA

[39] Institute for Modeling Plasma, Atmospheres, and Cosmic Dust (IMPACT), University of Colorado, Boulder, CO 80303, USA

[40] Faculty of Aerospace Engineering, Delft University of Technology, Kluyverweg 1, 2629 HS Delft, The Netherlands

[41] Radboud University, Institute for Molecules and Materials, FELIX Laboratory, Toernooiveld 7, 6525 ED Nijmegen, The Netherlands

[42] School of Physics, University of Hyderabad, Hyderabad, Telangana 500046, India

[43] Department of Physics, Wellesley College, 106 Central Street, Wellesley, MA 02481, USA

[44] Anton Pannekoek Institute for Astronomy (API), University of Amsterdam, Science Park 904, 1098 XH Amsterdam, The Netherlands

[45] Delft University of Technology, Delft, The Netherlands

[46] Laboratoire de Physique des 2 Infinis Irène Joliot-Curie, Université Paris-Saclay, CNRS/IN2P3, Bâtiment 104, 91405 Orsay Cedex, France

[47] Department of Chemistry, GITAM school of Science, GITAM Deemed to be University, Bangalore, India

[48] Institut de Physique de Rennes, UMR CNRS 6251, Université de Rennes 1, Campus de Beaulieu, 35042 Rennes Cedex, France

[49] Department of Chemistry, The University of British Columbia, Vancouver, British Columbia, Canada

[50] National Radio Astronomy Observatory (NRAO), 520 Edgemont Road, Charlottesville, VA 22903, USA

[51] European Space Astronomy Centre (ESAC/ESA), Villanueva de la Cañada, 28692 Madrid, Spain

[52] Observatoire de Paris, PSL University, Sorbonne Université, CNRS, LERMA, 75014 Paris, France

[53] Harvard-Smithsonian Center for Astrophysics, 60 Garden Street, Cambridge MA 02138, USA

[54] Sorbonne Université, CNRS, UMR 7095, Institut d'Astrophysique de Paris, 98bis bd Arago, 75014 Paris, France

[55] Institut Universitaire de France, Ministère de l'Enseignement Supérieur et de la Recherche, 1 rue Descartes, 75231 Paris Cedex 05, France

[56] Department of Physics and Astronomy, Rice University, Houston, TX 77005-1892, USA

[57] Yunnan Observatories, Chinese Academy of Sciences, 396 Yangfangwang, Guandu District, Kunming 650216, PR China

[58] Chinese Academy of Sciences South America Center for Astronomy, National Astronomical Observatories, CAS, Beijing 100101, PR China

[59] Departamento de Astronomía, Universidad de Chile, Casilla 36-D, Santiago, Chile

[60] Departments of Chemistry and Astronomy, University of Virginia, Charlottesville, VA 22904, USA

[61] InterCat and Dept. Physics and Astron., Aarhus University, Ny Munkegade 120, 8000 Aarhus C, Denmark

[62] Laboratory Astrophysics Group of the Max Planck Institute for Astronomy at the Friedrich Schiller University Jena, Institute of Solid State Physics, Helmholtzweg 3, 07743 Jena, Germany

[63] Instituto de Astronomia, Geofísica e Ciências Atmosféricas, Universidade de São Paulo, 05509-090 São Paulo, SP, Brazil

[64] Department of Physics and Astronomy, San José State University, San Jose, CA 95192, USA

[65] Institut de Ciencies de l'Espai (ICE, CSIC), Can Magrans, s/n, 08193 Bellaterra, Barcelona, Spain

[66] ICREA, Pg. Llu í is Company 23, 05010 Barcelona, Spain

[67] Institut d'Estudis Espacials de Catalunya (IEEC), 08034 Barcelona, Spain

[68] European Space Agency, Space Telescope Science Institute, 3700 San Martin Drive, Baltimore MD 21218, USA

[69] Institute of Astronomy, Russian Academy of Sciences, 119017, Pyatnitskaya str., 48, Moscow, Russia

[70] Department of Earth, Ocean, & Atmospheric Sciences, University of British Columbia, V6T 1Z4, Canada

[71] Telespazio UK for ESA, ESAC, 28692 Villanueva de la Cañada, Madrid, Spain

[72] IPAC, California Institute of Technology, Pasadena, CA, USA

[73] LAB, Université de Bordeaux, CNRS, 33615 Pessac, France

[74] Department of Physics and Astronomy, University of Missouri, Columbia, MO 65211, USA

[75] Max Planck Institute for Astronomy, Königstuhl 17, 69117 Heidelberg, Germany

[76] Chemical Sciences Division, Lawrence Berkeley National Laboratory, Berkeley, California, USA

[77] Kenneth S. Pitzer Center for Theoretical Chemistry, Department of Chemistry, University of California – Berkeley, Berkeley, CA, USA

[78] Institut des Sciences Moléculaires, CNRS, Université de Bordeaux, 33405 Talence, France

[79] Department of Chemistry, Massachusetts Institute of Technology, Cambridge, MA 02139, USA

[80] Instituto de Ciencia de Materiales de Madrid (CSIC), Sor Juana Ines de la Cruz 3, 28049 Madrid, Spain

[81] Department of Physics, PO Box 64, 00014 University of Helsinki, Finland

[82] Steward Observatory, University of Arizona, Tucson, AZ 85721-0065, USA

[83] AstronetX PBC, 55 Post Rd W FL 2, Westport, CT 06880, USA

[84] Department of Physics, College of Science, United Arab Emirates University (UAEU), Al-Ain, 15551, USA

[85] National Astronomical Observatory of Japan, National Institutes of Natural Science, 2-21-1 Osawa, Mitaka, Tokyo 181-8588, Japan

[86] California Institute of Technology, IPAC, 770, S. Wilson Ave., Pasadena, CA 91125, USA

[87] Department of Physics, Institute of Science, Banaras Hindu University, Varanasi 221005, India

[88] University of Central Florida, Orlando, FL 32765, USA

[89] Van't Hoff Institute for Molecular Sciences, University of Amsterdam, PO Box 94157, 1090 GD Amsterdam, The Netherlands

[90] Laboratoire de Chimie et Physique Quantiques LCPQ/IRSAMC, UMR5626, Université de Toulouse (UPS) and CNRS, 31062 Toulouse, France

[91] Instituto de Matemática, Estatística e Física, Universidade Federal do Rio Grande, 96201-900, Rio Grande, RS, Brazil

[92] Center for Astrophysics and Space Sciences, Department of Physics, University of California, San Diego, 9500 Gilman Drive, La Jolla, CA 92093, USA

[93] School of Chemistry, The University of Nottingham, University Park, Nottingham NG7 2RD, UK

[94] Astronomy Department, Ohio State University, Columbus, OH 43210 USA

[95] Space Science Institute, 4765 Walnut St., R203, Boulder, CO 80301, USA

[96] Department of Physics, Stockholm University, 10691 Stockholm, Sweden

[97] Department of Physics, Texas State University, San Marcos, TX 78666, USA

[98] Ritter Astrophysical Research Center, University of Toledo, Toledo, OH 43606, USA

[99] Department of Physics, Stockholm University, 10691 Stockholm, Sweden

[100] School of Physics and Astronomy, Sun Yat-sen University, 2 Da Xue Road, Tangjia, Zhuhai 519000, Guangdong Province, PR China

[101] Star and Planet Formation Laboratory, RIKEN Cluster for Pioneering Research, Hirosawa 2-1, Wako, Saitama 351-0198, Japan

[102] Institute of Deep Space Sciences, Deep Space Exploration Laboratory, Hefei 230026, PR China

Appendix A: Contribution of lines and AIBs in imaging bands

Figs. A.1 to A.7 show the three template spectra in Peeters et al. (2023), illustrating the variation of the contribution of different lines into each imaging band. More detailed analysis with a full set of lines will be presented in the science enable product and the associated article (Chown et al. 2023).
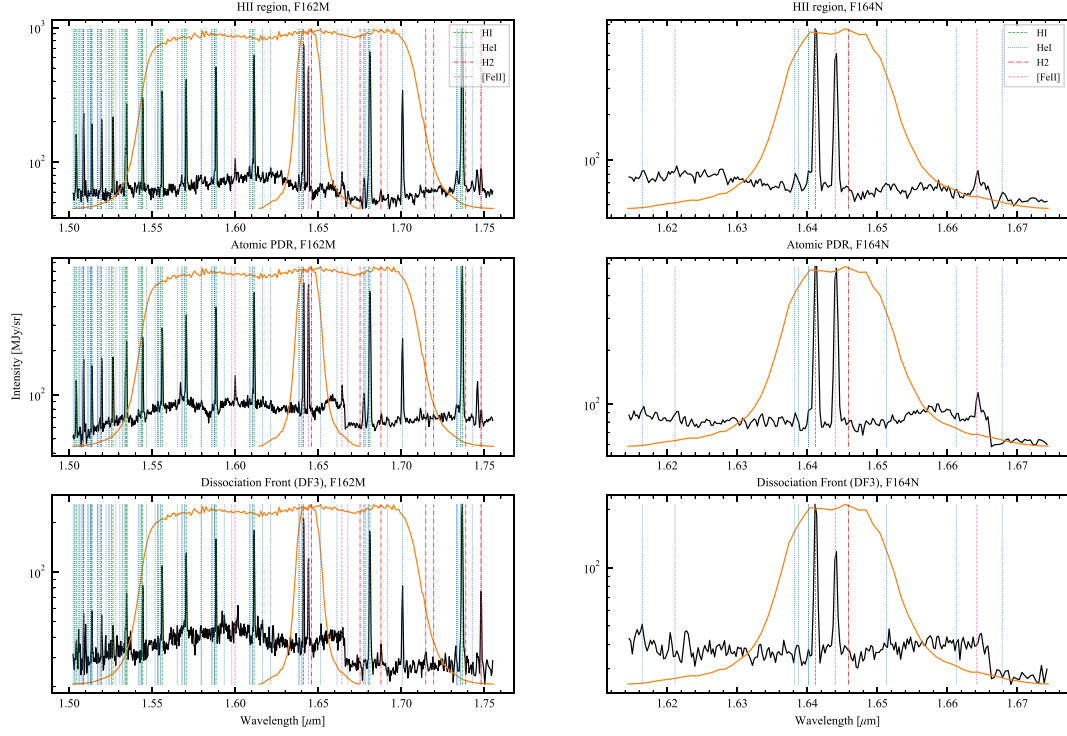
Fig. A.1. Three template spectra (from top to bottom) shown in Peeters et al. (2023) in the range covered by F162M (left) and F164N (right). Response functions of the filters are shown with thin orange lines. Expected positions of HI, HeI, H₂, and [FeII] lines are marked.
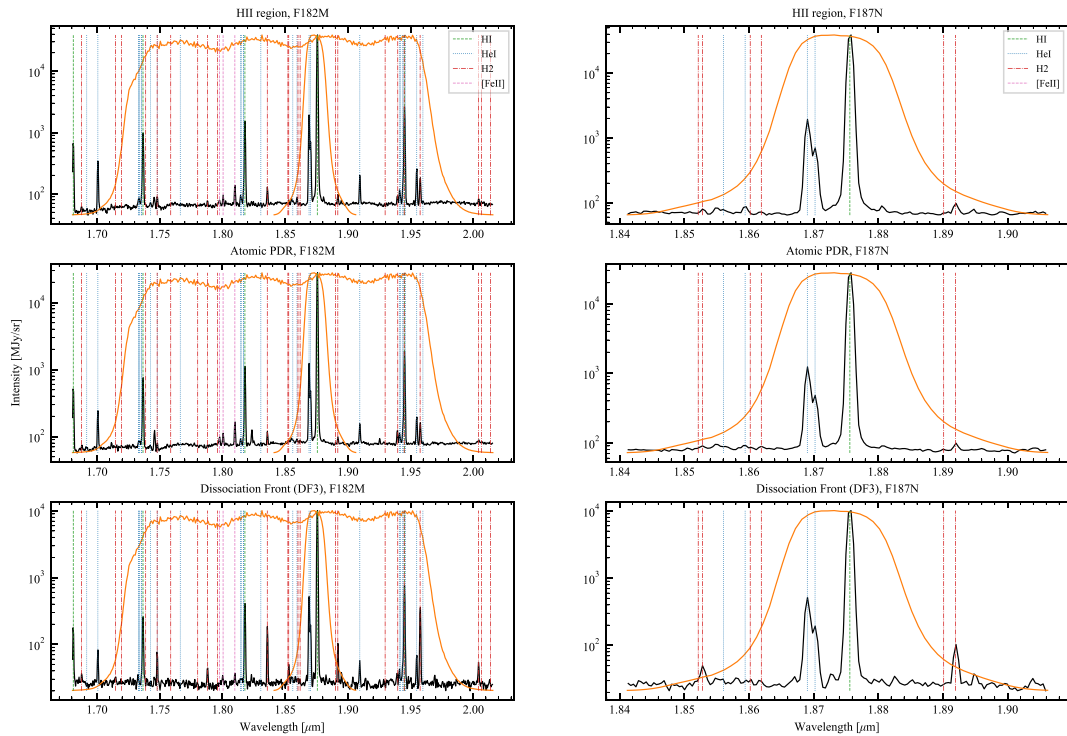
Fig. A.2. Same as Fig. A.1, but for F182M (left) and F187N (right).
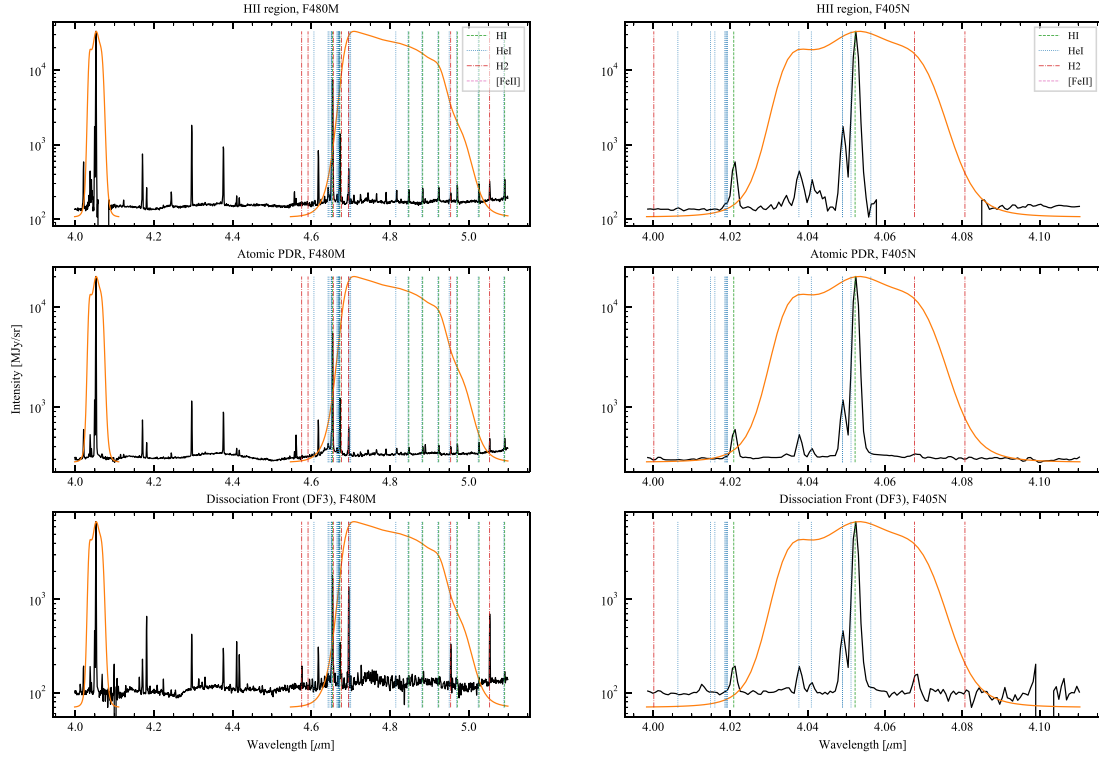
Fig. A.3. Same as Fig. A.1, but for F480M (left) and F405N (right).
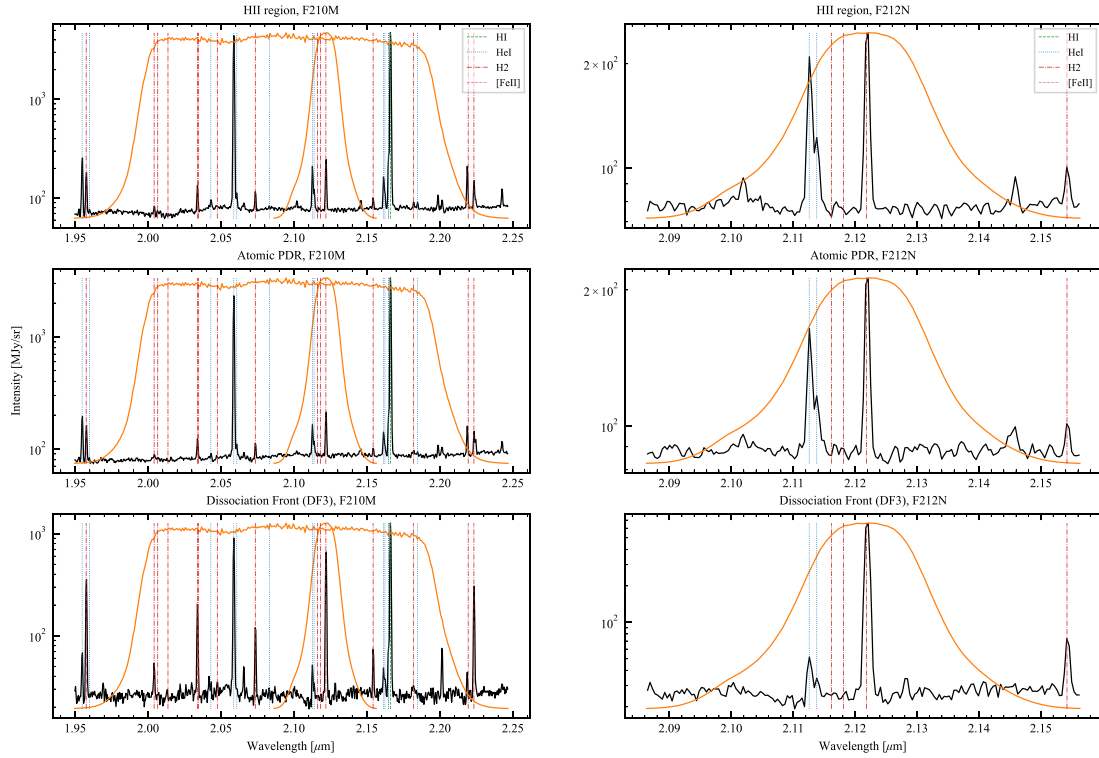
Fig. A.4. Same as Fig. A.1, but for F210M (left) and F212N (right).
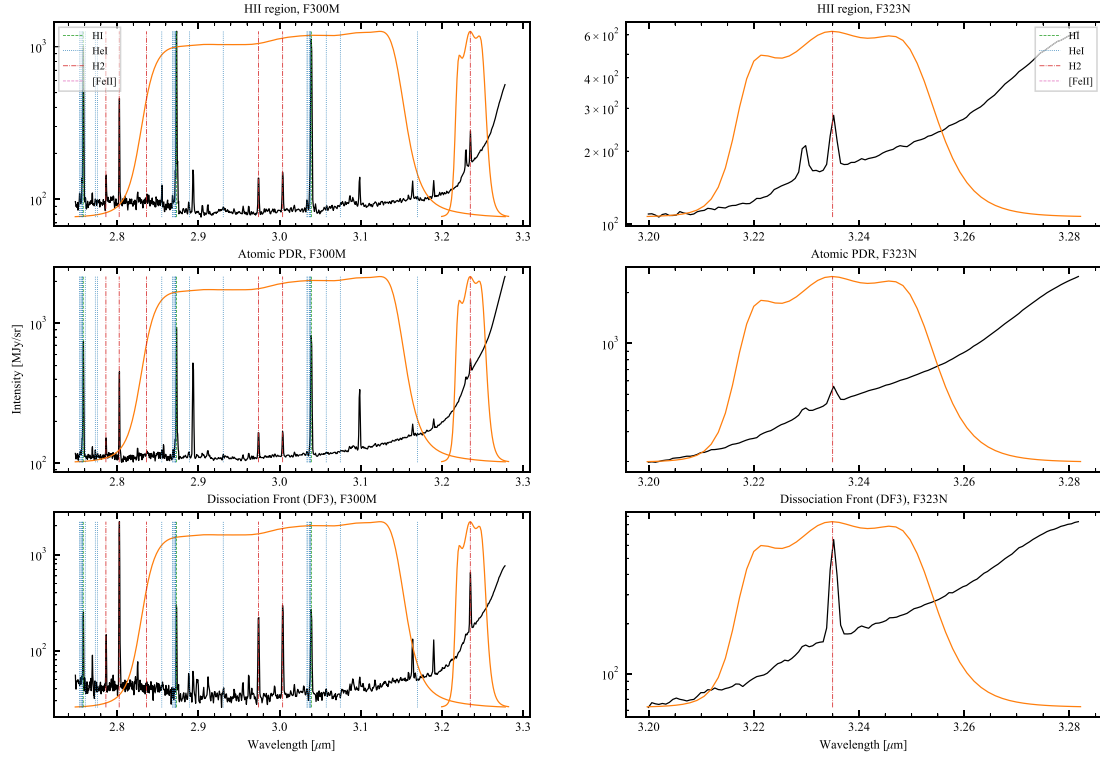
Fig. A.5. Same as Fig. A.1, but for F300M (left) and F323N (right).
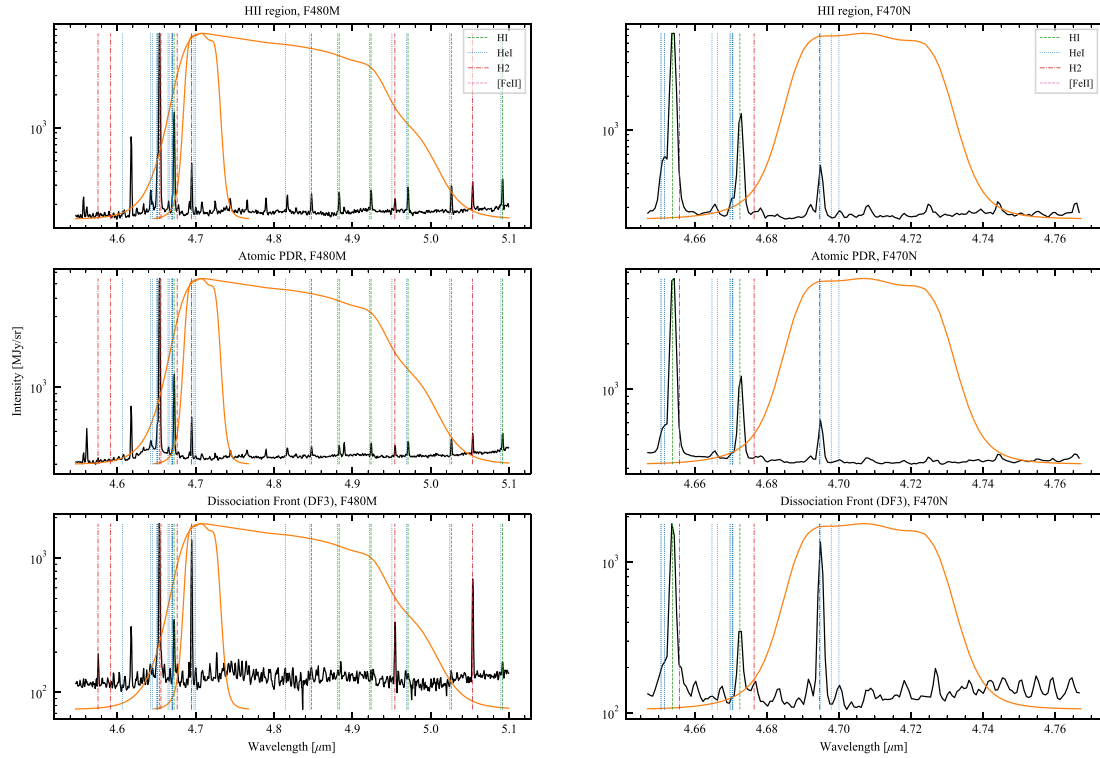
Fig. A.6. Same as Fig. A.1, but for F480 (left) and F470N (right).
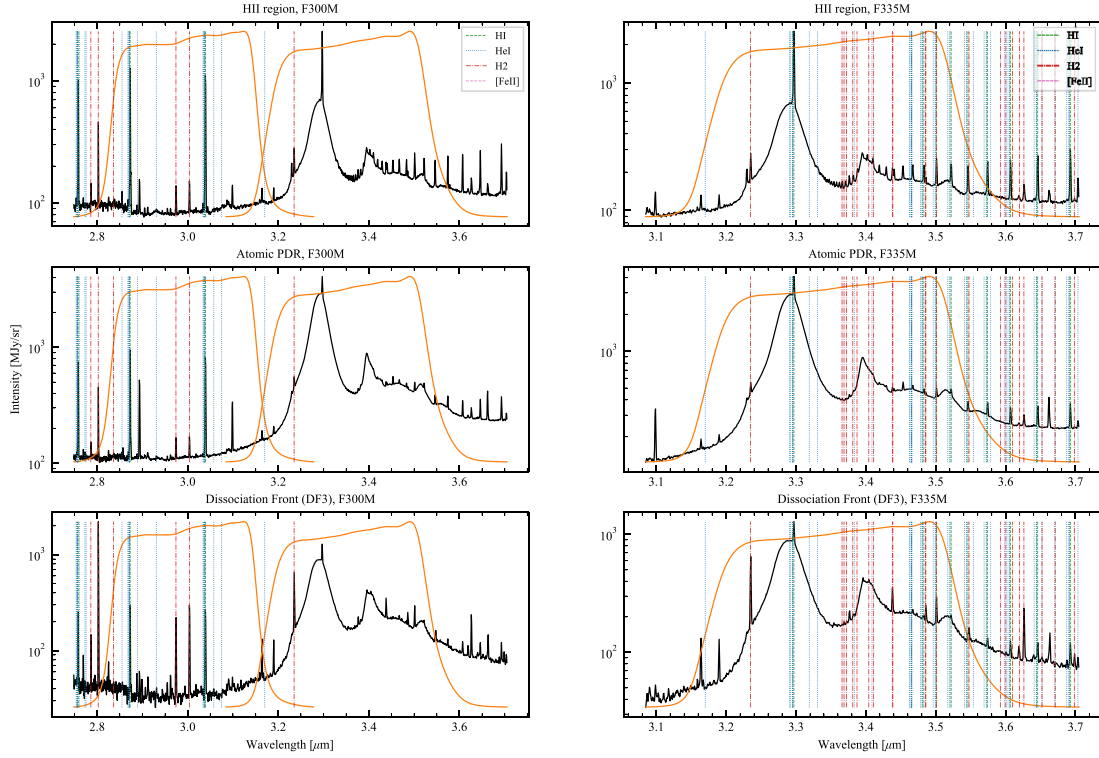
Fig. A.7. Same as Fig. A.7, but for F300M (left) and F335M (right).

Appendix B: JWST and ground-based telescopes images of the Bar

Fig. B.1 shows the composite MIRI images of the southwest part of Bar. This region designated the "SW Bright Bar" in O'Dell et al. (2017b) presents the sharpest ionization front of the Bar. Its structure and physical conditions near the MIF are studied in detail from HST, MUSE and velocity data in their Section 4.3.

Figs. B.2-B.4 present all NIRCam images of the Bar obtained in the filters listed in Table 1, and some filters continuum subtracted. Fig. B.5 shows for the southwestern part of the Bar NIRCAM map of the 0-0 S(9) H_2 line at 4.69 μm, Keck/NIRC2 map of the 1-0 S(1) H_2 line at 2.12 μm, and ALMA maps of the HCO^+ J=4-3 and CO J=3-2 lines.
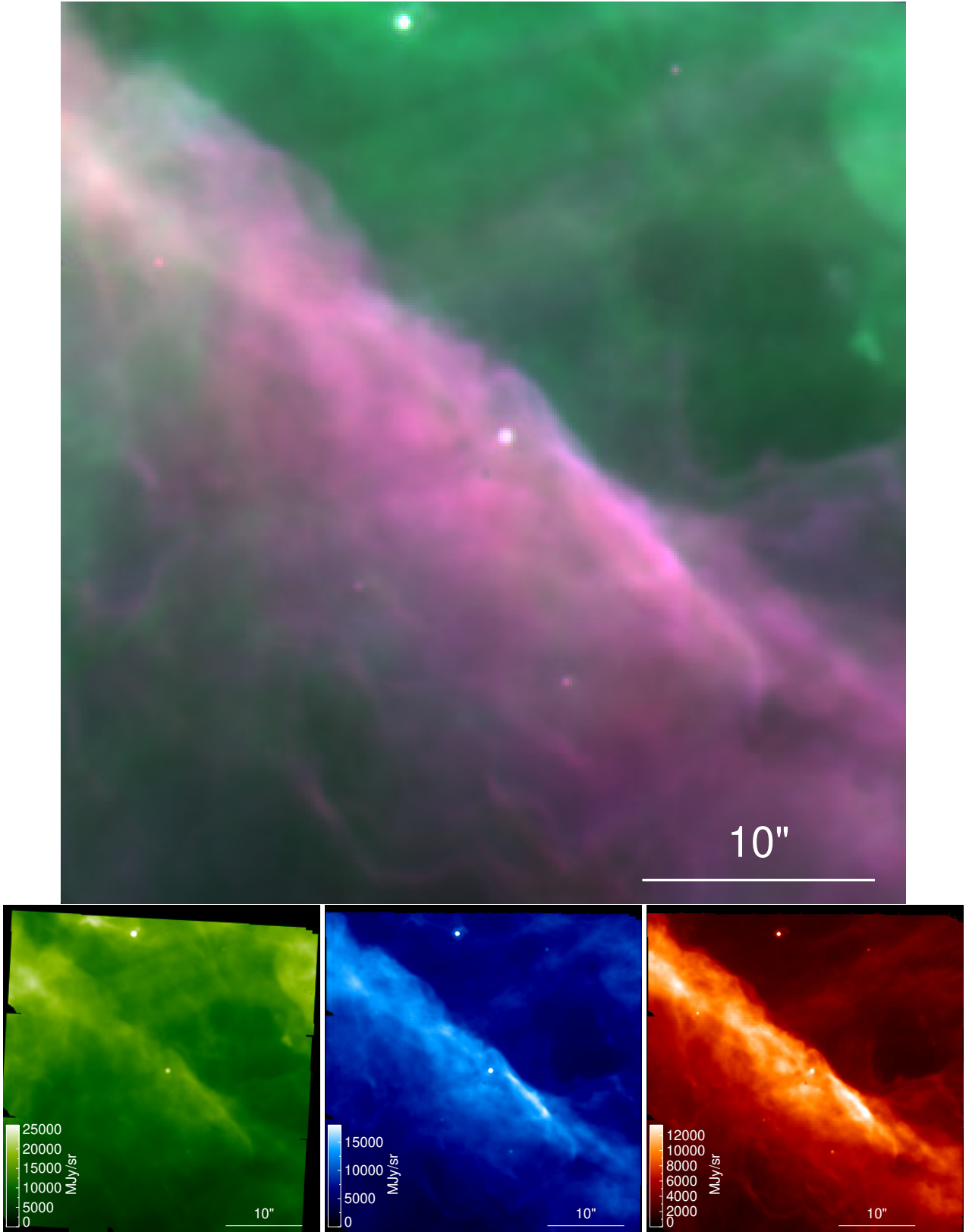
Fig. B.1. Southwestern part of Bar as seen by the JWST's MIRI instrument with north up and east left. Several images in different filters were combined to produce an RGB composite image: $F1500W$ (green), $F1130W$ (blue) and $F770W$ (red) that traces respectively continuum emission from hot/warm dust and hydrocarbons (AIBs). The individual images used to make the RGB composite one are shown below. The size of the images is $\sim 42'' \times 42''$ and it is centered on RA=05^{h}35^{m}20$\overset{s}{.}$33, DEC=-05°25′03.77″ very close the irradiated proto-planetary disk 203-504.
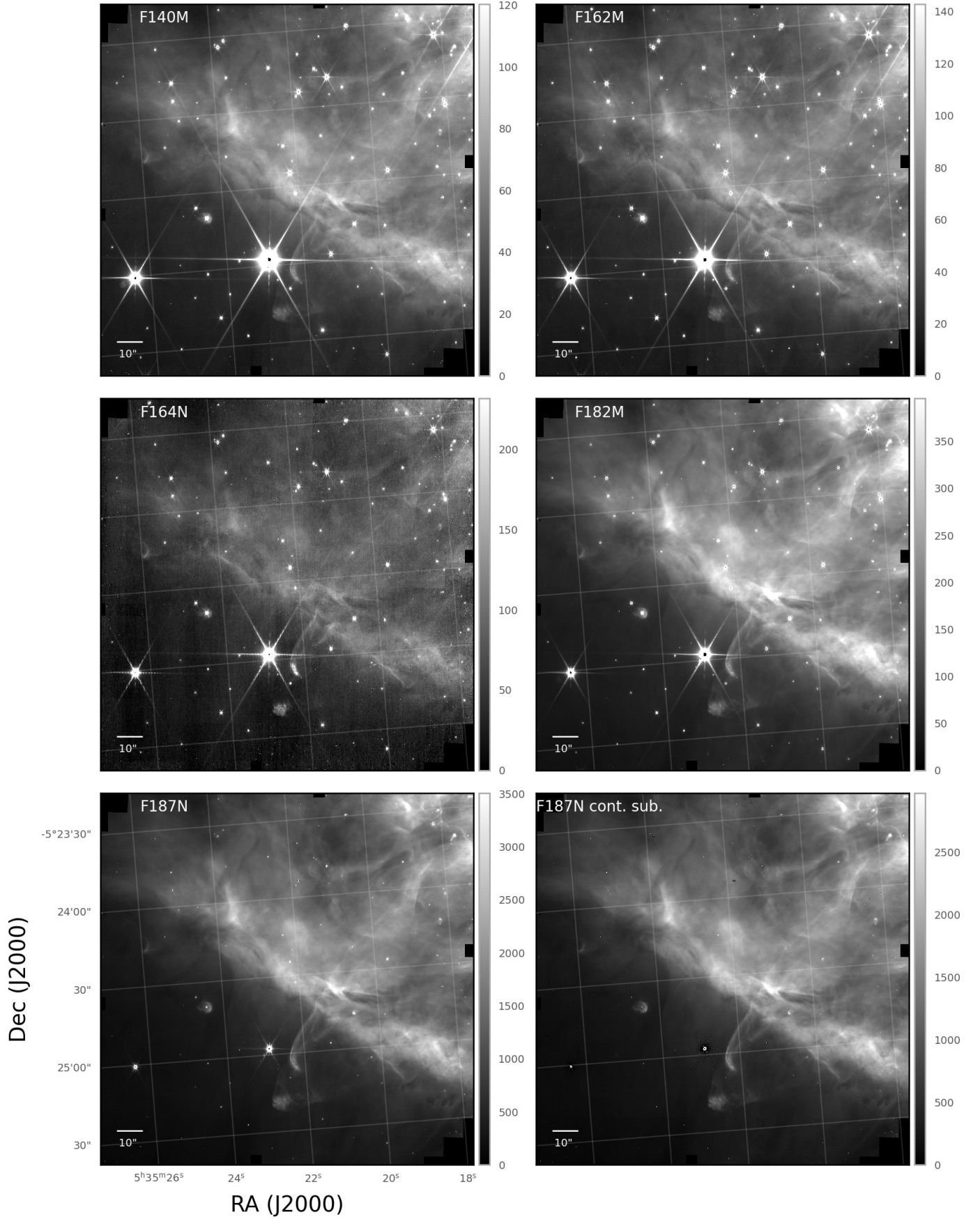
Fig. B.2. NIRCam maps of the Bar in different filters. Units are in MJy/sr.
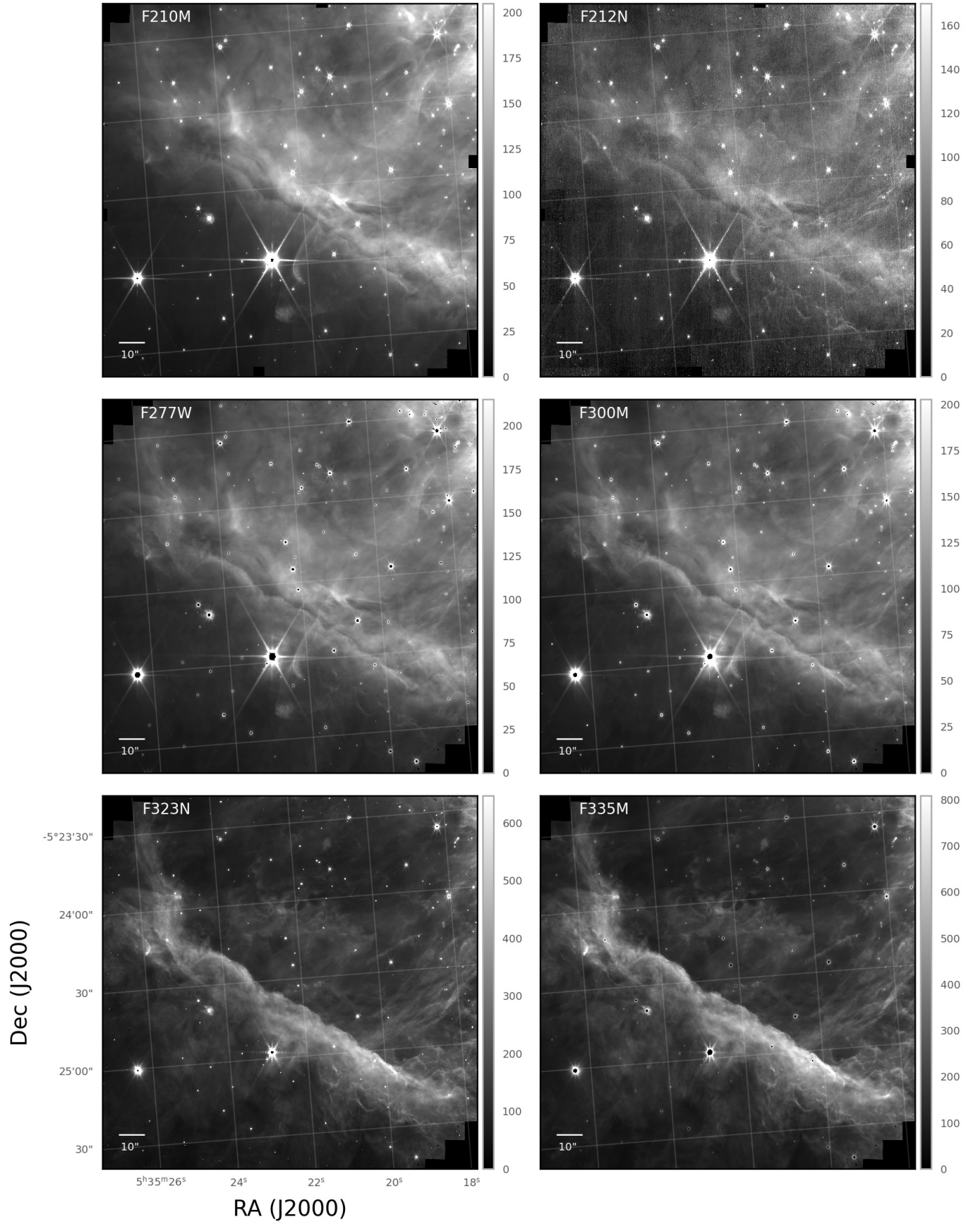
Fig. B.3. Same as Fig. B.2, but for other filters.
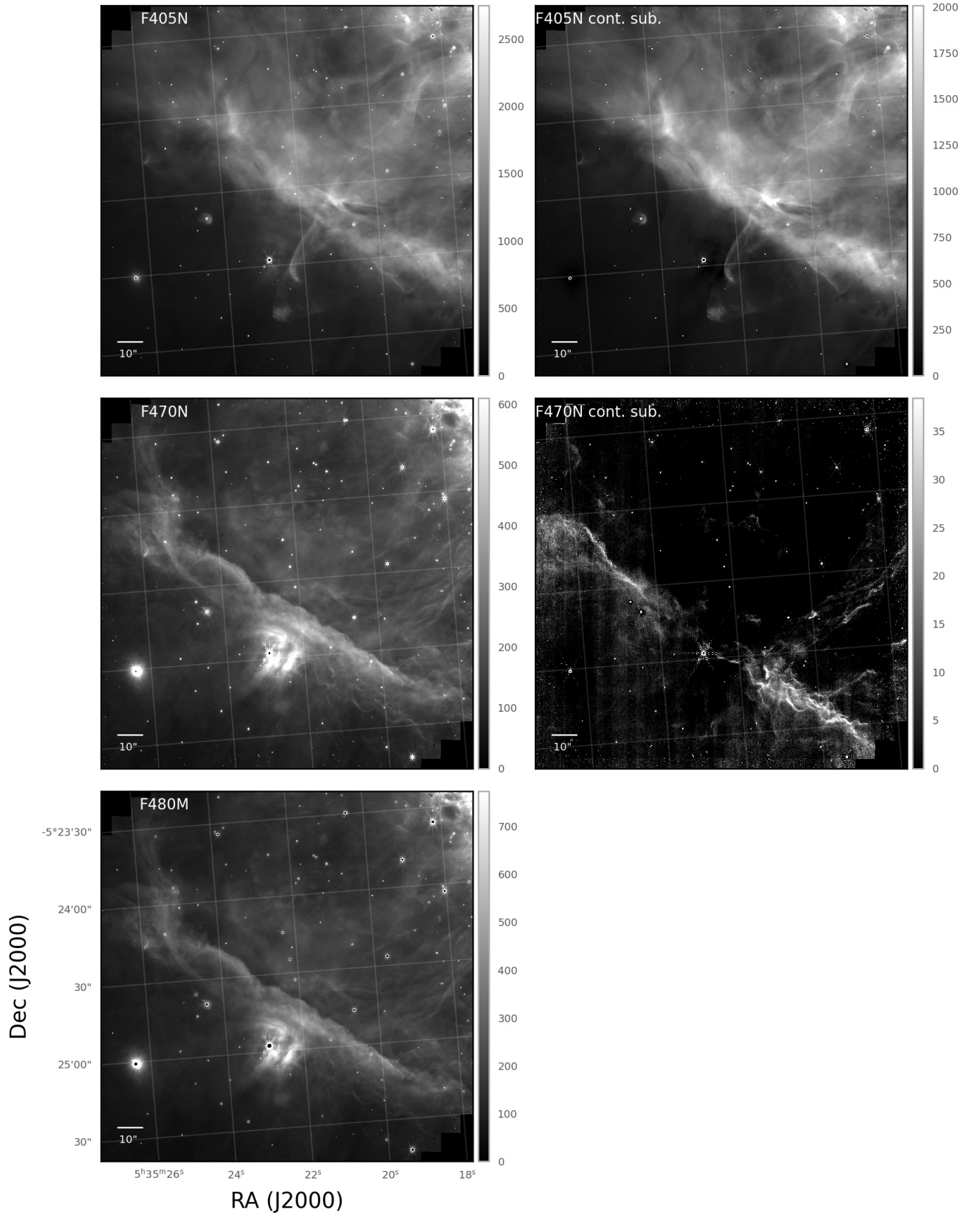
Fig. B.4. Same as Fig. B.2, but for other filters.
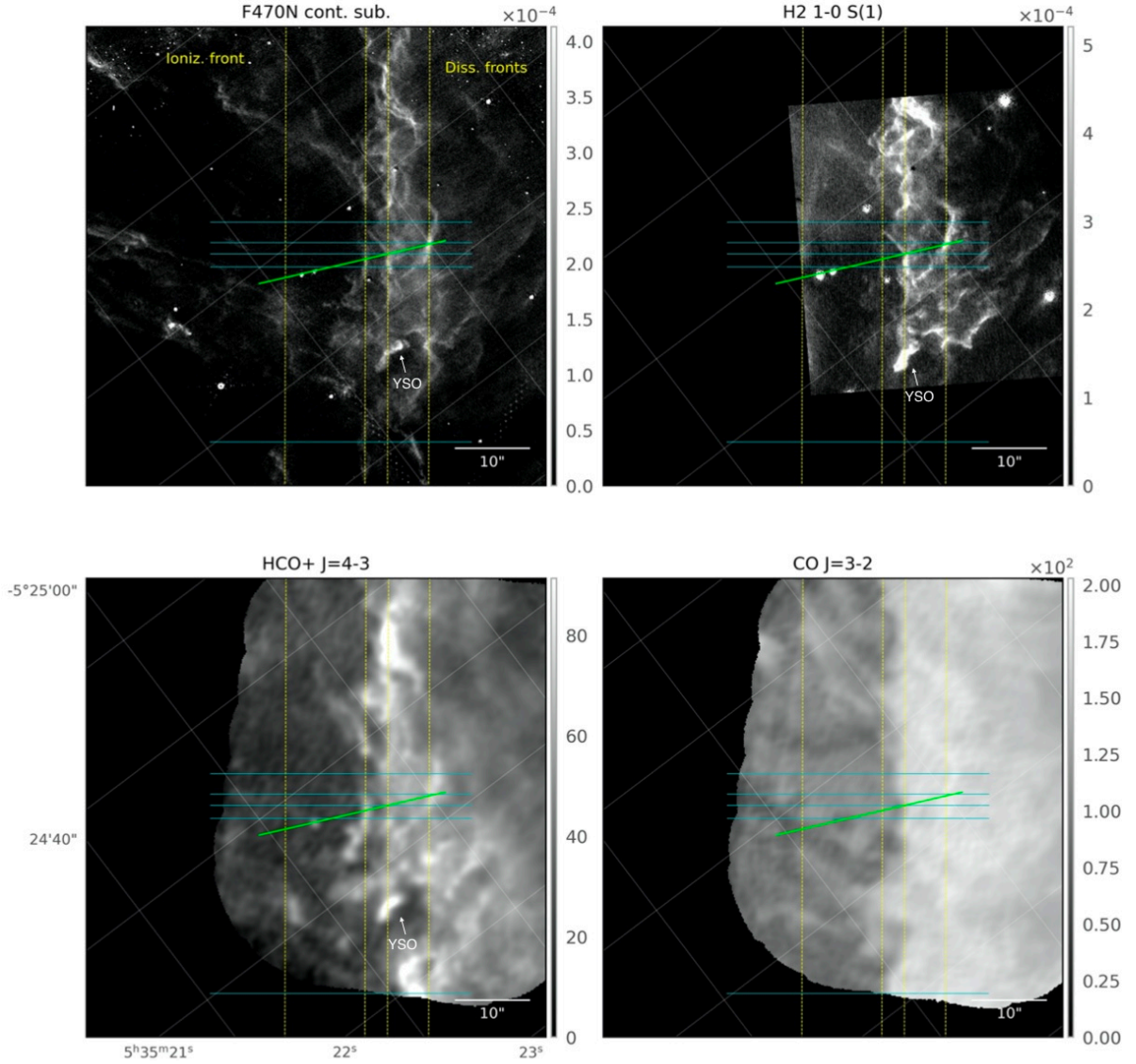
Fig. B.5. NIRCam, Keck and ALMA maps of the southwestern part of Bar. The maps have been rotated so that the ionizing radiation strikes the Bar from the left. **Upper left**: Map in the F470N filter continuum subtracted (H$_2$ 0-0 S(9) line at 4.7 μm). Units are in erg s^{-1} cm^{-2} sr^{-1}. **Upper right**: Keck/NIRC2 map of the H$_2$ 1-0 S(1) line at 2.12 μm with a resolution of 0.085″ (Habart et al. 2023). Our NIRCam observations show a very good agreement with Keck/NIRC2 observations in terms of line distribution and intensity. **Lower left and right**: ALMA observation at 1″ resolution of the HCO$^+$ J = 4-–3 line integrated intensity (in K km s^{-1}) and the CO J=3-2 line peak temperatures (T_{peak}) (Goicoechea et al. 2016). There exists a remarkably similar spatial distribution between the H$_2$ and HCO$^+$ emission from ALMA.

Appendix C: NIRCam images of the north of the Dark Bay, north of M42 and M43

In this Appendix, we present several prominent features arising in the images within the fields centered on north of the Dark Bay, north of M42 and M43 obtained in the NIRCam parallel mode. Figs. C.1, C.2 and C.4. show composite images in three selected filters F187N, F335M and F470N in north of the Dark Bay and F187N, F335M and F212N in north of M42 and M43. As in the field centered on the Bar, the molecular cloud border appears quite structured. Multiple patterns emerge such as ridges, waves, evaporating globules and bow-shocks (Fig. C.3). In Figs. C.5-C.11, all the images obtained in the filters listed in Table 1, and some filters continuum subtracted, are presented. Figs. C.12, C.13, C.14, C.15 show the proplyds detected in the north of the Dark Bay and M43. New proplyd candidates identified in the NIRCam F187N images of the north of the Dark Bay and M43 are given in Table C.1.

Appendix C.1. North of the Dark Bay

The NIRCam images of the material North of the Dark Bay reveal that there are linear bright features, such as the Bar (panels A and B in Figs. C.1 and C.3). Some of these features were previously seen in extinction corrected HST images (e.g., eastern and northern bright bar in Fig. 6 of O'Dell 2001b). The Dark Bay (and similar structures) are foreground extinction of visible light (Fig. 1) but seen in emission in PDRs tracers, such as AIBs and H_2 observed with NIRCam, and [CII] cooling line emission from *Herschel* and SOFIA (Goicoechea et al. 2015; Pabst 2021). The AIBs and H_2 line emission show the edges of these neutral warm regions with a very high level of detail. The bright PDR features (panels A and B in Figs. C.1 and C.3), which are at a projected distance of the order of $110''$-$120''$ (0.22-0.24 pc) from the illuminating O7-type star θ^1 Ori C, are illuminated by a strong FUV radiation field comparable to the one on the Bar. Goicoechea et al. (2015) studied with *Herschel*/HIFI the [CII] velocity emission along with the CO J=2-1 line with IRAM-30m and found that most of these PDRs lack detectable CO emission (CO-dark molecular gas). In the northern-west part of the NIRCam map, there is a zone devoid of nebula emission where background stars are well visible. This is in agreement with the fact that no CO emission was previously detected and that this region does not contain much dense molecular gas.

In the southwest corner of the continuum subtracted H_2 0-0 S(9) 4.69 μm line map (Fig. C.7), several very bright features produced by shocks are detected. No AIB emission or Pa α and [FeII] line emission are detected on these features. The well studied outflow HH 513 lies in this region. Furthermore, several arches (like a bent-over cylinder) which are most likely bow-shocks are detected in the southest corner of field (see panel A in Figs. C.1 and C.3). Bow-shocks can also be the result of multiple outflows that are close together in time like seen from the ground in clusters in various star-forming regions (Plunkett et al. 2013; Nony et al. 2020).

Appendix C.2. North of M42

Here, we present images within the fields covered the north of M42 obtained in the NIRCam parallel mode. As shown by the ionized gas line map in Fig. C.2, the north of M42 contains one main ionized gas region in the southwest part of the map. This region is irradiated by the Trapezium cluster. At the edge of the ionized region are the neutral zones, the PDRs. Particularly interesting PDRs are the ones in panel C in Figs. C.2 and C.3 which are irradiated from the South by star θ^1 Ori C and from the north by the B0.5V star NU Ori in the center of M43 (see Sect. Appendix C.3). As shown in Fig. C.2, a remarkable spatial correlation is observed between the F335M filter (AIBs) and the F212N filter (vibrationally excited line H_2 1-0 S(1)). Most likely, these PDRs are in a lower G_0/n_H regime than in the Bar. In fact, the incident FUV flux from the south on that PDR can be estimated to be about 10 times lower than in the Bar considering the projected distance from the star θ^1 Ori C. For lower G_0/n_H, the H^0/H_2 transition is not driven by dust opacity but by H_2 self shielding (e.g, Hollenbach & Tielens 1999), and the H_2 emission peak is expected to spatially coincide with the emission peak of the AIBs. Spatial coincidence between H_2 and AIB emission peaks has been observed in several lower excited PDRs such as the ρ Oph-W and Horsehead nebula PDR (e.g., Habart et al. 2003; Habart et al. 2005). In high G_0/n_H regime (as at the main edge of the Bar), where the H^0/H_2 is driven by dust opacity and H_2 is mostly photo-dissociated in the outer PDR layers ($A_V < 1$), H_2 emission appears after the emission peak of the AIBs. In the panel C of Fig. C.3, a thin structure (width of $1''$), probably an Evaporating Gaseous Globule, is detected at the PDR edge.

Appendix C.3. M43

As shown in Fig. C.4, M43 contains one main ionized gas region. M43 exhibits an expanding bubble structure, with an expansion velocity of 6 km s^{-1} (Pabst et al. 2020). Looking at the NIRCam images, the UV flux appears significantly lower than in the inner Orion Nebula. The Pa α line is in fact much less bright that in the inner region of the nebula. The emission in the F335M filter is also significantly weaker. This is expected due to the much cooler and less luminous exciting star NU Ori. Pabst et al. (2020, 2022) estimated the local PDR physical conditions in M43, the incident radiation field G_0 ($\sim 10^3$) and the gas density n from the SED results and their [C II] and CO data. In the rim of M43, Pabst et al. (2020) found $n = 10^4$ cm^{-3} from the [C II] and CO peak separation. Gas temperature estimated from [CII] excitation temperature is about 100-120 K. Thus, the thermal pressure must be around few 10^6 K cm^{-3}, 10 to 100 times lower than in the Bar. The PDRs around M43 are bright in aromatic emission but quite faint in H_2. This is consistent with the fact that the density should not be too high ($n \leq 10^4$ cm^{-3}). The conditions of the local PDR are compatible with the conditions of pressure equilibrium with the ionized region using the results of O'Dell & Harris (2010). From their M43 Samples A in Table 10, the averages electronic temperature and density are $T_e = 7950 \pm 60$ K and $n_e = 510 \pm 40$ cm^{-3}.
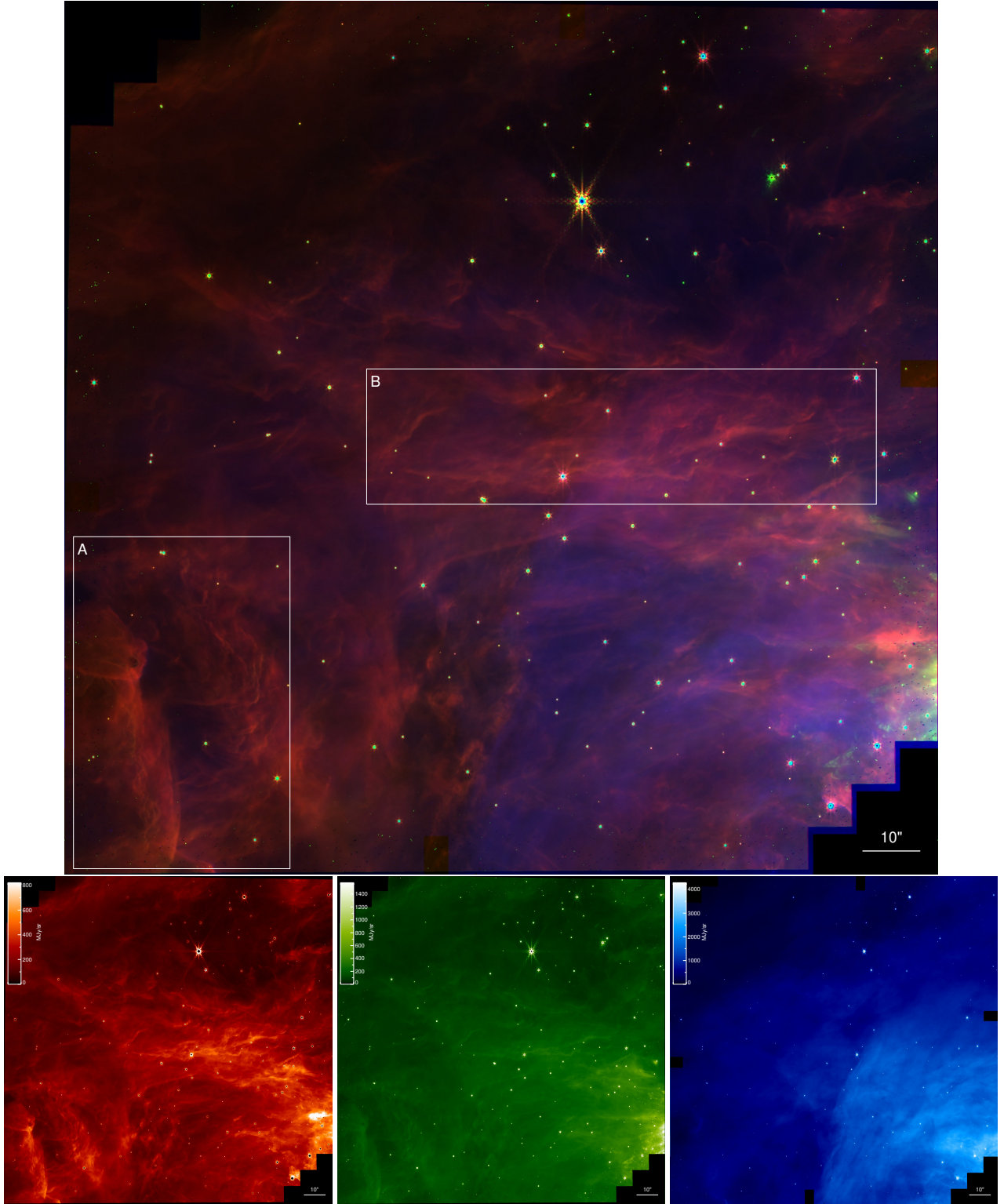
Fig. C.1. The North of the Dark Bay as seen by the JWST's NIRCam instrument with north up and east left. Several images in different filters were combined to produce an RGB composite image as in Fig. 3: F335M (red), F470N (green) and F187N (blue) that trace emission from hydrocarbons (AIBs), dust and molecular gas (H$_2$ 0-0 S(9) line), and ionized gas (Pa α line), respectively. The individual images used to make the RGB composite one are shown below. No continuum was subtracted. The size of the images is ~150″ × 150″ and it is centered on RA=05^{h}35^{m}21^{s}09, DEC=-05°21′40″01. White boxes (labeled A, B) are enlarged in Fig. C.3.
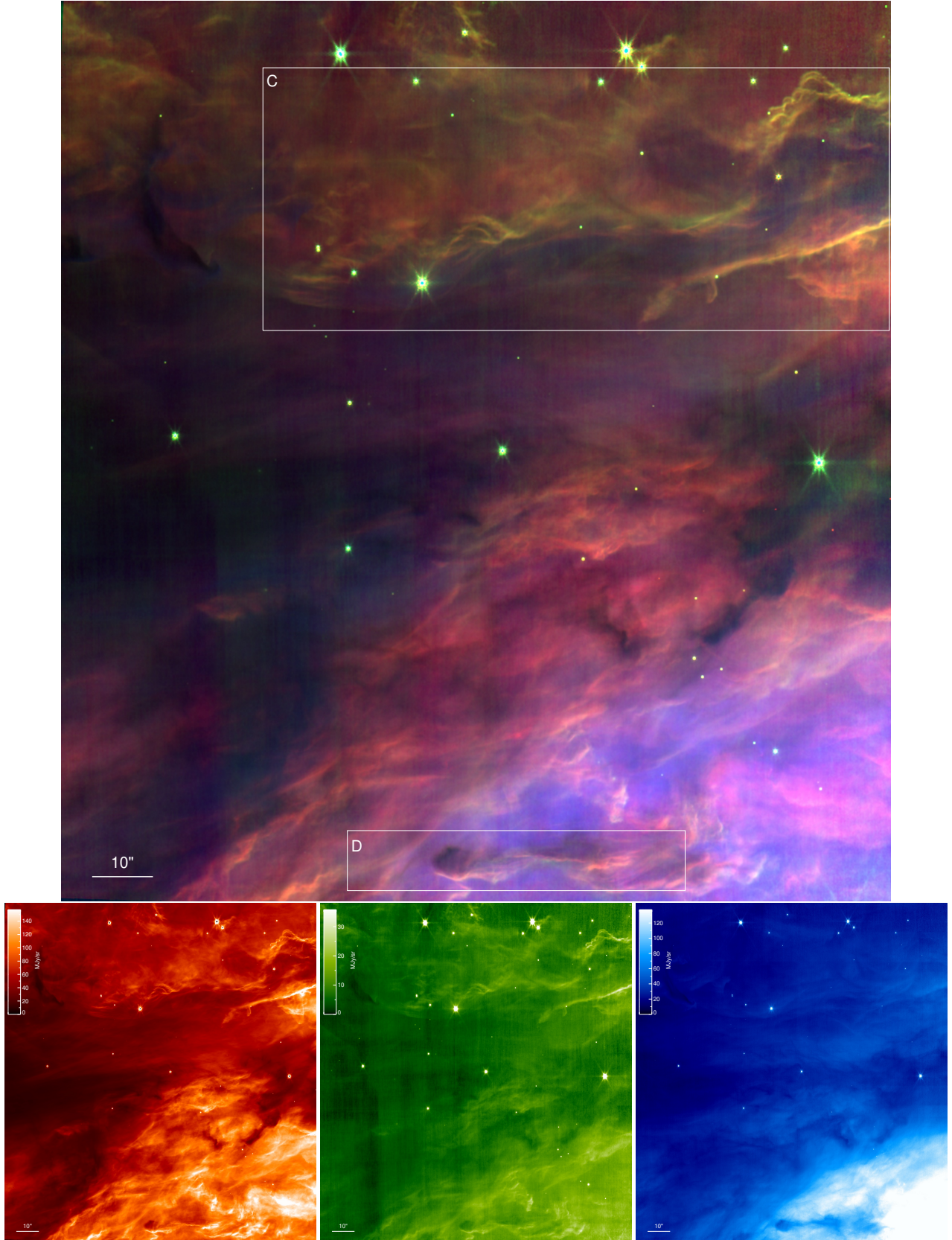
Fig. C.2. North of M42 as seen by the JWST's NIRCam instrument with north up and east left. Several images in different filters were combined to produce an RGB composite image : F335M (red), F212N (green) and F187N (blue) that traces respectively emission from hydrocarbons (AIBs), molecular gas (H$_2$ 1-0 S(1) line) and ionized gas (Pa α line), respectively. The individual images used to make the RGB composite one are shown below. No continuum was subtracted. The image field was chosen to have an overlap between the different individual images. The size of the images is $\sim$135$''$ $\times$ 145$''$ and it is centered on RA=05^{h}35^{m}29^{s}12, DEC=-05$°$20$'$3.66$''$. White boxes (labeled C, D) are enlarged in Fig. C.3.
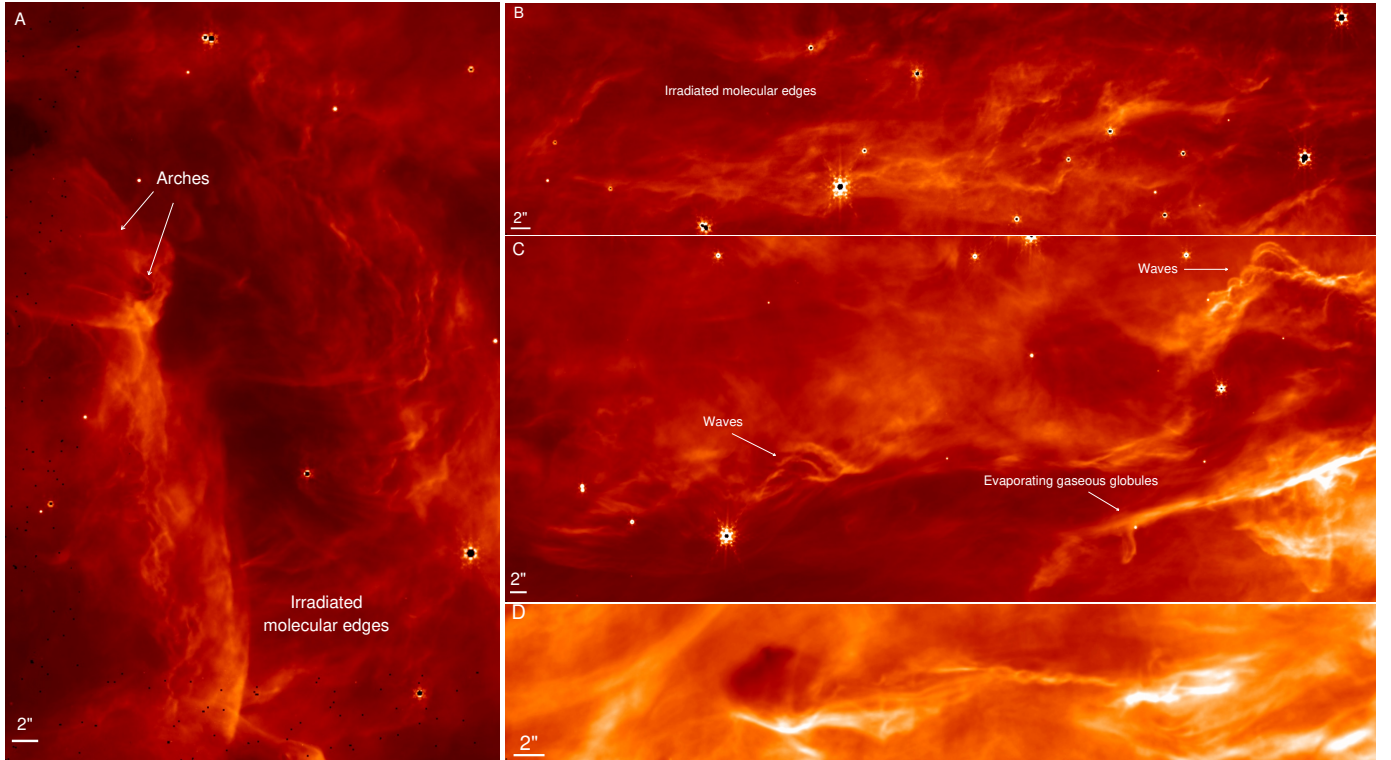
Fig. C.3. Zoom into the F335M image areas shown in Figs. C.1 (for panels A, B) and C.2 (for panels B, C). **A** Irradiated molecular edges showing many patterns such as ridges and arches (which are most likely bow-shocks) detected in the southeast area of M42 North. **B** Irradiated molecular edges detected in the north area of M42 North. **C** Irradiated molecular edges showing many patterns such as ridges, waves and evaporating gaseous globule detected in the northwest area of the M43 South field. **D** Features driven by a large outflow detected in the south area of the M43 South field.

Table C.1. New proplyd candidates identified in the NIRCam F187N images of M42 north and M43 (module A).

Proplyd[a]	α_{J2000}	δ_{J2000}	Region	Comments	2MASS
171 − 212	05 35 17.14	−05 22 11.9	M42	bright cusp with tail	no
180 − 218	05 35 18.04	−05 22 18.2	M42	near to filament, no tail	no
234 − 104	05 35 23.37	−05 21 03.7	M42	faint cusp, no tail	no
269 − 1713	05 35 26.87	−05 17 12.9	M43	bipolar jet, HH objects	yes, star

[a]Proplyd name following O'Dell & Wen (1994) coordinate-based convention.
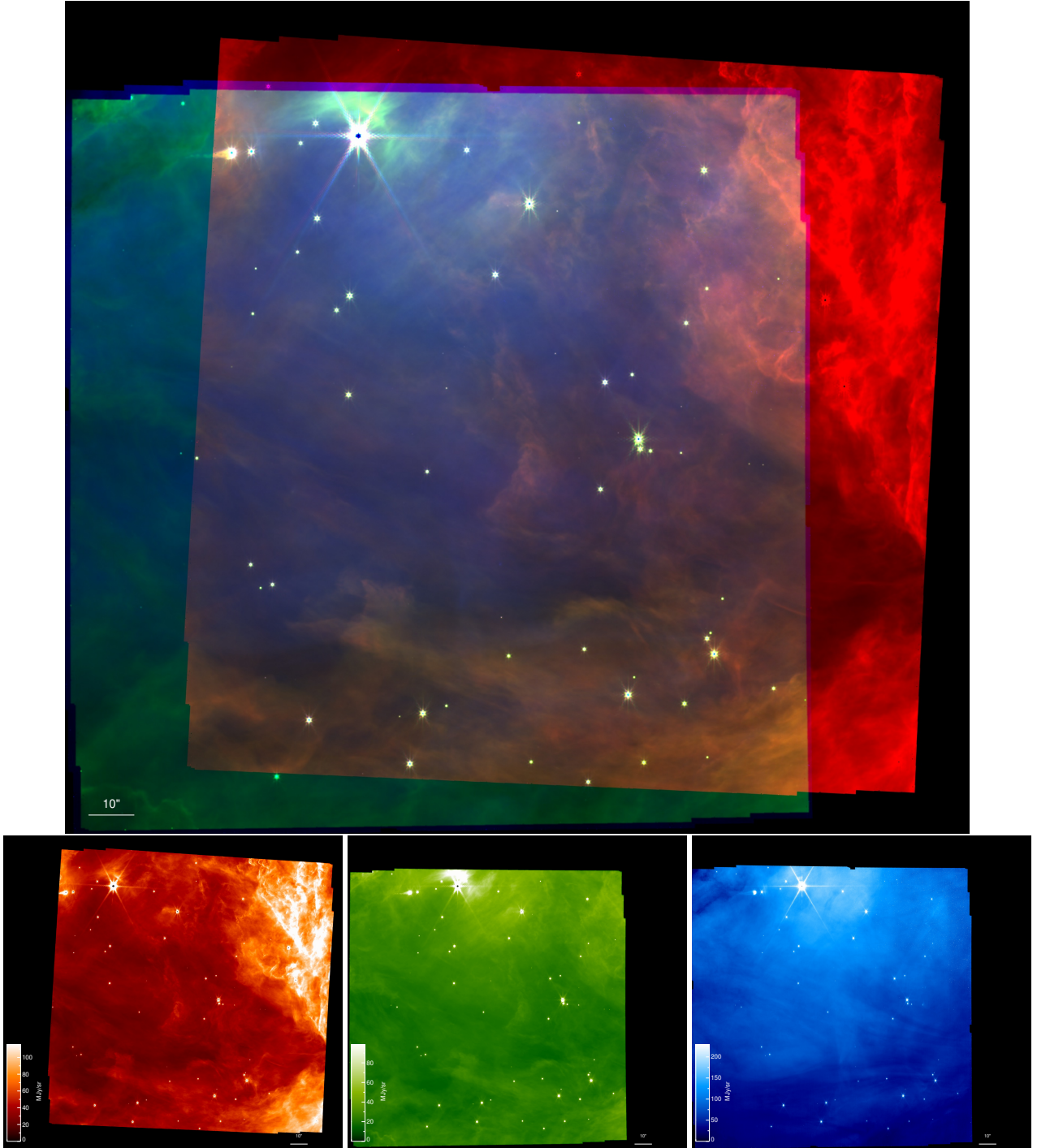
Fig. C.4. The M43 region as seen by the JWST's NIRCam instrument with north up and east left. Several images in different filters were combined to produce an RGB composite image : F335M (red), F212N (green) and F187N (blue) that traces respectively emission from hydrocarbons (AIBs), molecular gas (H$_2$ 1-0 S(1) line) and ionized gas (Pa α line), respectively. The individual images used to make the RGB composite one are shown below. No continuum was subtracted. The size of the images is ~158″ × 158″ and it is centered on RA=05^{h}35^{m}28^{s}92, DEC=-05°17′04.31″.
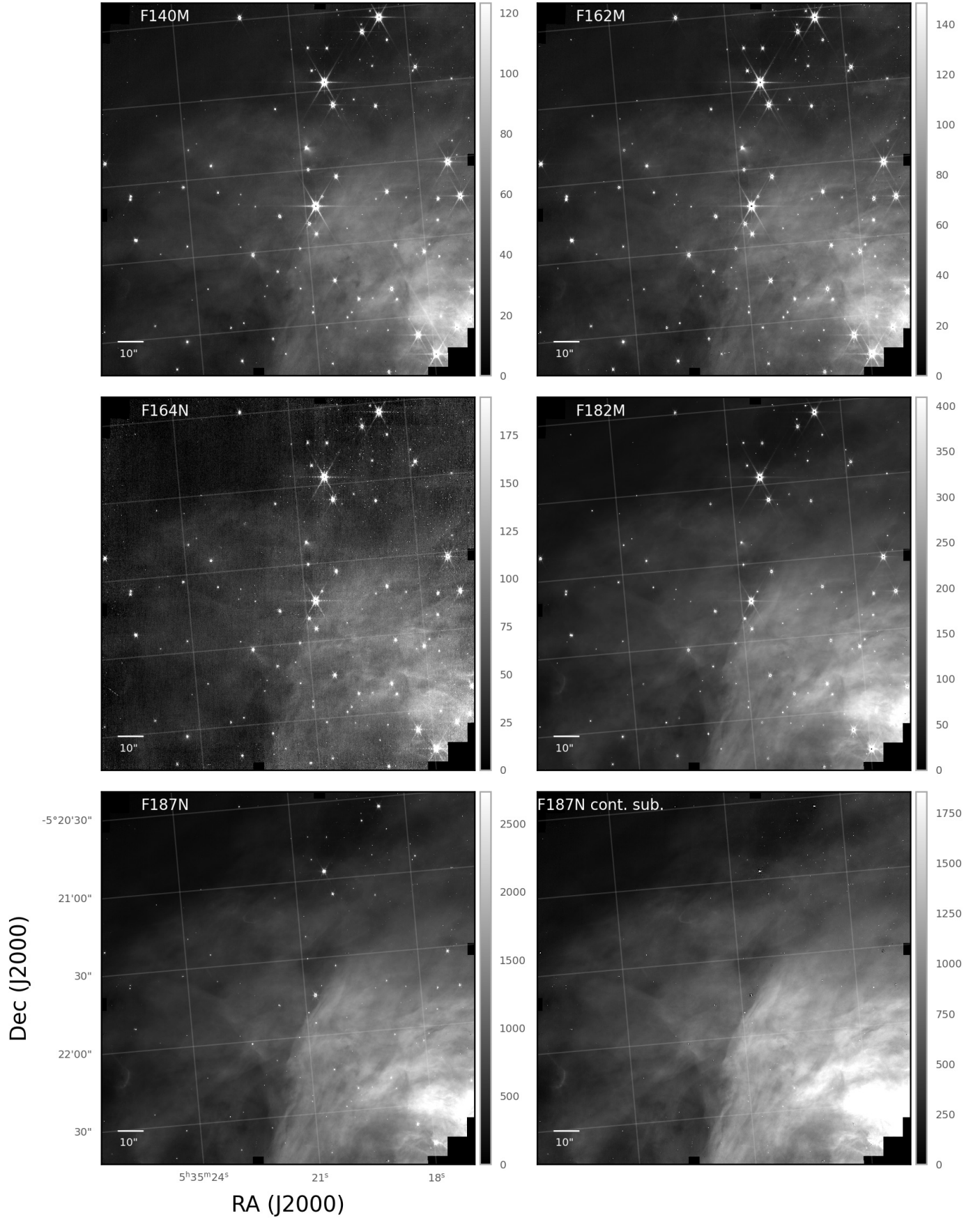
Fig. C.5. NIRCam maps of the North region of the Orion Nebula in different filters. Units are in MJy/sr.
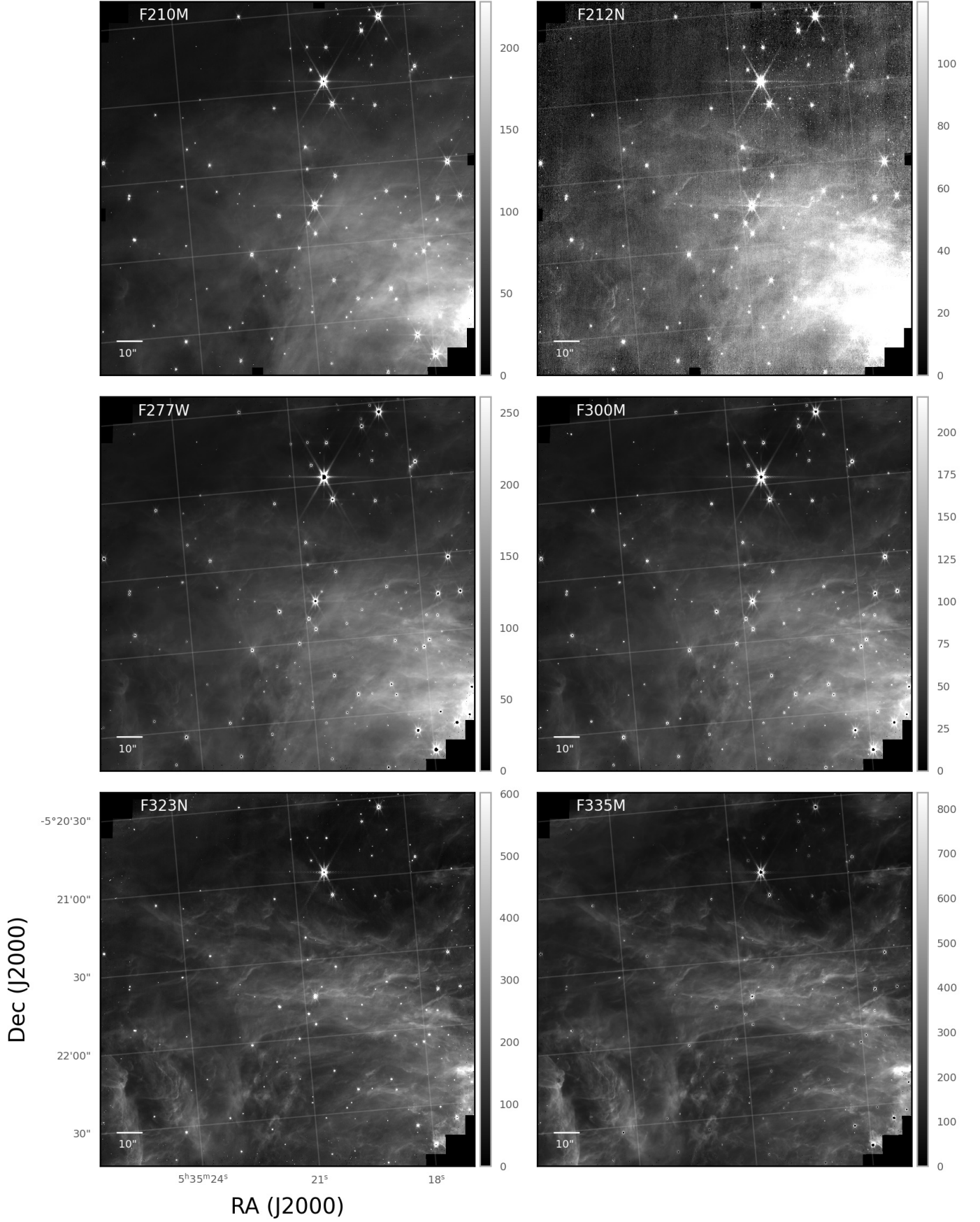
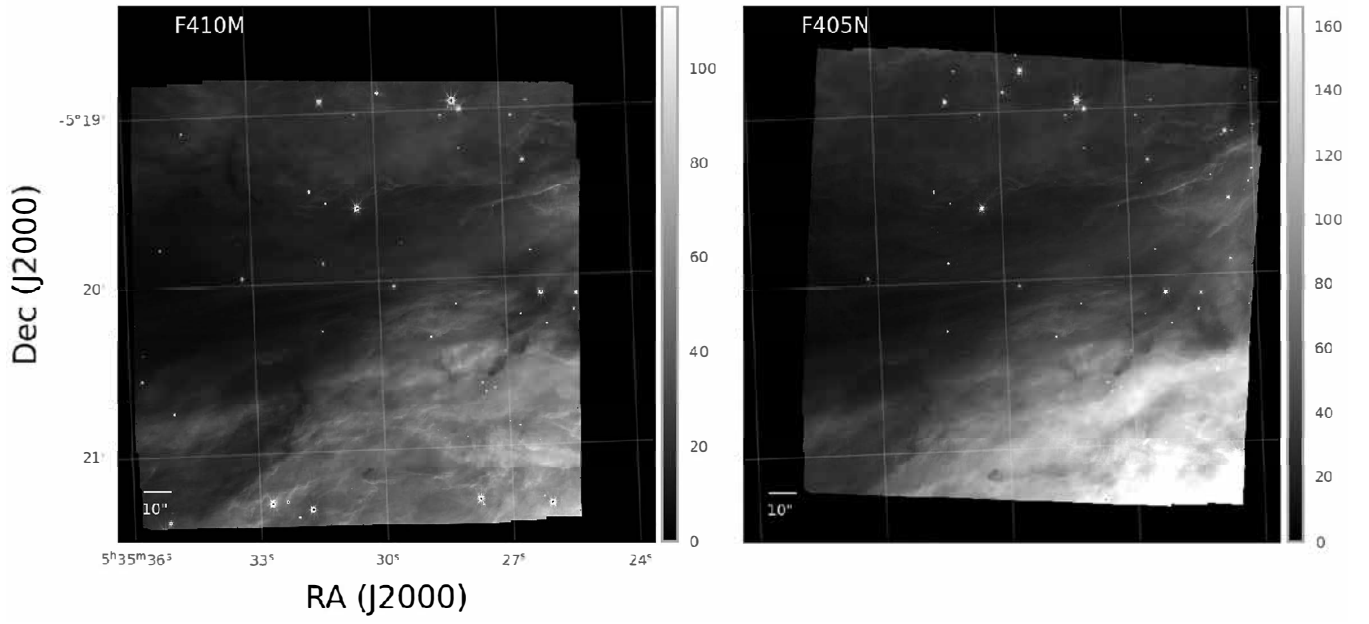**Fig. C.6.** Same as in Fig. C.5, but for other filters.
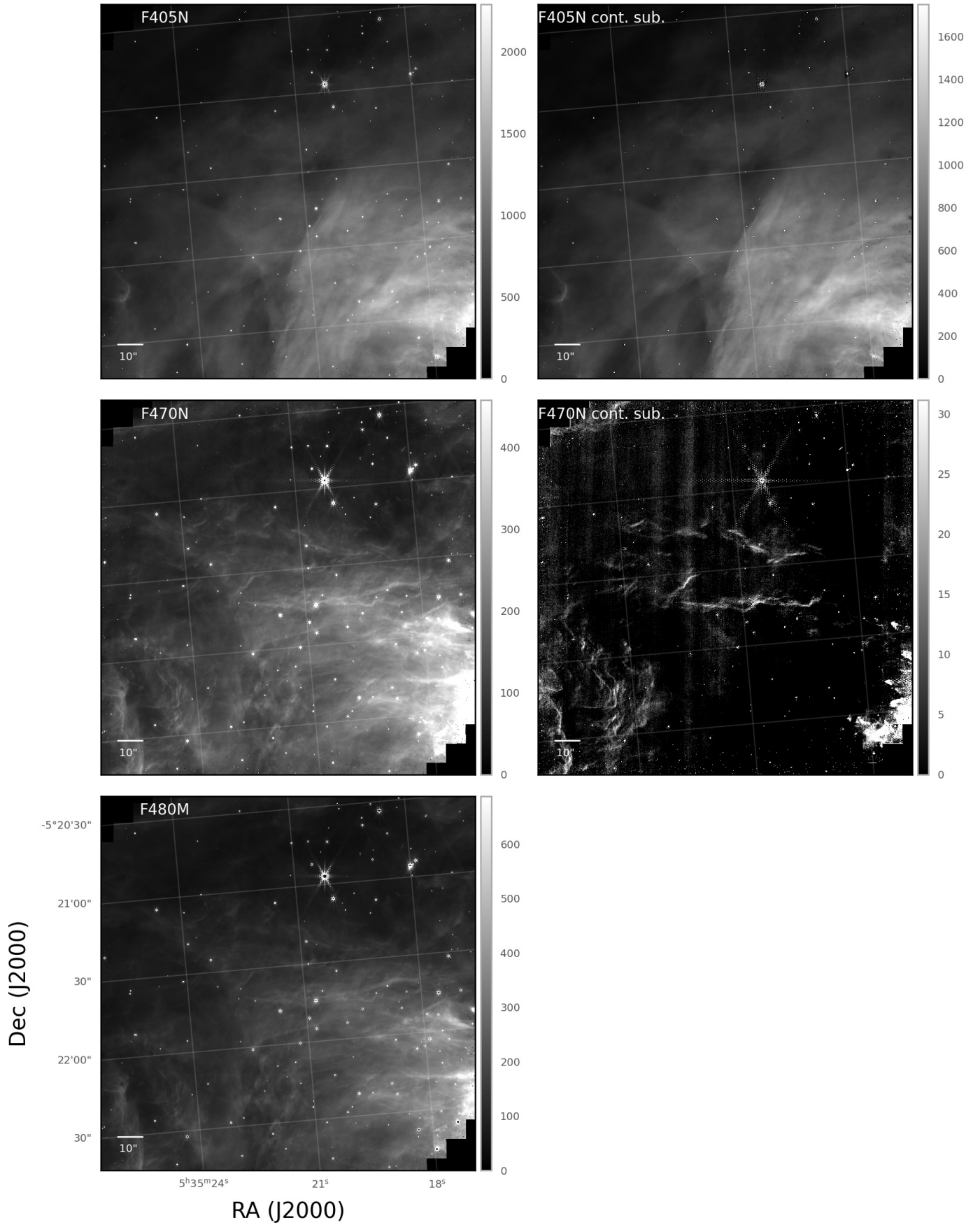
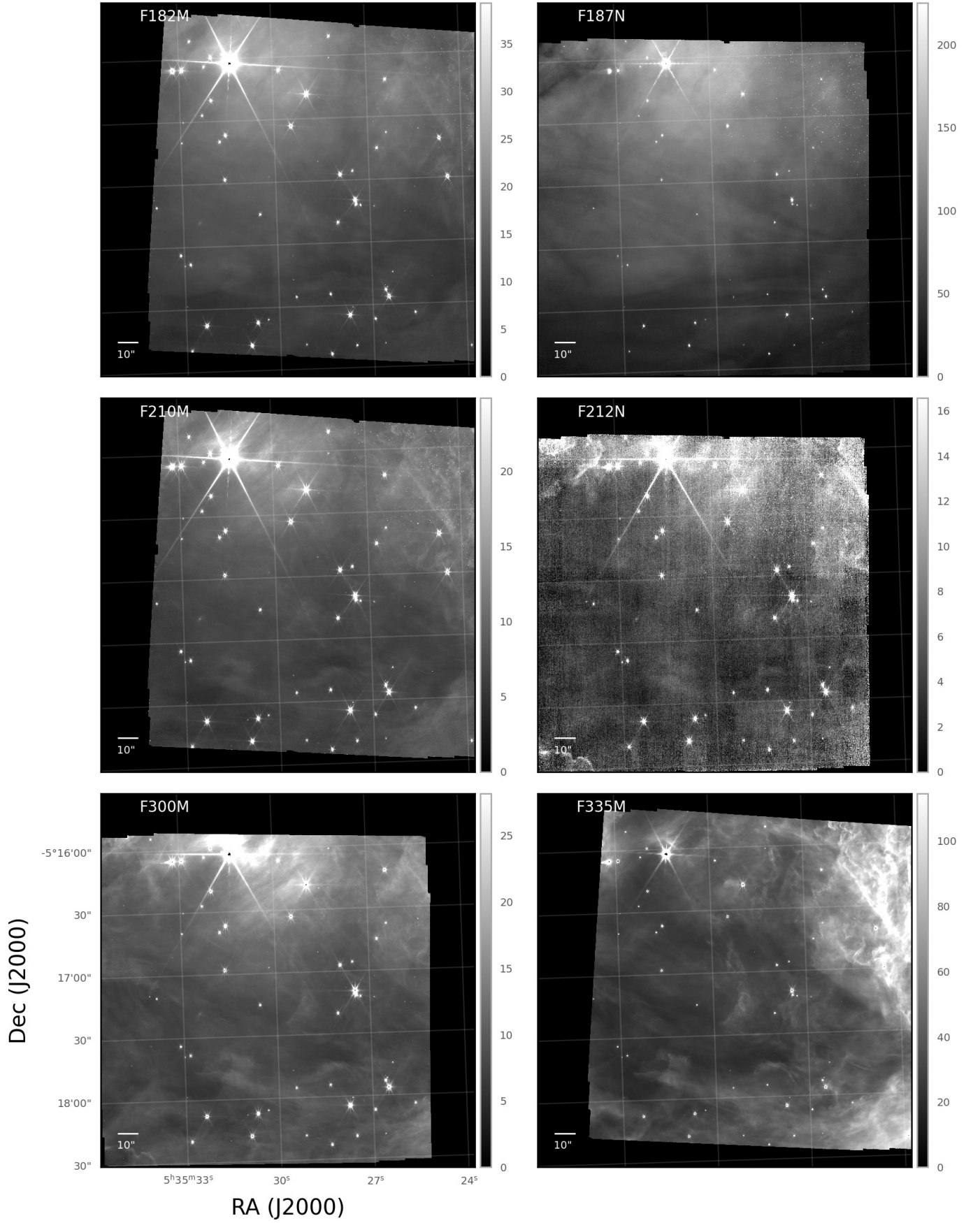**Fig. C.7.** Same as in Fig. C.5, but for other filters.
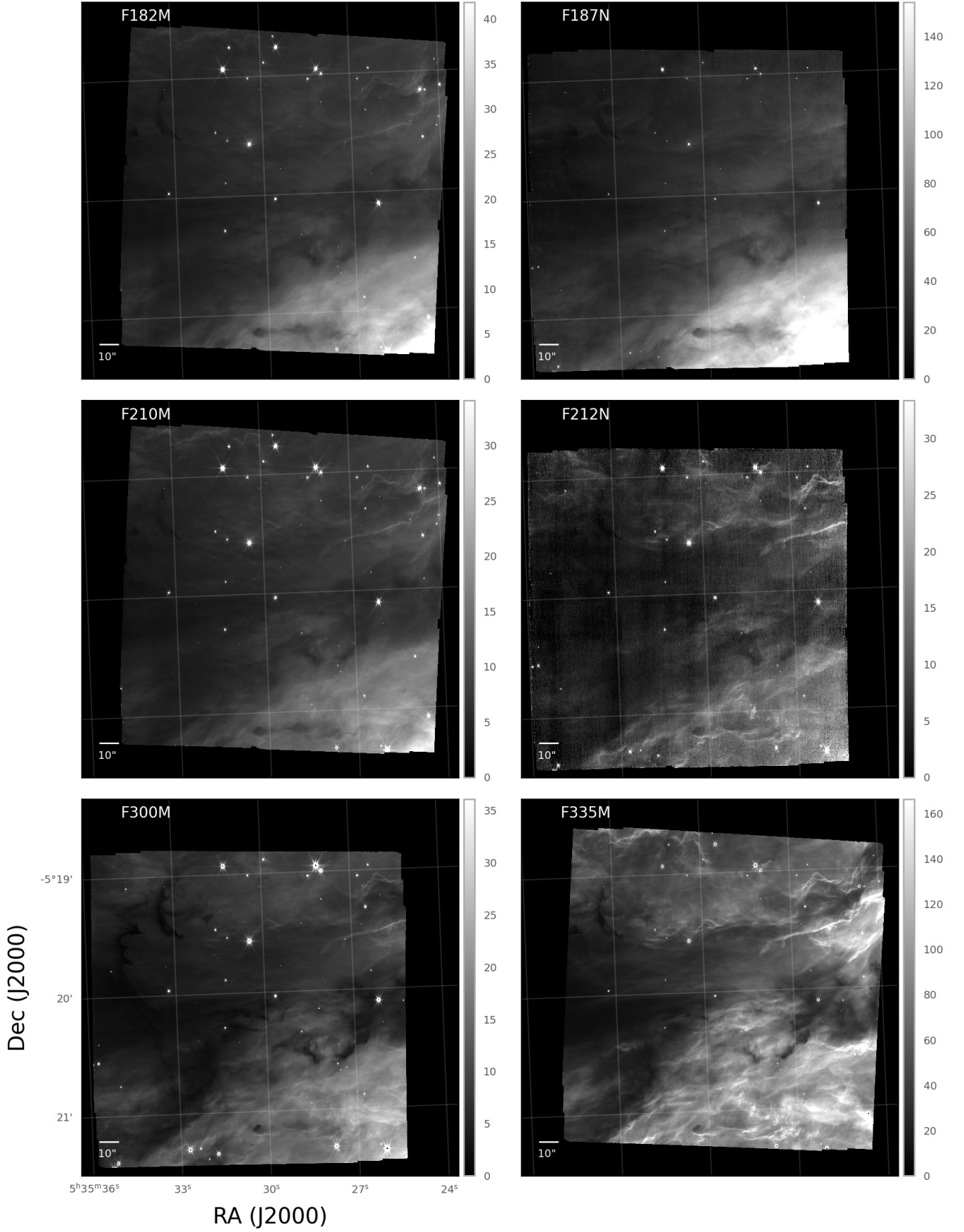
Fig. C.8. NIRCam maps of the M43 South region in different filters. Units are in MJy/sr.
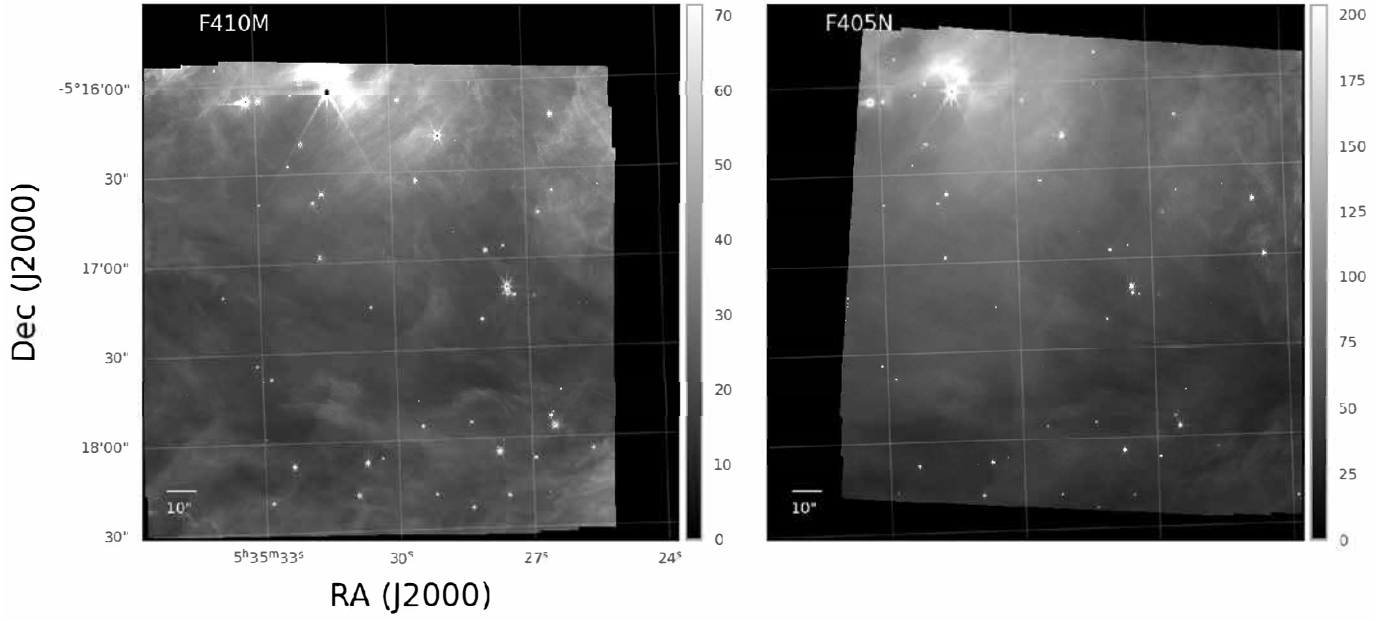
Fig. C.9. Same as in Fig. C.8, but for other filters.
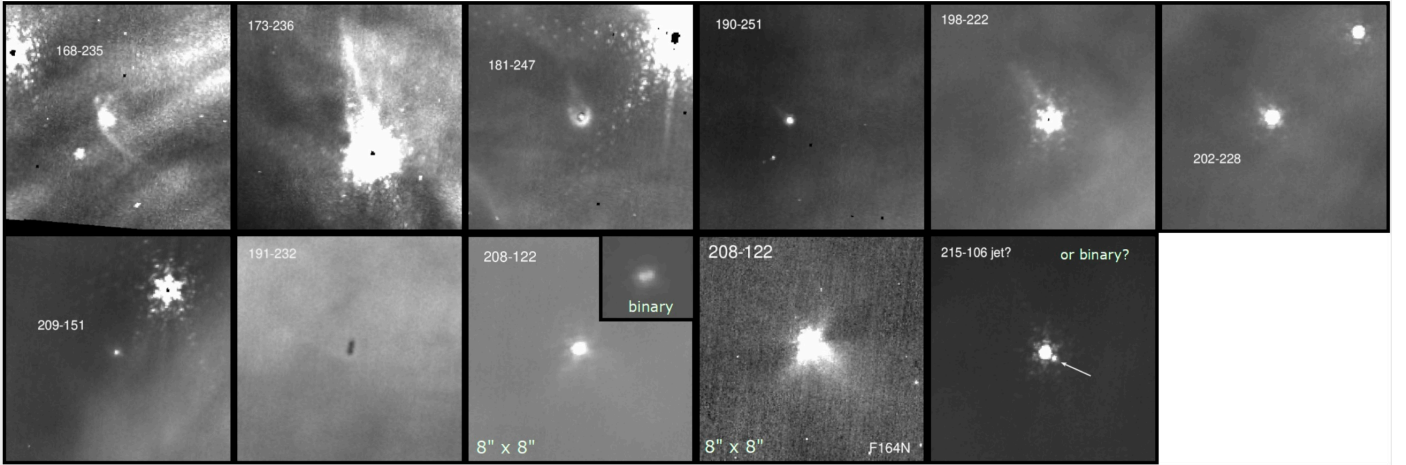
**Fig. C.10.** NIRCam maps of the M43 center region in different filters. Units are in MJy/sr.

Fig. C.11. Same as in Fig. C.10, but for other filters.

Fig. C.12. Zoom on the proplyds with extended structure identified in the F187N NIRCam image of the M42 north-east region (module A). The tiles are 5″ × 5″, with exception of the object 208-122 for which tiles are 8″ × 8″, with north is up and east to the left. Some images suffer from instrumental effects such as the diffraction pattern from bright stars and uncorrected cosmic ray events, affecting particularly the edge of the images because of lack of redundancy.
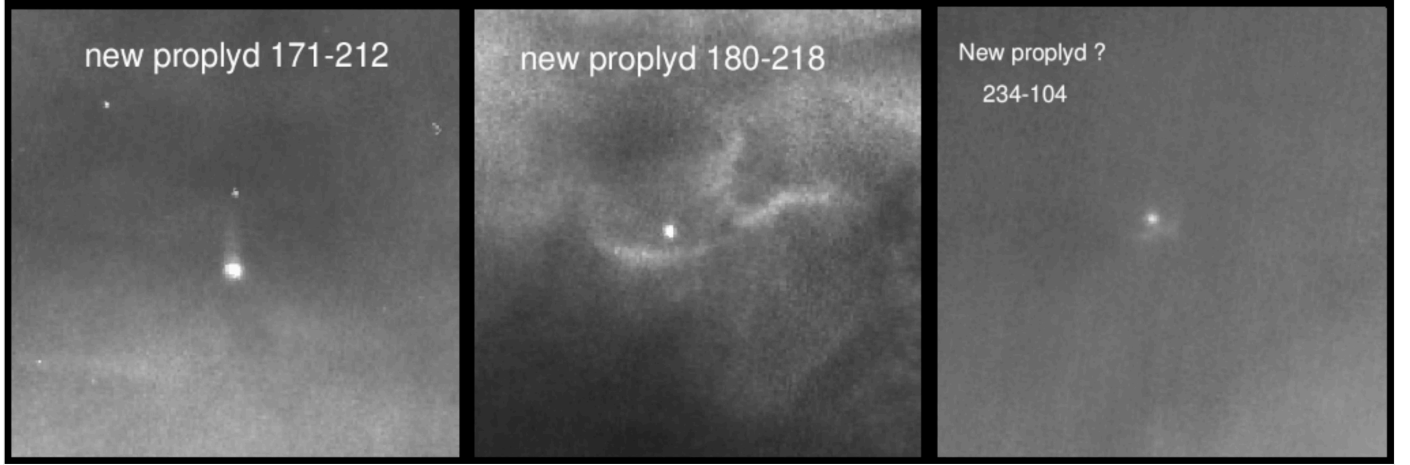
Fig. C.13. Zoom on the 3 new bright proplyds identified in the F187N NIRCam image north-east of the Trapezium stars (module A): 171-212, 180-218 and 234-104. They have faint cusps and only one shows a tail in Paα, that is proplyd 171-212. The tiles are 5″ × 5″ with north up and east to the left.
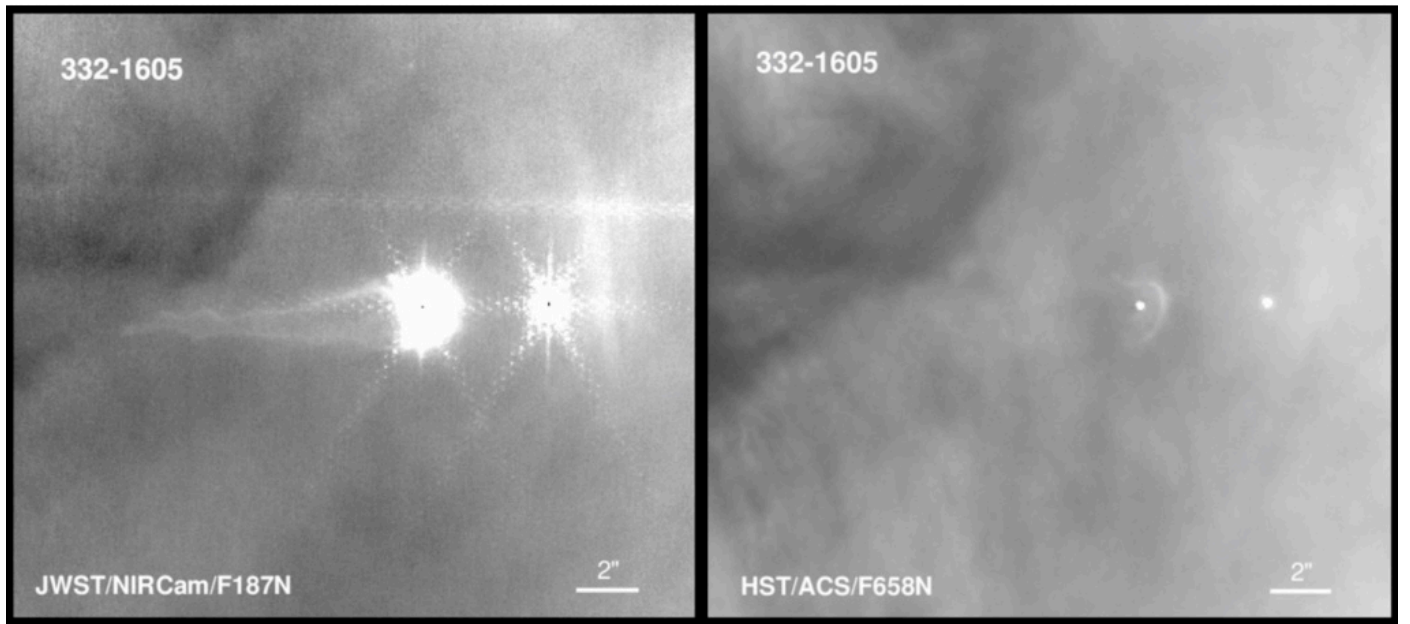
Fig. C.14. Zoom on the giant proplyd 332-1605 found in M43 (module A) and pointing directly to the ionizing star NU Ori, just 27″ to the west and not visible in the images. This object shows a long tail in Paα that is nearly 10 times larger than proplyd HST10. The Hα HST/ACS image of this object does not show any tail but only a faint cusp. The NIRCam F187N (left) and HST F1658N (right) images have similar spatial resolution allowing for a direct comparison of proplyd morphology in the optical and near-IR. North is up and east to the left.

Fig. C.15. Zoom on the new proplyd found in the M43 north region (detector A) at 97″ southwest of the ionizing star NU Ori (top figure). This object also shows a prominent jet identified by a chain of knots visible in both Paα and Hα images (bottom figure). However, the central star is only visible in the near-IR, reflecting the youth of this object. The JWST/NIRCam F187N images in the left and the HST/ACS F658N images in the right have similar spatial resolution. North is up and east to the left.